

DEVICE AND METASURFACE DESIGNS FOR NEXT-GENERATION BLUE-
EMITTING ORGANIC LEDs: COST, SUSTAINABILITY, EFFICIENCY, AND
STABILITY

By

CATRICE MONET CARTER

A dissertation submitted to the

School of Graduate Studies

Rutgers, The State University of New Jersey

In partial fulfillment of the requirements

For the degree of

Doctor of Philosophy

Graduate Program in Materials Science & Engineering

Written under the direction of

Deirdre M. O'Carroll

And approved by

New Brunswick, New Jersey

January 2018

ABSTRACT OF THE DISSERTATION

DEVICE AND METASURFACE DESIGNS FOR NEXT-GENERATION BLUE-EMITTING ORGANIC LEDs: COST, SUSTAINABILITY, EFFICIENCY, AND STABILITY

By CATRICE MONET CARTER

Dissertation Director:

Deirdre M. O'Carroll

Polymer-based organic light-emitting diodes (P-OLEDs), have potential to be a fully-solution-processable alternative to current display and lighting options. Currently, organic light-emitting diodes (OLEDs) can have internal quantum efficiencies of 100%. However, for white OLEDs the light-extraction efficiency is, at best, between 20-31%. The external quantum efficiency is lower for red and green (5.5% and 9%, respectively) phosphorescent OLEDs (Ph-OLEDs) and even lower for blue phosphorescent Ph-OLEDs (3.5%) as a result of poor light extraction. External quantum efficiency results are even lower for fluorescent P-OLEDs; therefore, further improvements must be made for white light and single color P-OLEDs. The use of alternative device architectures (such as top-emitting devices), integrated light management structures (such as using noble metal nanostructures), and improved charge transport layers, have shown to improve light-extraction from OLEDs. Device operational lifetime (i.e., stability) improvements are also needed; currently OLED luminaires on the market have lifetimes of approximately 10,000

hours to 100,000 hours, depending upon the operating luminance. Short OLED lifetimes are a result of unstable charge injection layers, non-radiative excited state interactions, and corrosion of the electrodes under ambient conditions. The implementation of encapsulants or getters and inverted device configurations can help to circumvent some of these stability issues.

In this thesis, various P-OLED device architectures are theoretically and experimentally studied to determine efficiency and stability enhancement approaches, with consideration for economic and environmental impacts. First, an economic, efficiency, and environmental assessment of four different P-OLED device configurations: bottom-emitting conventional, bottom-emitting inverted, top-emitting conventional and top-emitting inverted devices is carried out with regards to the following metrics: device cost, yearly operating cost, optical power cost and CO₂ emissions. For context, the metrics for the P-OLED devices are compared to those for a ubiquitous blue inorganic LED device architecture. The results show that the top-emitting inverted device architecture performs competitively at the laboratory scale with commercial-scale inorganic LEDs for all metrics and significantly reduces the device cost, yearly operating cost, optical power cost and CO₂ emissions for the P-OLED devices, due to elimination of indium tin oxide and its comparatively high luminous efficacy and longer lifetime. A scenario analysis is also carried out which projects economic and environmental impacts for P-OLEDs fabricated at a large scale.

Next, an experimental investigation of the photoluminescence (PL) stability, PL lifetime, and PL quantum yield of conjugated polymer:organometallic (PVK:FIrpic), blue, phosphorescent thin-films blends on silver metasurfaces is carried out in comparison to

corresponding data for the phosphorescent thin-film blend on planar silver films. Certain silver metasurfaces are found to have the ability to increase the radiative decay rate of triplet emission from the blue organic phosphorescent thin-films and this results in an improvement in the stability of the emission. In particular, this work shows that nanoparticle (NPT) Ag metasurfaces cause the greatest improvements in stability and brightness from the PVK:FIrpic thin films, with an average PL stability enhancement factor of 2, a reduction in the average PL lifetime by a factor of 1.29, and a PL intensity enhancement factor of 6.6 relative to PVK:FIrpic on planar Ag. Overall, the results have shown a correlation between enhanced PL stability and shorter PL lifetimes of PVK:FIrpic on silver plasmonic metasurfaces relative to a planar silver surfaces.

Finally, theoretical electromagnetic simulations are used to assess the light-extraction efficiency four different P-OLED configurations: conventional bottom- and top-emitting P-OLEDs and inverted bottom- and top-emitting P-OLEDs. The electromagnetic simulation results show that the total light extraction efficiency is the highest (28 %) for the bottom-emitting device configurations and the top-emitting conventional device has the lowest light extraction efficiency of 1 %. Further, it is shown that in-plane oriented dipoles contribute the most to the light extraction efficiency. The power absorbed in each device layer is also quantified and shows that a large portion of the power loss occurs when the dipole is oriented in the out-of-plane direction, particularly for the metallic layers, due to surface plasmon polariton modes at the metal/semiconductor interface.

In summary, this thesis identifies device designs and metasurface electrode types that can lead to efficiency and stability gains in polymer-based OLED devices using experimental and theoretical methods. The work is original in that it consists of the first

quantitative assessment of economic, energy and sustainability impacts of different OLED device architectures. Additionally, the demonstration that the local electromagnetic fields of metasurfaces can be used to improve the stability of phosphorescent OLED materials is unique and is relevant to the implementation of blue phosphorescence emitters in commercial OLEDs. The approaches to improve OLED device performance reported in this thesis have the potential to save on capital costs and on energy consumption, and to minimize the carbon footprint associated with OLED devices.

Acknowledgements

I would like to thank my mother and father, Tinette Carter and Reginald Colley, as well as my grandmother Diane McKinney. The matriarchs of my family have made sacrifices throughout my lifetime in order to ensure I was able to pursue my goals. Their support throughout my PhD studies has been invaluable and I am forever indebted. My life partner Jonathan Kees for his love and dedication to our family, which has enabled me to continue my pursuit of higher education after the birth of our daughter. My daughter, Jalyn Kees, and bonus sons, Sire Kees and Sincere Kees, thank you for giving me purpose to continue pushing through the hard times. This work is evidence that goals are accomplished through persistent effort and determination. My lifelong friend, Hanan Agyapong, for emphasizing self-care and mental health, as the mind, body, and soul are all connected. Lastly, the entire Hyter and Carter family for instilling in me the importance of education.

I would like to acknowledge my research collaborators: Zeqing Shen, Kun Zhu, Kelsey Gwynne, Justin Cho, Aaron Glanzer, and Nikola Kamcev, as well as my research group members Jill Tracey, Zhongkai Cheng, Cindy Kumah, and Hemanth Maddali for their assistance and feedback on research projects and the extended conversations during free time. My special friend Riyanka Pai, whose partnership throughout courses and fervent research conversations have added to my scientific body of knowledge.

Additionally, I would like to acknowledge Prof. Manish Chhowalla, Prof. Rick Garfunkel, and Dr. Johanna Bernstein for securing not only my funding as a NSF IGERT “Nanotechnology for Clean Energy” fellow, but also enabling me to travel to Addis Ababa, Ethiopia for the 2013 Africa MRS Conference.

I also would like to acknowledge my thesis committee members Prof. Laura Fabri, Prof. Dunbar Birnie, and Dr. Serpil Guran, for their time and willingness to serve on my committee. I would additionally, like to thank Dr. Guran for allowing me to study under during my internship with the Jerome Goldstein Scholarship for Ecoentrepreneurs.

I am forever indebted to my thesis advisor and professional mentor, Prof. Deirdre M. O’Carroll for her incessant support through my time at Rutgers. Having the privilege to study under such an immaculate researcher has enabled me to garner experimental, computational, scientific presentations, journal writing, time management and organizational skills. Her patience and diligence for sound and reputable research has pushed me to become a better scientist and a better individual.

Chapter 2 of this dissertation is based upon a first author publication lead by the author, C. Carter (Publication 3 from the List of Publications Section). Chapter 3 is based upon a first author publication in preparation by C. Carter *et al.* with contributions from fellow graduate students Zeqing Shen and Kun Zhu (Publication 1 from the List of Publications Section) and Chapter 4 is based upon unpublished computational results by the author.

Table of Contents

Abstract of The Dissertation.....	ii
Acknowledgments.....	vi
List of Figure Captions.....	x
List of Table Captions.....	xvi
List of Acronyms.....	xxi
List of Presentations.....	xxii
List of Publications.....	xxv
Chapter 1. Introduction.....	1
Electroluminescent Organic Semiconductor Devices	1
Electronic and Photonic Properties of Organic Semiconductors	2
Organic Semiconducting Materials.....	6
Organic Light-Emitting Diodes	7
Stability of Organic Light-Emitting Diodes	8
Efficiency of Organic Light-Emitting Diodes	9
Cost of Organic Light-Emitting Diodes.....	10
Thesis Overview	11
Chapter 2. Cost, Energy, and Emissions Assessment of Organic Light-Emitting Device Architectures	13
Abstract	13
Introduction	14
Methodology	19
Goal and Scope	19
Central Assumptions	22
Definition of Metrics	26
Results and Discussion.....	29
Life-Cycle Inventory - Device Architectures and Materials	29
Cost Assessment	31
Device Cost.....	31
Use-Phase Cost	33
Economic Impact	36
Energy and CO ₂ Emissions Assessment	37
Device Embodied Energy	37
GHG-Carbon Footprint.....	39
Interpretation, Scenario Analysis and Conclusions.....	42
Interpretation	42

Scenario Analysis	42
Conclusions	48
Chapter 3. Photoluminescence Stability of Blue Organic Phosphorescent Materials on Silver Metasurfaces	50
Abstract	50
Introduction	52
Methods	54
Sample Set Preparation	54
Preparation of Phosphorescent Organic Thin-Films.....	55
Metasurface Preparation	56
Characterization Methods	59
Results and Discussion.....	61
Conclusions	73
Chapter 4. Theoretical Predictions of Light-Extraction Efficiency of Planar OLED Device Architectures	75
Abstract	75
Introduction	77
Methods	81
Results and Discussion.....	87
LEE Results for Different Device Architectures	87
Effect of Dipole Orientation on LEE Results for Different Device Architectures.	89
Power Absorption Per Layer for Different Device Architectures	90
Conclusions and Future Directions	92
Chapter 5. Thesis Summary, Conclusions, and Future Directions	95
Thesis Summary and Conclusions	95
Future Directions.....	101
Economic, Efficiency, and Environmental Assessment (Extension).....	101
Characterization of the Operational Device Lifetime.....	101
Optimization of Active Layer Thickness Theoretical Calculation of External Quantum Efficiency with and without Plasmonic Nanostructures.	103
Conclusions.....	104
Appendix A	105
Appendix B	106
Appendix C	112
References	116

List of Figures

Figure 1.1: (left) Schematic of a basic organic semiconductor light-emitting diode device with anode, cathode, and organic semiconductor material. When a forward bias is applied electrons and holes recombine in the semiconductor layer and emit a photon. (right) Corresponding energy level diagram, charge carrier injection barriers are represented by the energy level difference between the HOMO and anode (holes), and LUMO and cathode (electrons).

Figure 1.2: Schematic of electronic energy levels of an organic semiconductor molecule showing the process of fluorescence and phosphorescence following electrical excitations. $\eta_{int,fl}$ and $\eta_{int,ph}$ indicate the theoretical internal quantum efficiency for fluorescence and phosphorescence under electrical excitation [9].

Figure 1.3: Molecular structures of selected organic semiconductor materials including conjugated and non- conjugated polymers and small molecules [15].

Figure 1.4: Copolymerization structure of functional units of an organic semiconducting material [15].

Figure 2.1: Schematic of life cycle assessment, from the inception of raw materials, to manufacturing of the device, device use, and recycling or reuse of the device. The structure

of blue P-OLEDs, bottom-emitting conventional and top-emitting inverted, are shown in the center.

Figure 2.2: System boundary diagram for a LCA of OLEDs. In this study, the assessment considers only the stages of the life cycle highlighted in by the dashed red boxes: raw materials extraction and production, OLED device fabrication, and OLED device use.

Figure 2.3: Schematics of: (a) a bottom-emitting conventional P-OLED, (b) a bottom-emitting inverted P-OLED, (c) a top-emitting conventional P-OLED, (d) a top-emitting inverted P-OLED, and (e) a blue inorganic LED. The blue arrows with $h\nu$ (photon energy) labels represent the direction of light emission.

Figure 2.4.: The percentage cost for each layer in the: (a) bottom-emitting conventional P-OLED; (b) bottom-emitting inverted P-OLED; (c) top-emitting conventional P-OLED; and (d) top-emitting inverted P-OLED. The materials cost, C_{mat} , for each device (1 m^2) is shown above the corresponding pie chart (i.e., manufacturing costs, C_{mat} , not included).

Figure 2.5: The corresponding C_{use} and C_{op} values for each P-OLED device architecture and a blue inorganic LED.

Figure 2.6: The corresponding GHG-CO₂ emissions for raw material extraction and device (1 m^2) manufacturing ($GHG-CO_{2,dev}$) and yearly GHG-CO₂ emissions from operation ($GHG-CO_{2,op}$) for each P-OLED device architecture and the blue inorganic LED.

Figure 2.7: Histograms showing the probability distribution of (a) C_{op} , (b) E_{use} and (c) $GHG-CO_{2,op}$ for top-emitting inverted P-OLEDs (1 m^2) generated using the Monte-Carlo method [45] for three different scenarios: small-scale, which assumes luminous efficacy (B_f) and operational lifetime (L) values of 7.9 lm/W and $28,000 \text{ h}$ (as reported in Table 2.3); large-scale (worst case), which assumes a factor of 6 reduction in B_f compared to the small-scale scenario and a $2,920 \text{ h}$ operational lifetime (i.e., 1 year); and large-scale (best case), which assumes a future “best case” large-scale production scenario that results in P-OLEDs with B_f and L values of 7.9 lm/W and $50,000 \text{ h}$, respectively. Normal distributions for B_f and L were generated as inputs for the Monte-Carlo analysis, assuming a relative standard deviation of 25% in B_f and L to represent typical performance parameter variations for polymer optoelectronic technologies. The Monte-Carlo analysis was carried out using Microsoft Excel with 10,000 random sampling iterations of the input distributions employed to calculate the probability distribution for C_{op} , E_{use} and $GHG-CO_{2,op}$.

Figure 3.1: Schematic of the sample configuration used for the PL stability measurements.

Figure 3.2: Schematic of the experimental configuration used for the transient PL lifetime measurements

Figure 3.3: (a) The chemical structures of the poly(N-vinylcarbazole) (PVK) and bis[2-(4,6-difluorophenyl)pyridinato- C^2,N](picolinato)iridium(III) (FIrpic) molecules. (b-e)

Schematic cross sectional diagrams of PVK:Firpic host:dopant thin-films on five different (meta)surface types: (b) planar silver, (c) nanoimprinted 1D silver gratings (both 1.6 μm grating pitch and 0.7 μm grating pitch); (d) nanoporous (NPO) silver, and (e) nanoparticle (NPT) silver.

Figure 3.4: The absorption and intensity normalized photoluminescence spectra of thin film host PVK, the dopant Firpic, and the blend PVK:Firpic.

Figure 3.5: SEM images of Ag metasurfaces: (a) the 1.6- μm -pitch 1D Ag grating, (b) the 0.7- μm -pitch 1D Ag grating, (c) Ag nanoparticles (NPT), and (d) nanoporous Ag (NPO). Insets in (a-d) are reflected-light, DF optical images. (e) DF spectra of the Ag metasurfaces. (f, g) Transmission spectra of (f) bare Ag metasurfaces and (g) PVK:Firpic-coated Ag metasurfaces.

Figure 3.6: PL stability (a,b) curves of PVK:Firpic thin films on various substrates. For the PL stability measurements, all samples were continuously exposed to a 355-nm laser. For the stability testing (a,b), 1.6 μm 1-D Ag grating, 0.7 μm 1-D Ag grating were all on a PMMA/glass substrate with silver thin films. The planar silver, 1.6 μm grating, and 0.7 μm grating all had 50 nm thick silver films, while the NPO and NPT were fabricated by dewetting from 50 nm thick silver films. All samples were spin coated with 20 g/L of PVK:Firpic yielding a film thickness of ~ 100 nm. The values in the parenthesis represent the luminance at the power meter (calculated using Equation 3.2) for each sample measurement; thus, the luminance at the sample is one order of magnitude larger.

Figure 3.7: PL lifetime (a) curves of PVK:Firpic thin films on various substrates and (b) the zoomed in time $t=0$ intensity peak. A 372-nm laser was employed for the PL lifetime measurements. The 1.6 μm 1-D Ag grating, 0.7 μm 1-D Ag grating were all on a PMMA/glass substrate with silver thin films. The planar silver, 1.6 μm grating, and 0.7 μm grating all had 50 nm thick silver films, while the NPO and NPT were fabricated by dewetting from 50 nm thick silver films. All samples were spin coated with 20 g/L of PVK:Firpic yielding a film thickness of ~ 100 nm

Figure 4.1: Schematic of the optical loss channels within a OLED device [187].

Figure 4.2: A dipole (blue arrow) suspended in free space oriented in either the (a) x , (b) y , and (c) z axes directions, respectively. The gray concentric circles correspond to the direction of propagation of the electric field away from the center of the dipole. The average emitted electromagnetic field is calculated by the magnitude of the electric field in the E_x , E_y , and E_z directions [187].

Figure 4.3: (a) Top-emitting inverted P-OLED cross-sectional image with dipole emitter located within the active layer and three power monitors for the light emitted out of the device (i), the electric field in the x -direction (ii.), and the electric field in the \hat{z} direction (iii.). (b) The dipole transmission monitor ($5 \text{ nm} \times 5 \text{ nm} \times 1 \text{ nm}$) encases only the dipole source within the active layer.

Figure 4.4: The electric field intensity profiles for electric dipoles within a PFO layer, polarized in the (a) x-direction and (b) z-direction.

Figure 4.5: (a) Bottom-emitting conventional P-OLED cross-sectional image with dipole emitter located within the active layer. (b) Bottom-emitting conventional P-OLED with three power monitors oriented around each device layer and the entire device structure, light extraction monitors oriented above device structure, and dipole transmission monitor in the x-z plane.

Figure A1: (Top) PL stability of Sample Set 1 (see Chapter 3, Methods). (Bottom) PL lifetime of Sample Set 1. All samples were continuously exposed to the 355-nm laser and 372-nm laser for the photoluminescence stability and lifetime testing, a. and b. respectively. For the stability testing PVK, Firpic, and PVK:Firpic were on a glass substrate, while 1D Ag Grating (1.6 μm), 1D Ag Grating (0.7 μm), NPO, and NPT were all on a PMMA/glass substrate with 50nm silver thin films. All samples were spin coated with 20 g/ μL of PVK:Firpic.

Figure B1: Schematic of a bottom-emitting P-OLED with nanostructures embedded within the active layer, and, in between the anode and HTL, and cathode and ETL layers.

Figure C1: The steps for P-OLED fabrication include etching of the ITO (a), the spin coating of the polymer layers (b), and the thermal evaporation of the metallic layers (c).

Figure C2: 4-point probe measurements of PEDOT:PSS with current being injected

through probes 1 and 4 and voltage being measured between probes 2 and 3.

List of Tables

Table 2.1: Table of bottom-emitting (conventional and inverted) and top-emitting (conventional and inverted) P-OLED device layer materials, layer thicknesses and corresponding layer functions. The thickness values are an average of values reported in the corresponding referenced literature with the standard deviation shown after the average value. Glass substrates with thickness of 0.192 mm were assumed for all P-OLED device architectures.

Table 2.2: The mass of each layer for a 1 m² device, the material dollar per gram (\$/g) values and the cost of each layer (\$/m²) in a particular device are represented for bottom-emitting conventional P-OLED, bottom-emitting inverted P-OLED, top-emitting conventional P-OLED, top-emitting inverted P-OLED, and blue inorganic LED architectures [105-114]. Only the materials that are used in a particular device architecture are represented in the respective column. The cost per layer for the encapsulant is a generic value take from Ref. [49]. Each material layer function is represented by the following superscript characters: ^substrate, #anode, ×HTL, +active layer, ~ETL, *cathode.

Table 2.3: The operational lifetime, L , and luminous efficacy, B_f , are represented for the bottom-emitting conventional P-OLED, bottom-emitting inverted P-OLED, top-emitting conventional P-OLED, top-emitting inverted P-OLED and blue inorganic LED.

Table 2.4: The metrics C_{dev} , C_{op} and C_{lm} for each P-OLED device architecture and the blue inorganic LED (device areas are 1 m² in all cases).

Table 2.5: Embodied energy in MJ/kg of materials in P-OLED devices.

*Data for P3HT used here as an approximation for PFO (PFO embodied energies not available), #LiCl used here instead of LiF as embodied energy data was limited for LiF; ‡value is in units of MJ/m²

Table 2.6: Embodied energy (in MJ) from raw material extraction per layer of material in 1 m² P-OLED devices (direct layer process energy not included).

Table 3.1: The stability enhancements (i.e., enhancements in the half-life (L_{50})) of PVK:FIrpic thin films on various substrate types. Data is reported for measurements carried out on different sets of samples (i.e., “Sets”) and on different days (“Trials”) to check the repeatability of the data, as follows: Sample Set 1 Trial 1 (S1T1), Sample Set 2 Trial 1 (S2T1) and Sample Set 2 Trial 3 (S2T3). The various substrate types are glass, planar Ag, 1.6 μm 1-D Ag grating and 0.7 μm 1-D Ag grating patterned metasurfaces, and NPT and NPO nanostructured metasurfaces. Two different luminances were employed for the stability measurements: 10,000 cd/m² (indicated by (*)) and 1,000 cd/m² (indicated by (+)) which were determined from the measured excitation power densities. All metallic substrate types (except “Glass”) had an underlying glass coverslip as the substrate.

Table 3.2: The average PL lifetime (τ_{average}), intensity at time, $t = 0$, shortest PL lifetime decay component (τ_1), longer PL lifetime decay component (τ_2), and the longest PL lifetime decay component (τ_3) for PVK:FIrpic thin films on glass, planar Ag, 1.6 μm 1-D

Ag grating and 0.7 μm 1-D Ag grating patterned, NPT and NPO nanostructured Ag metasurfaces. The PL lifetime components were extracted from fits to the data using a second or third order exponential decay function. Planar Ag and 1D Ag gratings had an underlying glass coverslip or PMMA/glass coverslip as the substrate.

Table 3.3: The stability enhancement (i.e., enhancement in the half-life (L_{50})), average PL lifetime (τ_{avg}), and PL intensity enhancement (E_{PL}) of PVK:FIrpic on various substrate types. Data is reported for measurements carried out on different sets of samples (i.e., “Sets”) and on different days (“Trials”) to check the repeatability of the data, as follows: Sample Set 1 Trial 1 (S1T1), Sample Set 2 Trial 1 (S2T1) and Sample Set 2 Trial 3 (S2T3). The various substrate types are glass, planar Ag, 1.6 μm 1-D Ag grating and 0.7 μm 1-D Ag grating patterned metasurfaces, and NPT and NPO nanostructured metasurfaces. Two different luminances were employed for the stability measurements: 10,000 cd/m^2 (indicated by (*)) and 1,000 cd/m^2 (indicated by (+)) which were determined from the measured excitation power densities. The PL quantum yield (QY) for Sample Set 1 for PVK:FIrpic thin films on glass, planar Ag, 1.6 μm 1-D Ag grating and 0.7 μm 1-D Ag grating patterned, NPT and NPO nanostructured Ag metasurfaces. Measurements carried out in collaboration with Kun Zhu. Planar Ag and 1D Ag gratings had an underlying glass coverslip or PMMA/glass coverslip as the substrate.

Table 4.1: The theoretical FDTD simulation LEE results using real and complex refractive indices for four device configurations: bottom-emitting conventional and inverted and top-

emitting conventional and inverted relative to literature theoretical FDTD simulation LEE for bottom-emitting and top-emitting conventional device configurations.

Table 4.2: The theoretical FDTD simulation LEE extraction efficiency for dipole orientation results for four device configurations: bottom-emitting conventional and inverted and top-emitting conventional and inverted relative to literature theoretical FDTD simulation LEE for bottom-emitting and top-emitting conventional device configurations.

Table 4.3: The theoretical FDTD simulation power absorption per layer results for dipole oriented in the x and z direction of four device configurations: bottom-emitting conventional and inverted and top-emitting conventional and inverted.

List of Abbreviations

Abbreviation	Unit	Definition	Description
m_w	g/mol	Molecular weight	The mass of a molecule which includes the sum of each atomic element multiplied by the number of atoms of that element in the molecular formula
OLED	-	Organic light -emitting diode	A light-emitting diode in which the emissive layer is an organic compound
PPV	-	Poly(<i>p</i> -phenylene vinylene)	A conducting polymer which can be doped to exhibit electrical properties
PVK	-	Poly(9-vinylcarbazole)	A transparent polymer with excellent insulating properties
PFO	-	Poly(9,9-dioctylfluorene)	A conjugated semiconducting polymer
P-OLED	-	Polymer- based organic light-emitting diode	A light-emitting diode in which the emissive layer is an emitting polymer
Ph-OLED	-	Phosphorescent organic light-emitting diode	A light-emitting diode in which the emissive layer is a phosphorescent emitter
HOMO	-	Highest Occupied Molecular Orbital	Molecular orbitals which represent the occupied energy levels in semiconductors analogous to the valence band in conductors
LUMO	-	Lowest Unoccupied Molecular Orbital	Molecular orbitals which represent the unoccupied energy levels in semiconductors analogous to the conduction band in conductors
S_0	-	Ground singlet state	The molecular state occupied by electrons prior to electrical excitation

S_1	-	Excited singlet state	A molecular state in which the spin of the excited state is paired with the spin the ground state
T_1	-	Excited triplet state	A molecular state in which the spin of the excited state is unpaired with the spin the ground state
NPB	-	<i>N, N</i> diphenyl- <i>N, N</i> -bis-1-naphthyl-1,1-biphenyl-4-4-diamine	A hole transport material used in organic light-emitting diodes
TBADN	-	2-(<i>t</i> -butyl)9,10-bis(2-naphthyl)anthracene	A hole transport material used in organic light-emitting diodes
PEDOT:PSS	-	poly(3,4-ethylenedioxythiophene) polystyrene sulfonate	A hole transport material used in organic light-emitting diodes
Ca	-	Calcium	A chemical element
LiF	-	Lithium Fluoride	An inorganic optical material
PL	-	Photoluminescence	The emission of light due to photoexcitation
Lm	-	Lumen	SI unit of luminous power
Cd	-	Candela	SI unit of luminous intensity brightness
W	-	Watt	SI unit of power
H	-	Hour	Time
kW h	-	Kilowatt hour	Unit of energy
C_{dev}	\$	Device cost	The total cost of materials and cost to manufacture a device architecture
C_{op}	\$/yr	Yearly operating cost	Cost to operate the device for 8 hours per day over a one year period
C_{lm}	\$/h	Optical power cost	Cost to continuously generate 1000 cd/m ² for one hour
$GHG-CO_{2,dev}$	kg CO ₂	CO ₂ emissions from device production	CO ₂ greenhouse gas emissions from raw materials extraction and manufacturing of a 1 m ² device
E_{mat}	MJ/kg	Material embodied energy	Embodied energy of the raw materials in a device

E_{man}	MJ/kg	Direct process energy	Energy consumed during device manufacturing
I_{CO_2}	kg CO ₂ /kWh	Carbon emission intensity	Average CO ₂ emission intensity
$GHG-CO_{2,op}$	kg CO ₂ /yr	Yearly operating CO ₂ emissions	Yearly CO ₂ greenhouse gas emissions produced from a 1 m ² device operating for 8 hours per day
C_{mat}	\$	Cost of materials in the device	Cost of raw materials used for a 1 m ² device
C_{man}	\$	Manufacturing cost	Cost to manufacture a 1 m ² device
C_{use}	\$	Use phase cost	The cost to electrically power each device architecture
L	Hour	Operational lifetime	The length of time it takes for device luminous efficacy to degrade by 50%
C_{elec}	\$(/kW h)	Cost of electricity in the USA	-
E_{use}	kW h or GJ	Use-phase energy consumption	The electrical energy needed to operate a device over its entire use phase
P_{in}	W	Power in	Electrical power applied to the device
P_{out}	lm/m ²	Power out	Luminous flux (i.e., perceived optical power) per m ²
B_f	lm/W	Luminous efficacy	Electrical-to-optical power conversion efficiency
K	0.75	Correction factor	Accounts for device operation at 75% of its initial luminous efficacy, on average, due to degradation and efficiency “roll-off” during its operational lifetime
B	cd/m ²	Luminance	Used to quantify the brightness of a light-emitting device
EL	-	Electroluminescence	The emission of light due to an electrical current

SPP	-	Surface Plasmon Polariton	Electromagnetic oscillations along a metal/dielectric material interface
FIrpic	-	bis[2-(4,6-difluorophenyl)pyridinato-C2,N](picolinato) iridium(III)	Phosphorescent blue emitter
NPO	-	Nonporous	Metal surface with pores approximately 1 pores per μm^2 in size
NPT	-	Nanoparticles	Particles less than 100 nm in size
LCD	-	Liquid crystal display	A flat panel display which uses liquid crystals
TPA	-	triplet-polaron annihilation	Annihilation occurs when an excited polaron state pairs with a triplet exciton
TTA	-	triplet-triplet exciton annihilation	Annihilation occurs when triplet excitons in a high-energy excited state accumulate due to the long lifetime of the emitting triplet state
S1T1	-	Sample Set 1 Trial 1	The metasurfaces were spin coated with 19:1 host:dopant mixture in chlorobenzene
S2T1	-	Sample Set 2 Trial 1	The metasurfaces were spin coated with 9:1 host:dopant mixture in chlorobenzene
S2T2	-	Sample Set 2 Trial 2	The metasurfaces were spin coated with 9:1 host:dopant mixture in chlorobenzene
S2T3	-	Sample Set 2 Trial 3	The metasurfaces were spin coated with 9:1

				host:dopant mixture in chlorobenzene
LEE	%	Light extraction efficiency		The ratio of the emitted photons over the total produced photons
FDTD	-	Finite difference time domain		A numerical analysis used to computational model electrodynamics
LEE _{total}	%	Total light extraction efficiency		The sum of the light extraction efficiency in the x, y and z directions
P _{abs}	%	Total power absorption		The sum of the power absorbed per layer in the x, y, and z directions
P _{abs,x}	%	Power absorption in the x direction		The power absorbed when emission is perpendicular to the device
P _{abs,z}	%	Power absorption in the z direction		The power absorbed when emission is parallel to the device
TOLED	-	Top emitting organic light emitting diode		Organic light emitting diode in which light emission occurs through an optical thin metal electrode
BOLED	-	Bottom emitting organic light emitting diode		Organic light emitting diode in which light emission occurs through a thick transparent electrode
WGM	-	Waveguided mode		Confinement of electromagnetic waves between a linear structure's endpoint
P _{averaged}	%	Average power absorption		The averaged power absorbed in x, y, and z directions

List of Presentations

Oral Presentations

1. C. M. Carter, Z. Chen, K. Zhu, K. Gwynne, and D. M. O'Carroll, Photoluminescence Stability of Blue Organic Phosphorescent Materials on Silver Metasurface Electrodes. *Laboratory for Surface Modification – Institute for Advanced Materials Devices and Nanotechnology* Piscataway, New Jersey (2017).
2. C. M. Carter and D. M. O'Carroll, Theoretical Predictions for Light Extraction Efficiency of Organic Polymer Light Emitting Diodes. *Society of Women Engineers – Rutgers Graduate Chapter* Piscataway, New Jersey (2016).
3. C. M. Carter and D. M. O'Carroll, Light Extraction Efficiency Assessment of Organic Polymer Light-Emitting Device Architectures. *Materials Research Society Fall Meeting* Boston, Massachusetts (2015).
4. C. M. Carter, J. Cho, A. Glanzer, N. Karncey, and D. M. O'Carroll, Economic and Environmental Assessment of Organic Polymer Light Emitting Diodes. *Materials Research Society Fall Meeting* Boston, Massachusetts (2014).
5. C. M. Carter and D. M. O'Carroll, Economic and Environmental Assessment of Polymer Light Emitting Diodes. *Africa Materials Research Society* Addis Ababa, Ethiopia (2013).
6. C. M. Carter, T. Babakol, J. Brock, X. Fang, Y. Kim, Characterization of Oxygen Vacancies in SrTiO₃. *Louis Stokes Alliances for Minority Participation* Northfield, Minnesota (2011).
7. C. M. Carter, T. Babakol, J. Brock, X. Fang, Y. Kim, Characterization of Oxygen Vacancies in SrTiO₃. *Cornell Center for Materials Research* Ithaca, New York (2010).
8. S. Schlotter, C. M. Carter, T. Brenner, B. Colwell, A. Kinsey, B. Schuster, M. Eblen-Zayas, Magnetic and transport properties of EuO films fabricated by oxidation of Eu metal films. *American Physical Society* Portland, Oregon (2010).

Poster Presentations

1. C. V. Antonick, C. E. Petoukhoff, C. M. Carter, D. M. O'Carroll, Inverted Organic Polymer-Based Light Emitting Diodes with Native Silver Oxid Hole Transport Layers. *Materials Research Society Fall Meeting* Boston, Massachusetts (2015).
2. K. Gwynne, C. M. Carter, and D. M. O'Carroll, Photoluminescence Stability of Blue Organic Phosphorescent Materials on Silver Nanostructured Surfaces. *Research in Science and Engineering* Piscataway, New Jersey (2015).

3. S. Siva, C. M. Carter, C. E. Petoukhoff, D. M. O'Carroll, Fabrication and Lifetime Testing of Polymer Light-Emitting Diodes. *Materials Research Society Fall Meeting* Boston, Massachusetts (2014).
4. M. Jain, S. Siva, C. E. Petoukhoff, C. M. Carter, D. M. O'Carroll, Solution Deposition of Multi-Layer Transparent Conducting Cathodes on Conjugated Polymer Active Layers for Inverted Plasmonic Photovoltaics. *Materials Research Society Fall Meeting* Boston, Massachusetts (2014).
5. C. Kumah, C. M. Carter, and D. M. O'Carroll, Nanoporous Metal Electrodes and Insulator-Semiconductor-Metal-Insulator Waveguides. *Research in Science and Engineering* Piscataway, New Jersey (2014).

List of Publications

1. C. M. Carter, Z. Chen, K. Zhu, K. Gwynne, and D. M. O'Carroll, Photoluminescence Stability of Blue Organic Phosphorescent on Silver Plasmonic Electrodes. Manuscript in Preparation.
2. A. K. Dalsania, J. Kohl, C. Kumah, Z. Shen, C. E. Petoukhoff, C. M. Carter and D. M. O'Carroll, Effects of Metal Film Thickness and Gain on the Coupling of Organic Semiconductor Exciton Emission to Surface Plasmon Polaritons. *J. Mater Chem. C*, 00, 1-9 (2016).
3. C. M. Carter, J. Cho, A. Glanzer, N. Kamcev, and D. M. O'Carroll, Cost, Energy, and Emissions Assessment of Organic Polymer Light-Emitting Device Architectures. *J. Clean Prod.*, 137, 1418-1431 (2016).
4. D. M. O'Carroll, C. E. Petoukhoff, J. Kohl, B. Yu, C. M. Carter, S. Goodman, Conjugated Polymer-Based Photonic Nanostructures. *Poly. Chem.*, 4, 5181-5196, (2013) review paper.

Chapter 1.

Introduction

1.1. Electroluminescent Organic Semiconductor Devices

In the 1960s, Martin Pope reported electroluminescence (EL) from single crystal anthracene and a doped anthracene crystal under direct current [1]. However, the molecular crystals, held together due to Van-der-Waals forces, had micron-scale thicknesses, thus visible EL emission occurred with applied electric fields of only a few 100s of volts. Despite this early EL demonstration, practical applications were prevented due to the high operating voltages necessary for working devices and the instability of the charge injection contacts. The research which followed provided a theoretical basis of optical excitation and charge carrier transfer in organic materials [1-3].

In 1976, Alan MacDiarmid, Hideki Shirakawa, and Alan J. Heeger discovered that π -conjugated polymers, hydrocarbon chains with alternating single and double bonds, can have high conductivities when they are extrinsically doped with chlorine, bromine, or iodine vapour; thus, showing that polymers could be used as electrically active materials [4-4]. The discovery by Tang and Van Slyke *et al* in 1987 of EL from a novel thin film organic device structure was the technological advancement of organic semiconductors. They discovered EL from a thin-film of the conjugated organic molecule, Alq₃, (thickness of ~100 nm) with an external quantum efficiency of 1% (emitted photons to injected electrons) [6]. Thus, with the thin film thickness much smaller compared to molecular crystal thicknesses, a lower applied electric field was required to observe EL (below 10 V), minimizing the barrier to charge injection [6]. In parallel, research was completed into

semiconducting polymer devices, in part, due to their ease of processibility. In 1990, EL was observed from a 100-nm-thick film of a non-doped π -conjugated polymer poly (para-phenylenevinylene (PPV)) using an applied voltage below 14 V [7]. Following from these early demonstrations of EL from organic semiconductors, over the course of the next three decades great advances were made in the synthesis of new EL organic semiconductors, processing of organic semiconductors, and optimization of organic device architectures, which lead to the use of organic semiconductor-based light-emitting diodes for commercial display and lighting.

1.1. 1. Electronic and Photonic Properties of Organic Semiconductors

Organic semiconductors refer to organic materials, which primarily contain carbon and hydrogen atoms, whose building blocks are covalently-bonded molecules or polymers with both σ - and π -bonding that exhibit semiconducting properties. The semiconducting properties are primarily due to the conjugated chemical bonding, i.e., alternating single and double bonds, in the molecular backbone. Conjugation is formed by the overlap of the out of plane p_z orbitals due to the hybridization of the sp^2 carbon atoms in the molecules; thus, forming highly directional σ -bonding and σ^* -antibonding and delocalized π -bonding and π^* -antibonding. The backbone of the molecule is formed by σ bonds, thus making π bonding significantly weaker. Consequently, the least energetic electron excitations of conjugated molecules are the π - π^* transitions with an energy gap typically between 1.5 and 3 eV, such transitions leading to light absorption or emission in the visible radiation regime [8].

The number of chemical bonds that can form are determined by the number of hybrid orbitals and the remaining unoccupied p orbitals. Each chemical bond between carbon atoms represents a pair of electrons shared between the two atoms, which makes it equally probable that the electrons can be found orbiting either atom; thus, associating the electrons with a molecular orbital rather than atomic orbitals [7,8]. In highly unsaturated, conjugated organic molecules with π -bonded carbon atoms, this enables delocalization of the electron cloud in a molecular orbital that spans the entire molecule (or even over one or more molecular monomer units in the case of conjugated polymers).

Organic semiconductors tend to have poor charge-carrier mobility and relatively small photoexcitations diffusion lengths. In the solid state, organic semiconductor molecules interact by relatively weak van der Waals forces, dipole-dipole interactions, and/or hydrogen bonding. This results in relatively large intermolecular distances due to the many degrees of conformational freedom that each molecule can adopt with differing relative orientations. In conjugated molecules, the strong Coulomb interactions in a molecule either pull electrons towards or repel holes (vacancies) away from the positively charged nuclei; thus, distorting the molecule and creating a polaron, i.e., a charge with phonons. As a result, charges adopt a lower energy and more localized state than the highest occupied molecular orbital (HOMO) or lowest unoccupied molecular orbital (LUMO) level of the molecule; thus, resulting in charge transport at elevated temperatures due primarily to electron-transfer or hopping between localised states [9,10].

The highest occupied molecular orbitals (HOMO) and the lowest unoccupied orbitals (LUMO) in organic semiconductors are analogous to that of the valence and conduction bands within an inorganic semiconductor. The electronic energy gap is the

energy difference between the HOMO and LUMO levels (Figure 1.1). This electronic energy gap can be controlled by the degree of conjugation. When the semiconductor is optically driven, electrons are transported through the LUMO levels and an unpaired electron in HOMO leading to a positively charged vacancy are transported through the HOMO levels [9,14].

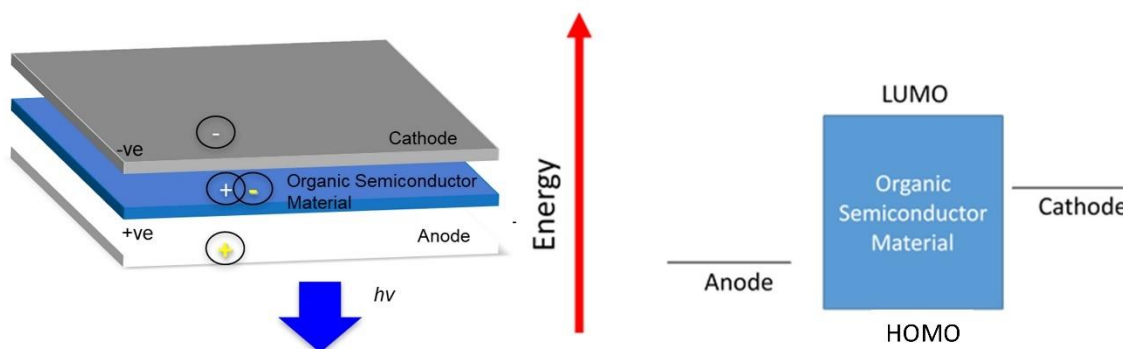


Figure 1.1: (left) Schematic of a basic organic semiconductor light-emitting diode device with anode, cathode, and organic semiconductor material. When a forward bias is applied electrons and holes recombine in the semiconductor layer and emit a photon. (right) Corresponding energy level diagram, charge carrier injection barriers are represented by the energy level difference between the HOMO and anode (holes), and LUMO and cathode (electrons).

In the ground state of many organic semiconductors, all bonding orbitals up to the HOMO level are half-filled with antiparallel spin electrons and the antibonding orbitals are empty from the LUMO level onward. When an electron is added to a π -bonding state or taken from a π^* -antibonding state the spatial distribution is altered for the σ orbitals; thus, resulting in more energy required to add or remove a second electron. This changes the molecular orbital position relative the vacuum level and shortens bond length [11].

Organic semiconductor materials have well-defined spin states (singlet and triplet) in a molecule. The ground electronic state is a singlet state (S_0) and the first-excited singlet state (S_1) is populated upon absorption of photons with energy greater than the band gap (difference in energy between S_0 and S_1) or vibrionic permeations. The excited triplet state (T_1) lies at an energy below (S_1) and cannot be directly optically excited. However, upon electrical excitation the T_1 state can be directly populated with electrons. Fluorescence, the rapid transition from S_1 to S_0 has a lifetime of $\sim 1-10$ ns, while phosphorescence, the transition from T_1 to S_0 , which can occur due to intersystem crossing, has a lifetime of ~ 10 μ s [8]. In fluorescent materials due to quantum mechanics phosphorescence is prohibited. Therefore, due to the relatively long lifetime of phosphorescence radiative decay, it is typically not observed at room temperature. Since the triplet states have a degeneracy of three, on average, 75% of excitons in organic semiconductors created by electrical excitation are triplet states; thus, influencing the theoretical EL quantum efficiency limit [9]. The efficiency of radiative processes is influenced by whether the organic semiconductor material is a fluorescent or phosphorescent emitter with the internal quantum efficiency being theoretically 25% and 100%, respectively (Figure 1.2).

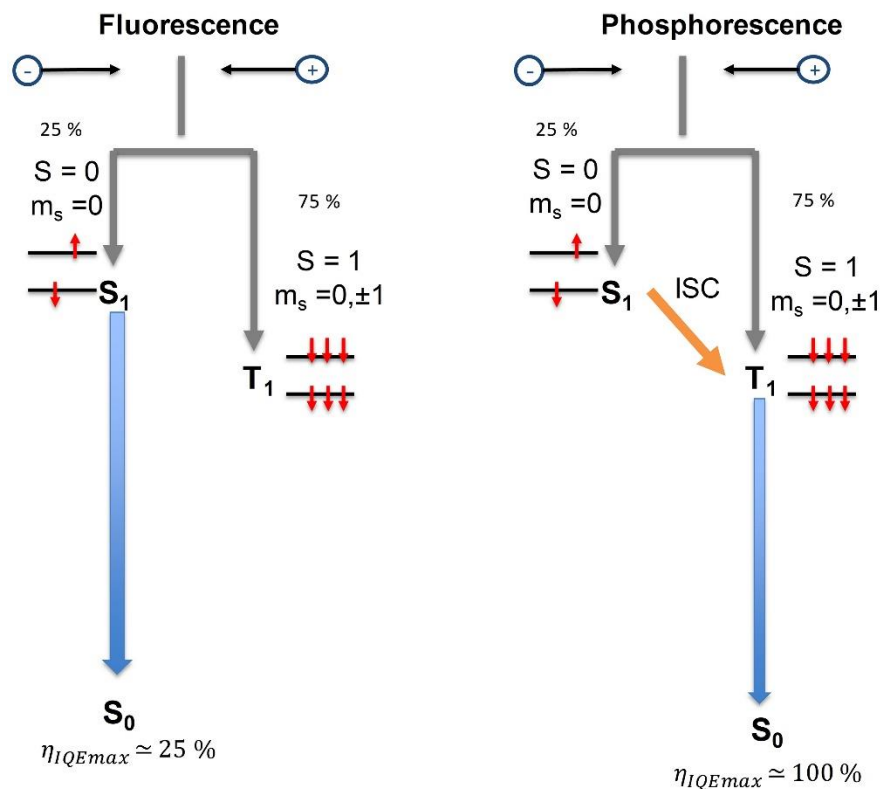


Figure 1.2: Schematic of electronic energy levels of an organic semiconductor molecule showing the process of fluorescence and phosphorescence following electrical excitations. $\eta_{int,fl}$ and $\eta_{int,ph}$ indicate the theoretical internal quantum efficiency for fluorescence and phosphorescence under electrical excitation [9].

1.1.2. Organic Semiconducting Materials

Organic semiconductor materials can be classified by molecular weight, m_w , into two major categories: low molecular weight, m_w , small molecule ($m_w < 1$ kg/mol) and those with larger m_w , polymers ($m_w > 1$ kg/mol). Polymers can be further classified into conjugated and non-conjugated polymers. Conjugated polymers follow the photophysics described in Section 2.1.1., while non-conjugated polymers host-guest blend types act as

an electrical deliver with functional guest fluorescent or phosphorescent emitters doped into the polymer host [15]. Some common small molecule materials are Alq₃ and pentacene, while some common conjugated and non-conjugated polymer materials are poly (*p*-phenylene vinylene) PPV and poly(9,9- dioctylfluorene) PFO and poly(9-vinylcarbazole) PVK derivatives respectively (Figure 1.3). The primary difference is the deposition methods where small molecule thin films are deposited from gas sublimation or evaporation, while polymers can be solution processed using spin-coating, ink-jet printing, or industrial reel- to-reel coating.

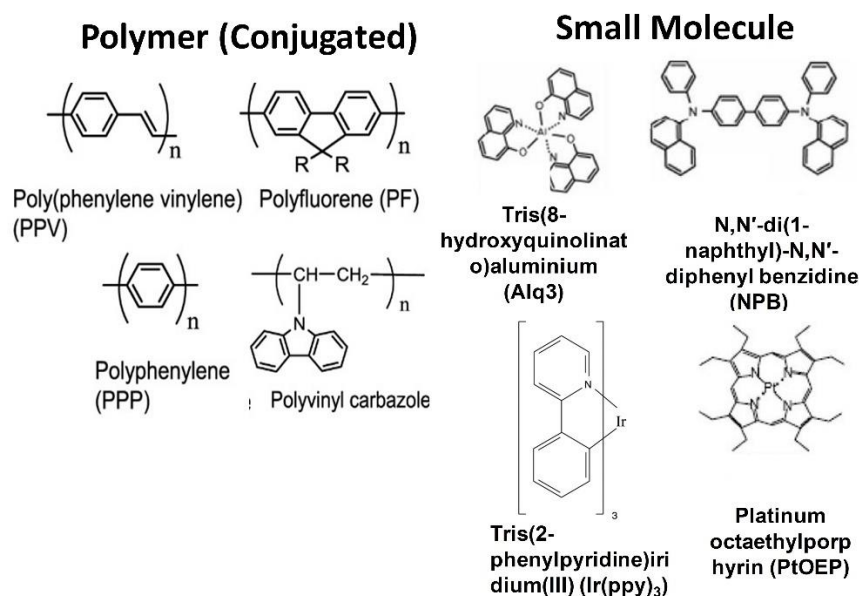


Figure 1.3: Molecular structures of selected organic semiconductor materials including conjugated polymers and small molecules [15].

Organic semiconductors are primarily p-type due to the instability of radical anions and photooxidation of pi-conjugated backbone.

1.2. Organic Light-Emitting Diodes

Organic semiconductor materials are of particular interest for organic light-emitting diodes (OLEDs). These organic semiconductor materials can be coupled together with a transparent conducting high work function anode and a metallic low work function cathode (Figure 2.4.) thus forming an OLED. OLEDs have wide viewing angle over 160°, vivid colour purity, thin and flexible devices, and low power consumption. When a forward bias is applied across the device electrons move through the cathode and holes through the anode and recombine thus forming an exciton within the organic semiconductor material. Spontaneous emission occurs through the emission of a photon. The device performance is dependent on effective charge injection into the organic semiconductor material.

1.3. Stability of Organic Light-Emitting Diodes

Long operational device lifetimes are essential for OLED flat panel displays and luminaires to be competitive within the commercial market. Currently OLED lifetimes are lower than that of LED counterparts. I.D. Parker *et al* have completed operational lifetime studies of polymer-based organic light-emitting diodes (P-OLEDs) at several temperature ranges from 25 to 85 °C to understand this issue [162]. They noted that lifetimes around 20,000 h were observed at 85 °C when operated at a constant current and luminance greater than 100 cd/m². However, during continuous operation, thermally activated changes in performance occurred because of PPV polymer degradation experienced from electron passage through this layer (hole transport did not seem to lead to degradation). Y. C. Tsai and J. H. Jou employed a mixed-host double emission layer to achieve a long lifetime, high-efficiency white OLED [163]. The first layer comprised yellow rubrene doped in a mixed host consisting of 50% *N, N* diphenyl-*N, N*-bis-1-naphthyl-1,1-biphenyl-4-4-

diamine (NPB) and 50% 2-(*t*-butyl)9,10-bis(2-naphthyl) anthracene (TBADN). The second layer comprised blue 4,4'-bis[2-{4-(*N,N*-diphenylamino)phenyl}vinyl] biphenyl doped in TBADN. They observed that this device structured exhibited a long lifetime - two or five times that of its pure NPB counterpart. The device stability of P-OLEDs is dependent on the stabilization of charge transport layers and the reduction of oxygen and water vapour migrate into the device.

1.4. Efficiency of Organic Light-Emitting Diodes

The lower efficiency and the short lifetime of blue OLEDs compared to red and green OLEDs, hinders the commercialization of a full-color OLED for general lighting and display purposes [22]. Additionally, the promise of fully-solution processed, and low-cost OLEDs has not yet been realized due to use of costly and brittle vacuum-deposited transparent conducting layers and ridged glass substrates. The lower efficiency of blue (3.5%) OLEDs can be attributed to the difficulty of charge injection into blue-emitting polymers which have low highest-occupied molecular orbital (HOMO) energies (ca. -5.9 eV) and high lowest-unoccupied molecular orbital (LUMO) energies (\sim -2.1 eV) [23]. Common approaches that have been used to remedy these issues are incorporation of a high work function hole injection layer, such as poly(3,4-ethylenedioxythiophene) polystyrene sulfonate (PEDOT:PSS), and a low work function electron transport layer, such as calcium, Ca, or lithium fluoride, LiF, into the device structure [24-26]. Additionally, while total internal quantum efficiency can be optimal (\sim 100% for phosphorescent OLEDs and P-OLEDs) [27], light-extraction efficiency is relatively low (\sim 20 - 31%) [27-29], especially for blue-emitting devices and is a significant barrier to high

efficiency P-OLEDs. The shorter lifetime of blue P-OLEDs is due to a combination of: (1) corrosion of ITO due to the acidity of the PEDOT:PSS layer [30,31] and (2) degradation of PEDOT:PSS and Ca carrier injection properties due to exposure to water vapour and oxygen during device fabrication or operation [32].

Proposed approaches to tackling lifetime and efficiency issues are: (1) inverted device configurations [32]; (2) improved encapsulation methods [33] and (3) light management approaches, such as use of top-emitting device architectures, and addition of metallic or dielectric nanostructures to promote more efficient light-extraction [34]. While these approaches have been shown to have the potential to increase device efficiency and operational lifetime [32-34] they may, in turn, effect the overall cost and environmental impact. Thus, further research must be completed before any definitive conclusions (regarding the practical potential of these approaches) can be drawn.

1.5. Cost of Organic Light-Emitting Diodes

Organic light-emitting diodes (OLEDs) are being investigated as alternative display and lighting options because of their low temperature growth conditions and potential earth-abundant constituent elements (while phosphorescent OLEDs contain rare-earth elements to harvest triplet excitons, fluorescent OLEDs with conjugated-polymer active layers are composed primarily of carbon and hydrogen). However, current small-molecule OLEDs on the market are fabricated under high vacuum using thermal deposition thus making the fabrication process expensive [0]. For example, current OLED luminaires are \$1000-2000 for 1m² emitting areas. Therefore, low-cost, large-scale fabrication options

are needed to make OLED technologies marketable. Polymer light-emitting diodes (P-OLEDs) are an emerging sub-section of OLED technologies that offer solution-based processability which may enable even more straight-forward fabrication, recycling, and biodegradability of the device compared to small-molecule based OLED and, hence, lower cost and greater sustainability [18-21].

1.6. Thesis Overview:

The objective of this thesis is to study various OLED device architectures, using theoretical and experimental methods, to determine efficiency and stability enhancement approaches, with consideration for economic and environmental impacts. In Chapter 2 an economic, efficiency, and environmental assessment of four different P-OLED device configurations: bottom-emitting conventional, bottom-emitting inverted, top-emitting conventional and top-emitting inverted devices with regards to the following metrics: device cost, yearly operating cost, optical power cost and CO₂ emissions. For context, the metrics for the P-OLED devices are compared to those for a ubiquitous blue inorganic LED device architecture. In Chapter 3, an experimental investigation of the photoluminescence (PL) stability, PL lifetime, and PL quantum yield of conjugated polymer:organometallic, blue, phosphorescent thin-films blends on silver metasurfaces is carried out in comparison to corresponding data for the organic phosphorescent thin-film blend on planar silver films. Certain silver metasurfaces are found to have the ability to increase the radiative decay rate of triplet emission from the blue organic phosphorescent thin-films and this results in an improvement in the stability of the emission. In Chapter 4, theoretical electromagnetic simulations are used to assess the light-extraction efficiency four different P-OLED

configurations: conventional bottom- and top-emitting P-OLEDs and inverted bottom- and top-emitting P-OLEDs. Finally, in Chapter 5, the findings and main conclusions of the thesis are summarized and future directions on the life-cycle assessment of OLEDs and on further approaches to improving to light-extraction efficiency and stability are discussed.

Chapter 2.

Cost, Energy, and Emissions Assessment of Organic Light-Emitting Device Architectures

2.1 Abstract

Proponents for sustainable alternative lighting and display options advocate for organic light-emitting diodes (OLEDs), particularly polymer-based organic light-emitting diodes (P-OLEDs), because of their potential for low-cost fabrication, more versatile device formats and lower power consumption compared to traditional options. Here, an economic, energy and CO₂ emissions assessment is carried out for four different laboratory-scale, blue-emitting P-OLED device architectures: bottom-emitting conventional; bottom-emitting inverted; top-emitting conventional; and top-emitting inverted. Additionally, comparisons with a standard, commercial-scale, blue inorganic light-emitting diode (LED) device architecture are made. The various P-OLED device architectures are investigated due to their potential to increase operational lifetime (inverted) and light out-coupling efficiency (top-emitting). The following metrics are used in this assessment: device cost, yearly operating cost, optical power cost, CO₂ emissions from device production, and yearly operating CO₂ emissions. We show that the top-emitting inverted device architecture significantly reduces the device cost, yearly operating cost, optical power cost and CO₂ emissions for the P-OLED devices, due to elimination of indium tin oxide and its comparatively high luminous efficacy and longer lifetime. In addition, the top-emitting inverted P-OLED device architecture performs competitively at the laboratory scale with commercial-scale inorganic LEDs for all metrics. However, if

top-emitting P-OLEDs are to be manufactured on a large scale, the luminous efficacy assumed for laboratory-scale devices needs to remain constant throughout development to remain competitive.

2.2 Introduction

OLEDs are being investigated as sustainable alternative display and lighting options, as opposed to compact fluorescent lamps, incandescent lighting, and LEDs because of their low temperature growth conditions and potential earth-abundant constituent elements (while organic phosphorescent OLEDs usually contain rare-earth elements to harvest triplet excitons, fluorescent OLEDs have active layers that are primarily composed of carbon and hydrogen). However, current small-molecule OLEDs on the market are fabricated under high vacuum using thermal deposition, thus making the fabrication process expensive [0-25]. Therefore, low-cost, large-scale fabrication options are needed to make OLED technologies more marketable. P-OLEDs are an emerging sub-section of OLED technologies that are more amenable to solution-based processing which may enable more straight-forward, vacuum-free fabrication of the devices and, hence, lower cost and lower process energy consumption [18,26-29].

However, the lower efficiency (i.e., luminous efficacy) and the shorter operational lifetime of blue P-OLEDs compared to red and green P-OLEDs, slows the commercialization of a full-color P-OLED for general lighting and display purposes [18]. The lower efficiency of blue P-OLEDs can be attributed to the difficulty of charge injection into blue-emitting fluorescent polymers which have low highest-occupied molecular

orbital (HOMO) energies (ca. -5.9 eV) and high lowest-unoccupied molecular orbital (LUMO) energies (ca. -2.1 eV) [30]. Common approaches that have been used to remedy these issues are incorporation of a high-work-function hole injection layer, such as poly(3,4-ethylenedioxythiophene):poly(styrenesulfonate) (PEDOT:PSS), and a low-work-function electron transport layer, such as calcium (Ca) or lithium fluoride (LiF) into the device structure [31-33]. Additionally, while internal quantum efficiency can be optimal ($\sim 100\%$ for phosphorescent OLEDs and phosphorescent P-OLEDs) [34], light-extraction efficiency is quite low ($\sim 20 - 31\%$) [34-36], especially for blue-emitting devices and is a significant barrier to high-efficiency P-OLEDs. The shorter operational lifetime of conventional blue, fluorescent P-OLEDs is due to a combination of: (1) higher drive voltages due to the low light extraction efficiency; (2) corrosion of indium tin oxide (ITO) due to the acidity of the PEDOT:PSS layer [19,37] and (3) degradation of PEDOT:PSS and Ca carrier injection properties due to exposure to water vapour and oxygen during device fabrication or operation [19].

Proposed approaches to tackling efficiency and operational lifetime issues are: (1) light management approaches, such as use of top-emitting device architectures, and addition of metallic or dielectric nanostructures to promote more efficient light extraction [38]; (2) inverted device architectures [39]; (3) improved encapsulation methods [40]. While these approaches have been shown to have the potential to increase device efficiency and operational lifetime [38-40], they may in turn affect the overall cost and environmental impact. Thus, further assessment of these approaches must be completed before any definitive conclusions can be drawn as to their usefulness. The goal of this study is to carry out an cost, energy and CO₂ emissions assessment, based on life-cycle assessment (LCA)

methodologies, for four laboratory-scale, prototypical, fluorescent, blue-emitting P-OLED device architectures (conventional bottom-emitting, inverted bottom-emitting, conventional top-emitting and inverted top-emitting architectures) to determine which architecture is more effective in terms of device cost, operating cost, optical power cost, energy consumption, and CO₂ emissions. Additionally, comparisons are made with the more ubiquitous, commercial-scale, blue inorganic LED device. As discussed earlier, the inverted P-OLED architectures increase the operational lifetime and the top-emitting P-OLED architectures increase the electrical-to-optical power conversion efficiency (i.e., luminous efficacy) [19,24,39].

Several economic and LCA studies have been conducted for LEDs and organic photovoltaic (OPV) devices which form the basis of this study for P-OLEDs [20-23,41-55]. A case study for the LCA of LED downlight luminaires concluded that the environmental impact of LEDs is dominated by the use-stage energy consumption and data gaps exist in LED product manufacturing and its environmental impacts; thus, resulting in a need for further research and assessments in order to compare LED-based luminaires with existing lighting technologies [44]. The U. S. Department of Energy has carried out detailed LCAs of energy and environmental impacts of LED lighting products, which show that the average life-cycle energy consumption is similar for both compact fluorescent lamps and LEDs, with it being greater for incandescent lamps [23]. While economic, energy and environmental assessments have been completed for inorganic LEDs not much emphasis has been placed on the organic counterpart, which motivates this study. We draw comparisons with polymer-based OPV device economic and LCA studies, where applicable, since there have been a significant number of such studies [20-22,38,43-55]

and, while OLEDs and OPV devices are operationally different, their device compositions and architectures are similar. As a result, one can study prior work on OPVs in order to draw inspiration to base future organic polymer-based cost and LCA studies due to the similarities in device structure and material type with the main difference being that polymer-based OPV devices produce electrical energy from sunlight while P-OLEDs consume electrical energy to produce light.

Furthermore, numerous OPV studies have focused on identifying approaches to lower device cost and the effects of increasing the efficiency and operational lifetime on energy and greenhouse gas (GHG) emission metrics that are also pertinent to P-OLEDs. For example, a life-cycle and cost assessment of OPV devices by Emmott et al. explored various transparent conductor alternatives to ITO in which they found that material alternatives, such as silver nanowires and high-conductivity PEDOT:PSS, have the potential to reduce the energy-payback time (EPBT) and financial cost of organic photovoltaic devices [20]. Espinosa et al. conducted a LCA of organic tandem solar cells where they investigated the economic and environmental feasibility of manufacturing a tandem solar cell versus a single junction solar cell. They found that the tandem solar cell has to be 20% better performing than a single-junction device in order to improve cost and sustainability metrics [43]. A review paper by Lizin et al. of LCA studies of OPVs focused on environmental aspects such as cumulative energy demand (CED), EPBT, and the GHG emission factor of single-junction, organic, bulk-heterojunction P3HT:PC₆₀BM polymer-based solar cells [21]. The top environmentally performing solar cell had a CED of 37.58 MJ/m², EPBT of 3.54 - 6.24 months, and cell efficiency of 2% with lower GHG emission factors than current power plants. They concluded that the often-used linear relationship

between increasing operational lifetime or efficiency and improved sustainability, CED and EPBT, is not a sufficient model because improvements in these areas are heavily dependent on the device materials and architectures [21]. Darling et al. conducted a LCA to estimate the CO₂ emission factor for a 1 m² OPV device, with 1% solar power conversion efficiency (PCE) and 2-year operational lifetime (which are achievable today), and a hypothetical future OPV device with 15% PCE and a 20- year operational lifetime [22]. They estimated a ~10% decrease in CO₂ emissions due to the increase in PCE and the longer operational lifetime. Furthermore, they suggest that improvements can be made to operational lifetime through encapsulation with materials with low water and oxygen transport rates and use of air-stable alternative materials. Additionally, in order to transfer OPV technology from laboratory-scale to larger scales for commercialization, efficiency, scalability of manufacturing processes, and knowledge of degradation mechanisms and their impacts on operational lifetime are critical factors that have been identified through economic and LCA studies [21,22 ,45 -55].

The aforementioned OPV studies allow us to draw some conclusions that are applicable to P-OLED devices, such as: eliminating ITO from the device architectures, increasing multilayer device performance, and use of stable device materials and encapsulants should assist in making P-OLED performance more comparable with the performance of current LEDs on the market. However, comparisons between certain aspects such as life-cycle CO₂ emissions and cost assessments of photovoltaic devices and light-emitting devices are not appropriate or straight forward. For example, once a photovoltaic system is installed, the main yearly cost is associated with system maintenance, while, for a lighting system there are significant additional costs because it

consumes electricity during operation (as opposed to generating electricity from a free natural resource, i.e. the sun, as in the case of a photovoltaic system). Therefore, in this study some alternative assessment methodologies and metrics that are relevant to P-OLED devices but not to OPV devices are developed.

2.3 Methodology

2.3.1. Goal and Scope

The goal of this study is to carry out an economic and environmental assessment of four prototypical P-OLED device architectures to determine which architecture is more effective in terms of cost, energy consumption, and carbon dioxide emission as compared to the widely-studied conventional bottom-emitting blue P-OLED and conventional inorganic blue LED device architectures. We complete a cradle-to-grave boundary assessment, i.e., from the inception of raw materials to the end of use, of an organic polyfluorene-based blue P-OLED device as there are numerous results reported in the literature for such devices [18,19,23,37,40]. We determine the device cost (per meter squared) including materials and manufacturing costs; operational cost per year of continuous use; cost to power the device per lumen; the brightness emitted by the (P)LED for 1 W of electrical input power; and the global warming potential from CO₂ emissions during the entire use phase, from the point of view of the consumer. In this assessment we ignore all transport, installation and disposal phase costs associated with the life-cycle of the P-OLED. The assessment carried out here is meant to provide perspective on the economic and environmental impact of organic P-OLEDs relative to the more mature inorganic semiconductor LED technologies. Additionally, the P-OLED life-cycle stages

and materials which are expected to have the greatest economic and environmental impacts are identified. Furthermore, this assessment will identify target efficiency and lifetimes for P-OLEDs that should be reached for the practical application in display and lighting technologies.

As mentioned in Section 2.2, the goal of this study is to carry out a cost, energy and CO₂ greenhouse gas (GHG-CO₂) emissions assessment, based on LCA methodologies, for four laboratory-scale, prototypical, fluorescent, blue-emitting P-OLED device architectures to determine which architecture is more effective in terms of device cost, operating cost, optical power cost, energy consumption, and CO₂ emissions. LCA is used as a tool to assess the energy and environmental impacts of a product, process or activity throughout its life cycle; from the extraction of raw materials through to processing, transport, use and disposal [20,21,23,41-58]. LCA is a standard international ISO 14040 series method that consists of four distinct components: (1) goal and scope, (2) inventory analysis, (3) impact assessment, and (4) interpretation. First, the aim of the study, central assumptions, and system boundaries are chosen. Next, during the life-cycle inventory analysis (LCI) phase, the inputs and outputs for the emissions and resources are quantified. Then a life cycle impact assessment (LCIA) is conducted to evaluate the potential environmental impact of the previous quantified values. Finally, an interpretation of results are presented in a clear concise manner [43,57,58].

We complete cradle-to-grave assessment, i.e., from the inception of raw materials to the end of use, of a fluorescent, blue-emitting P-OLED device (i.e., one that uses, for example, a polyfluorene-based light-emitting active layer) as there are numerous results reported in the literature for such devices [0,19,24-30] (Figure 2.1).

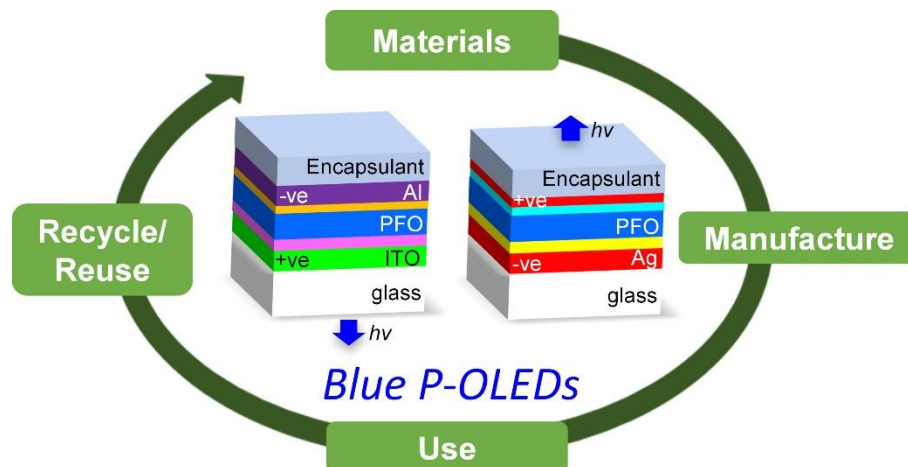


Figure 2.1: Schematic of life cycle assessment, from the inception of raw materials, to manufacturing of the device, device use, and recycling or reuse of the device. The structure of blue P-OLEDs, bottom-emitting conventional and top-emitting inverted, are shown in the center.

As discussed in Section 1, while photovoltaic studies can be used as a guide to base LCA studies of light-emitting devices on, they differ in terms of their operation. Unlike OPVs, P-OLEDs consume electrical power for operation and produce optical power (i.e., light). As a result, the functional unit should be determined by the basis of the optical power produced, which in this case we are assuming to be the brightness per unit area or luminance. Therefore, here, we employ a luminance of 1000 cd/m^2 as our functional unit which is a commonly reported luminance for OLEDs [18,40,59-66]. Each device architecture is assumed to produce this constant brightness, and in order for this to be achieved either the electrical input power or the power efficiency (i.e., luminous efficacy) of the device can be varied. Note that in contrast, for OPV devices a constant optical input power (or irradiance) is applied during performance testing (i.e., 100 mW/cm^2 (1 sun)); therefore, to generate a particular target electrical power quantity, device area or efficiency

is varied. We determine the following metrics: the device cost per meter squared [$\$/\text{m}^2$], including materials and manufacturing costs; operational cost per year [$\$/\text{yr}$]; cost to continuously generate $1000 \text{ cd}/\text{m}^2$ for one hour [$\$/\text{lm}$]; and the GHG-CO₂ emissions [kg CO_2], for both device production and yearly operation, from the point of view of the user. The assessment carried out here is meant to provide perspective on the cost, energy and emissions impact of blue-emitting P-OLEDs relative to the more mature inorganic semiconductor LED technologies. Additionally, the P-OLED life-cycle stages and materials which are expected to have the greatest cost and emissions impacts are identified.

2.3.2. Central Assumptions

In this study, we completed a cradle-to-grave assessment including the following stages (Figure 2.2.): (1) raw materials extraction and production; (2) P-OLED device fabrication and (3) P-OLED device use. The following inputs and outputs are considered for each stage where relevant: material inputs; electrical energy inputs; GHG-CO₂ emissions outputs and optical energy output, and P-OLED device use stages. A life-cycle inventory is compiled and analyzed for the materials, production and fabrication, and use-phase operating cost of the P-OLEDs in order to carry out the assessment. In this assessment, we ignore all transport, installation, and disposal phase costs associated with the life-cycle of the P-OLED because these costs are assumed to be small compared to device and use-phase costs [20,47,56]. Furthermore, we have not included in the assessment the housing, electrical connections, heat sinks, or other items involved in the mounting of the P-OLED as it is assumed to be similar amongst the different P-OLED architectures regardless of the final product (e.g., lighting, display) because they are all

planar, thin-film surface-emitting optoelectronic devices and the functional unit (i.e., 1000 cd/m²) is the same for each architecture. Conversely, for the inorganic LED different housing, mounting and peripheral components (e.g., electrical connections, heat sinks) could certainly be employed. However, given that the blue inorganic LED is the most ubiquitous blue light-emitting device, it is useful as a standard against which blue OLEDs can be compared (similar to how a silicon solar cell is the standard against which all newer solar cell technologies are compared regardless of eventual differences in mounting, housing, etc. [22]).

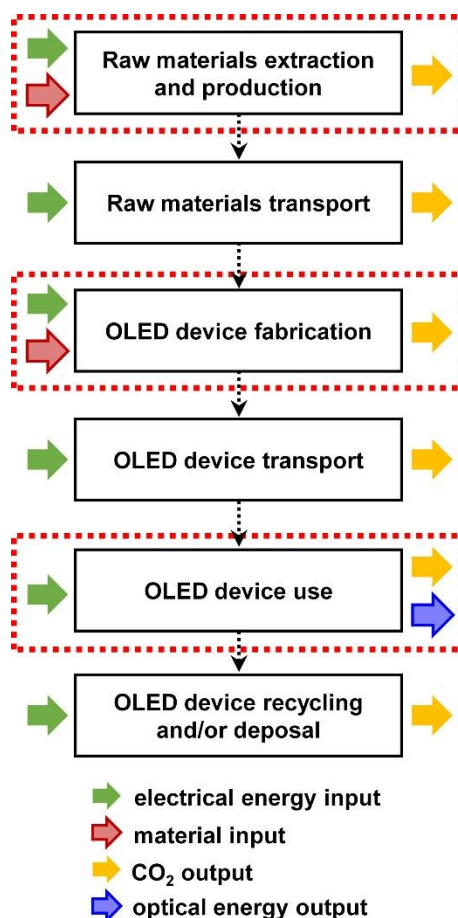


Figure 2.2.: System boundary diagram for a LCA of OLEDs. In this study, the assessment considers only the stages of the life cycle highlighted in by the dashed red boxes: raw materials extraction and production, OLED device fabrication, and OLED device use.

The background system (i.e., the information needed to carry out this study) is defined through extensive reviews of published literature and supplier catalogues. Embodied energy and direct process energy values were obtained from published literature that included relevant embodied energy data from LCA databases such as Ecoinvent and Gabi for the more common materials (e.g., glass, silver). However, in some cases, material embodied energy values were assumed values based on more commonly-available materials within the same material class. For example, material embodied energies for poly(3-hexylthiophene) were used instead of those for poly(9,9-dioctylfluorene), PFO, for the organic conjugated polymer active layer due to lack of available embodied energy data for PFO. This is a reasonable approach because both P3HT and PFO are conjugated (i.e., semiconducting) polymers that have rigid molecular backbones that consist of molecular monomers or long chains of carbon-based repeat units connected by covalent bonds. In addition, both polymers are synthesized from a solution in a similar catalytic fashion [67,68]. The dollar per gram (\$/g) data for materials was obtained from supplier online catalogues and from published literature. References to the source websites (including date accessed) and the relevant papers are included at the appropriate location for each \$/g value. For the thickness of layers in the different P-OLED devices (Tables 2.1. and 2.2.), information was obtained from published literature in which device prototypes were fabricated and tested, as well as Department of Energy solid-state lighting technical reports (referenced below).

The performance parameters (Table 2.3.) are essential to calculating the metrics defined in Section 2.3 used for the assessment of the different device architectures, which

comprise the foreground system. Note that only lab-scale and pilot-scale fluorescent blue polymer OLED devices have been reported to date. Therefore, all of the metrics for the OLED devices are for lab/pilot-scale devices. First, the average operational lifetimes of conventional blue fluorescent OLEDs were determined from references [18,59,60]. Then, based on publications in which direct comparisons between the lifetime of a conventional and inverted OLED were made [61,62], a scaling factor was determined. From this assessment we found that the inverted OLEDs have operational lifetimes that are 1.75 times longer than the conventional OLEDs. We then multiplied the average conventional operational P-OLED lifetime by the scaling factor to determine the inverted OLED operational lifetimes for both bottom and top emitting device structures.

The luminous efficacy values were calculated in a similar fashion to the operational lifetime. To determine the luminous efficacy values for the different device architectures, first, we averaged the luminous efficacy values for conventional bottom emitting fluorescent blue OLEDs from references [26,60,68] at a luminance of 1000 cd/m². Then, in a similar way to how the operational lifetime of the inverted devices was determined, a scaling factor was taken from reports that directly compared inverted to conventional bottom emitting OLEDs [61,70-73], top emitting to bottom emitting conventional OLEDs [74], and the top emitting to bottom emitting inverted OLEDs [72,75-77]. We then used these scaling factors to calculate the efficacy values from the averaged conventional bottom emitting OLED luminous efficacy for each device configuration. Note that the luminous efficacy value of the inorganic LED was based on reported values for mass-produced inorganic LEDs that included light extraction structures and housing [64,66,78-81], which may aid in increasing efficacy values.

2.3.3. Definition of Metrics

The metrics for this assessment are as follows: (1) device cost (per m²), C_{dev} [\$/m²], which is the upfront cost to the user at the initial purchase; (2) yearly operating cost, C_{op} [\$/yr], which is the cost to operate the device for 8 hours per day over a one year period; (3) optical power cost, C_{lm} [\$/h], which is the cost required to generate the functional unit of 1000 cd/m² of optical power for one hour; (4) GHG-CO₂ emissions from raw materials extraction and device manufacturing, $GHG-CO_{2,dev}$ [kg-CO₂/m²]; (5) yearly GHG-CO₂ emissions produced from a device operating for 8 hours per day, $GHG-CO_{2,op}$ [kg-CO₂/yr]. We define C_{dev} as:

$$C_{dev} = C_{mat} + C_{man} \quad (1)$$

where C_{mat} is the materials cost for all device layers and C_{man} is the manufacturing cost. Estimation of C_{mat} for each device architecture studied here will be discussed in the next section using information obtained from materials suppliers and is the largest contribution to C_{dev} .

C_{man} is determined from a percentage range of the total device cost typically found for solution-processed OPV device manufacturing costs on the lab/pilot scale, i.e., 21 % - 40 % [22,43,45-67]. Note due to the current state of P-OLED development, large-scale manufacturing methods and practices are currently not optimized or standardized. Additionally, comparisons between manufacturing costs for reel-to-reel processed devices and manufacturing costs for devices fabricated on ridged substrates have shown only a slight increase in the percentage contribution of manufacturing costs to total device costs

(~50 % is an upper estimate for OPV devices on glass substrates compared to 21 - 40 % for OPV on PET substrates). Therefore, we have assumed an average percent contribution of manufacturing costs to total device costs of 30% [22,43,45-67]. Therefore, to determine C_{man} , such that C_{man} contributes to 30% of C_{dev} , C_{man} was taken to be a 43% of C_{mat} . We do not account for possible differences in manufacturing costs between lighting and display P-OLED technologies such as types of capital equipment (e.g., spray coaters versus ink-jet printers). However, in both cases the active layer, hole transport layer (HTL) and ETL are assumed to be fully solution processed on glass [27,28]. Additionally, as stated earlier, this study focuses on device costs – costs associated with P -OLED housing, electrical connections, heat sinks and electronic drivers (i.e., balance of system costs) are not included.

We define C_{op} [\$/yr] as:

$$C_{op} = \frac{C_{use}}{L} * 8 * 365 \quad (2)$$

where L [h] is the operational lifetime of the device and C_{use} [\$] is the use-phase cost. L is taken to be the time it takes for the luminous efficacy [lm/W] to drop to 50% of its initial value [84]. C_{use} is the cost of operation for a 1 m² device over the device's operational lifetime and is defined as:

$$C_{use} = C_{elec} * E_{use} \quad (3)$$

where C_{elec} is taken to be the cost of electricity in the United States (assumed to be 0.0984 \$/(kW h) [85]), and E_{use} is the use-phase energy consumption [kW h] defined as:

$$E_{use} = \frac{P_{in} * L}{1000} \quad (4)$$

where P_{in} is operating electrical power [W] for a 1 m² device. P_{in} is calculated as follows:

$$P_{in} = \frac{P_{out}}{B_f} k \quad (5)$$

where B_f is the luminous efficacy [lm/W] and k is a correction factor, which accounts for the performance degradation of the device over time. Here, we assume a constant applied voltage is applied to each device, therefore, $k = 0.75$ (i.e., on average, the device operates at 75% of its initial luminous efficacy over its operational lifetime, L) [84]. P_{out} is the light output power or luminous flux per m^2 [lm/m²] and is defined as

$$P_{out} = B * \pi \quad (6)$$

where B is luminance [cd/m²] and we have taken it to be 1000 cd/m², as discussed earlier in Section 2.1, as it is the standard value used when reporting operational lifetimes of OLED devices [18,40,57-66]. We assume C_{lm} in \$/h is then calculated as:

$$C_{lm} = \frac{P_{out} * C_{elec}}{B_f * 1000} \quad (7)$$

Next, CO₂ emissions from device production, $GHG-CO_{2,dev}$, which includes the GHG-CO₂ emissions from raw materials and device fabrication in kg CO₂ is defined as:

$$GHG-CO_{2,dev} = (E_{mat} + E_{man}) * I_{CO_2} \quad (8)$$

where E_{mat} , in MJ/m², is the embodied energy of the raw materials in the devices and E_{man} , in MJ/m², is the direct process energy consumed during device manufacturing. E_{man} , which is taken to be 1.05 times E_{mat} , is determined from averaged ratios of direct process energy to embodied energy in the material from relevant OPV literature [43, 45-47]. The average CO₂ emission intensity from fossil fuels, I_{CO_2} , between 1997 and 2012 for the United States from electricity generation is taken to be 1.90 kg CO₂/(kW h) (equal to 0.53 kg CO₂/MJ) [86]. Finally, yearly operating CO₂ emissions, $GHG-CO_{2,op}$, which is

the yearly GHG-CO₂ emissions produced from a 1 m² device operating 8 hours per day (in kg CO₂/yr) is defined as:

$$GHG-CO_{2,op} = \frac{(E_{use} * I_{CO_2} * 8 * 365)}{L} \quad (9)$$

2.4 Results and Discussion

2.4.1. Life-Cycle Inventory - Device Architectures and Materials

The bottom-emitting conventional P-OLED was analysed initially as a foundation with which to compare the bottom-emitting inverted, the top-emitting conventional and the top-emitting inverted P-OLED architectures, and the blue inorganic LED. Schematics of the different P-OLED architectures and the inorganic LED are shown in Figure 2.3a-e.

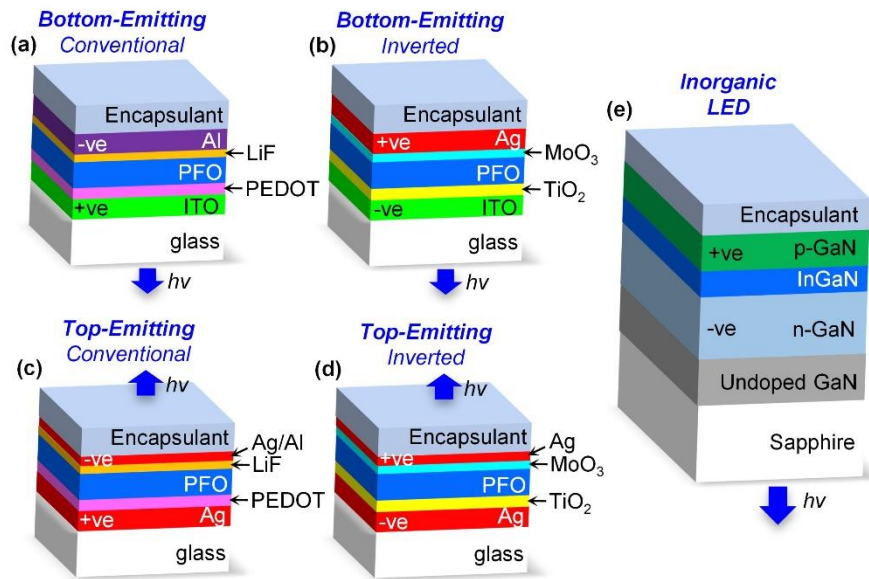


Figure 2.3.: Schematics of: (a) a bottom-emitting conventional P-OLED, (b) a bottom-emitting inverted P-OLED, (c) a top-emitting conventional P-OLED, (d) a top-emitting inverted P-OLED, and (e) a blue inorganic LED. The blue arrows with $h\nu$ (photon energy) labels represent the direction of light emission.

The inventory of materials and average layer thicknesses for each device architecture, obtained from published literature, is included in Table 2.1.

Device Architecture	Thickness (nm)	Function	References
<i>Bottom-Emitting Conventional</i>			
ITO	108 ± 50	Anode	[20,38,66]
PEDOT:PSS	57 ± 13	HTL	[20,38,68,87-91]
PFO	108 ± 45	active layer	[20,38,66,88-92]
LiF	2.3 ± 2	ETL	[20,87,92]
Al	142 ± 53	Cathode	[20,38,66,89,90,92]
<i>Bottom-Emitting Inverted</i>			
ITO	108 ± 50	Cathode	[20,38,66]
TiO ₂	45 ± 40	ETL	[93,94]
PFO	108 ± 45	active layer	[20,38,66,88-92]
MoO ₃	11 ± 7	HTL	[24,66,93-100]
Ag	35 ± 30	Anode	[98-100]
<i>Top-Emitting Conventional</i>			
Ag	125 ± 29	Anode	[24,74,101]
PEDOT:PSS	57 ± 13	HTL	[20,38,66,88-92]
PFO	108 ± 45	active layer	[20,38,66,88-92]
LiF	2.3 ± 2	ETL	[20,87,92]
Al	2	Cathode	[101]
Ag	17.8 ± 2.17	Cathode	[24,101]
<i>Top-Emitting Inverted</i>			
Ag	125 ± 29	Cathode	[24,74,101]
TiO ₂	45 ± 40	ETL	[93,94]
PFO	108 ± 45	active layer	[20,38,66,88-92]
MoO ₃	11 ± 7	HTL	[24,66,93-100]
Ag	17.8 ± 2.17	Anode	[24,101]
<i>Blue Inorganic LED</i>			
Sapphire	10 ⁶	Substrate	[102,103]
undoped GaN	600	buffer layer	[102,103]
n-doped GaN	1500	ETL	[102,103]
p-doped GaN	500	HTL	[102,103]
InGaN	200	emitter layer	[102,103]

Table 2.1. Table of bottom-emitting (conventional and inverted) and top-emitting (conventional and inverted) P-OLED device layer materials, layer thicknesses and corresponding layer functions.

The thickness values are an average of values reported in the corresponding referenced literature

with the standard deviation shown after the average value. Glass substrates with thickness of 0.192 mm were assumed for all P-OLED device architectures.

2.4.2. Cost Assessment

2.4.2.1. Device Cost

To determine the C_{dev} , we first carried out materials cost calculations to determine C_{mat} using the mass per m^2 for each layer of the device and material cost per gram as shown in Table 2.2. Using the data obtained from Table 2.2, the estimated price for each layer in a 1 m^2 device was calculated as follows:

$$\text{Estimated price per layer} = m \times l_p \quad (10)$$

where m = material mass [g/m^2] and l_p = price per layer [$\$/\text{g}$].

Materials	Mass/Unit Area (g/m^2)	Cost per gram ($\$/\text{g}$)	Cost Per Layer ($\$/\text{m}^2$)				
			Bottom-Emitting P-OLED		Top-Emitting P-OLED		Inorganic LED
			Conventional	Inverted	Conventional	Inverted	
Glass [^]	474.24	0.09	42.92	42.92	42.92	42.92	-
ITO	0.73 ± 0.34	114	$83.68 \pm 38.53^{\#}$	$83.68 \pm 38.53^*$	-	-	-
Al [*] (142 nm)	0.38 ± 0.14	0.24	0.09 ± 0.03	-	-	-	-
Al [*] (2 nm)	0.005	0.24	-	-	0.001	-	-
Ag [#] (35 nm)	0.37 ± 0.32	6.39	-	2.35 ± 2.01	-	-	-
Ag (17.8 nm)	0.19 ± 0.02	6.39	-	-	$1.19 \pm 0.15^*$	$1.19 \pm 0.15^{\#}$	-
Ag (125 nm)	1.31 ± 0.30	6.39	-	-	$8.38 \pm 1.94^{\#}$	$8.38 \pm 1.94^*$	-
PEDOT:PSS ^x	0.06 ± 0.01	9.02	0.52 ± 0.12	-	0.52 ± 0.12	-	-
MoO ₃ ^x	0.05 ± 0.03	10.84	-	0.57 ± 0.36	-	0.57 ± 0.36	-
PFO ⁺	0.11 ± 0.05	391	43.79 ± 18.38	43.79 ± 18.38	43.79 ± 18.38	43.79 ± 18.38	-
LiF ⁻	0.01 ± 0.005	31.30	0.19 ± 0.16	-	0.19 ± 0.16	-	-
TiO ₂ ⁻	0.19 ± 0.17	3.16	-	0.59 ± 0.53	-	0.59 ± 0.53	-
Sapphire [^]	398	0.52	-	-	-	-	206.96
GaN	15.99	17.55	-	-	-	-	280.62
GaN ⁺	0.86	17.55	-	-	-	-	15.11
InN ⁺	0.41	188	-	-	-	-	76.89
Encapsulant	-	-	11.49	11.49	11.49	11.49	11.49
C_{mat} ($\\$/\text{m}^2$)			182.68 ± 57.22	185.39 ± 59.81	108.48 ± 20.75	108.93 ± 21.36	591.07

Table 2.2. The mass of each layer for a 1 m^2 device, the material dollar per gram ($\$/\text{g}$) values and the cost of each layer ($\$/\text{m}^2$) in a particular device are represented for bottom-emitting conventional

P-OLED, bottom-emitting inverted P-OLED, top-emitting conventional P-OLED, top-emitting inverted P-OLED, and blue inorganic LED architectures [104-113]. Only the materials that are used in a particular device architecture are represented in the respective column. The cost per layer for the encapsulant is a generic value take from Ref. [48]. Each material layer function is represented by the following superscript characters: [^]substrate, [#]anode, ^xHTL, ⁺active layer, [~]ETL, ^{*}cathode.

By adding the estimated price for each layer (calculated using Equation 10) we determined the estimated C_{mat} of a 1 m² device (excluding manufacturing costs) for each architecture: \$183 ± 57 (bottom-emitting conventional); \$185 ± 60 (bottom-emitting inverted); \$108 ± 21 (top-emitting conventional); \$109 ± 21 (top-emitting inverted); and \$591 (inorganic blue LED). In this way the contribution of each layer to the overall C_{mat} amount for each device could be examined.

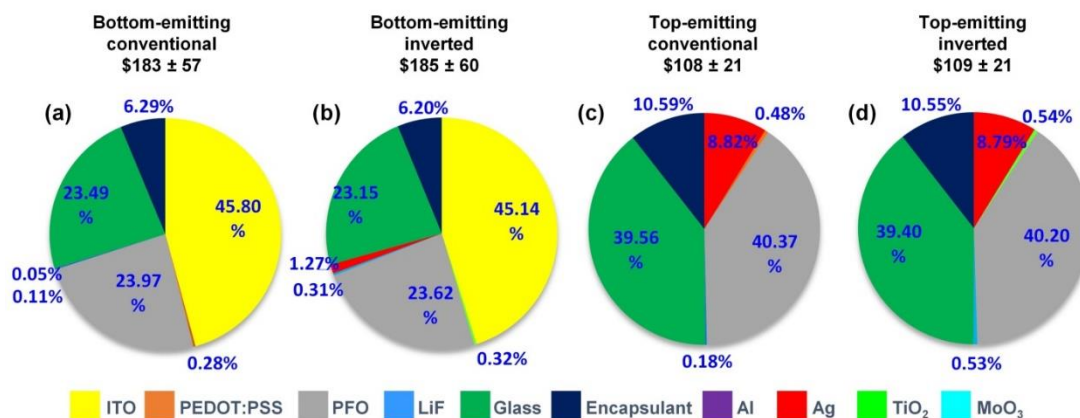


Figure 2.4.: The percentage cost for each layer in the: (a) bottom-emitting conventional P-OLED; (b) bottom-emitting inverted P-OLED; (c) top-emitting conventional P-OLED; and (d) top-emitting inverted P-OLED. The materials cost, C_{mat} , for each device (1 m²) is shown above the corresponding pie chart (i.e., manufacturing costs, C_{mat} , not included).

As shown in Figure 2.4 the ITO, PFO and glass layers contributed the most to C_{mat} for bottom-emitting P-OLEDs (approximately 45%, 24% and 23%, respectively) and the PFO and glass layers contributed the most to C_{mat} for top-emitting P-OLEDs (both $\sim 40\%$). Despite layer thicknesses of only ~ 100 nm for both ITO and PFO (Table 2.1) they were the most expensive materials, per gram, hence the significant percentage contribution to C_{dev} . Conversely, glass was one of the cheapest materials per gram; however, it was also the thickest layer (0.192 mm) which resulted in the significant overall cost per square meter. The metal layers (Ag and Al) accounted for less than 9% of the total cost of the materials in the devices. The ETL and HTL layers were negligible in cost compared to the other layers. As a result, there was very little change in cost on going from a conventional to an inverted device architecture. However, since the top-emitting architectures eliminated ITO, the value of C_{mat} was reduced by $\sim 41\%$ compared to the bottom-emitting devices. $C_{mat} = \$591$ for the blue inorganic LED device architecture (1 m² device), with C_{mat} calculated in a similar fashion to the P-OLED architectures (see Figure 2.2 and Table 2.1). Therefore, C_{mat} for the blue inorganic LED was 5.4 times more than that of the top-emitting P-OLED architecture. This makes the top-emitting architecture a viable option in terms of C_{mat} for solid-state lighting or display applications. C_{dev} , which included a material cost, C_{man} , that was calculated as a percentage of C_{mat} (43 %) such that C_{man} contributed to 30% of C_{dev} (see Section 2.3.3), was then determined and the assessment of C_{dev} is included in Section 2.4 below.

2.4.2.2. Use-Phase Cost

We now determine the performance data (operational lifetime and luminous

efficacy) obtained from the literature for each device architecture (Table 2.3) and how much it would cost to electrically power each architecture in the United States (cost of electricity of 0.0984 \$/(kW h)[85]) over the useful life of each device, i.e., the use-phase cost (C_{phase}) using Equations 3-6.

Performance Parameters	Bottom-Emitting P-OLED		Top-Emitting P-OLED		Inorganic LED	Sources
	Conventional	Inverted	Conventional	Inverted		
L (h)	16,000	28,000	16,000	28,000	50,000	[18,40,57-62,66]
B_f (lm/W)	2.5	3.8	5.1	7.8	7.5	[26,60-81]

Table 2.3: The operational lifetime, L , and luminous efficacy, B_f , are represented for the bottom-emitting conventional P-OLED, bottom-emitting inverted P-OLED, top-emitting conventional P-OLED, top-emitting inverted P-OLED and blue inorganic LED.

As shown in Table 2.3 the inverted P-OLED architecture has an approximately 75% longer operational lifetime than the conventional P-OLED architecture (9.6 years compared to 5.5 years, assuming the P-OLED device operated for 8 h per day). The top-emitting inverted device is the most energy efficient of all of the devices (luminous efficacy of ~7.8 lm/W), and consumes at least 1.5 times less power than the other P-OLED architectures during operation. However, the blue inorganic LED has a factor of 1.8 longer operational lifetime than the longest operating P-OLED (17.1 years for the inorganic LED). Using the operational lifetime and luminous efficacy values reported in Table 2.3 along with Equations 3-6, the use-phase cost (C_{phase}) for each architecture was determined; see Figure 2.4.2.3.

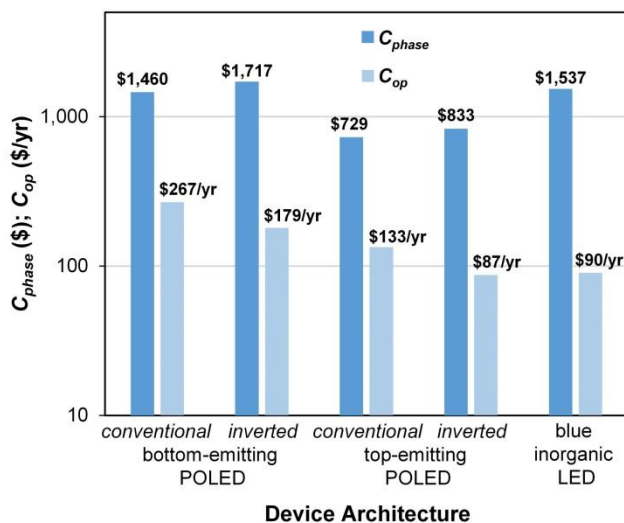


Figure 2.5: The corresponding C_{use} and C_{op} values for each P-OLED device architecture and a blue inorganic LED.

We find that the bottom-emitting inverted P-OLED device had the highest use-phase cost (\$1,717; see Figure 2.5) of all of the devices and the top-emitting conventional device had the lowest use-phase cost of the P-OLED devices (2.4 times smaller than the bottom-emitting inverted architecture) primarily due its higher luminous efficacy and shorter operational lifetime (Table 2.3). The use-phase cost of the blue inorganic LED was ~2.1 times greater than the top-emitting conventional P-OLED (\$729 and \$1,537, respectively) primarily due to its longer operational lifetime (50,000 h). When the use-phase cost is normalized by the device operational lifetime, we obtain C_{op} , the operating cost per year, for each device (Figure 2.5). The top-emitting inverted P-OLED had the lowest operating cost of all P-OLEDs (\$261/yr) and cost \$8/yr lower than the blue inorganic LED (\$269/yr) due to the higher luminous efficacy of the former (7.79 lm/W).

2.4.2.3. Economic Impact

The following metrics are presented in Table 2.4 for 1 m² light-emitting devices: C_{dev} , C_{op} and C_{lm} . C_{dev} (i.e., including materials and manufacturing costs) was the lowest for the top-emitting P-OLEDs and was approximately 5 times cheaper than the blue inorganic LED.

Device Architectures	C_{dev} (\$)	C_{op} (\$/yr)	C_{lm} (\$/h)
Bottom-emitting Conventional P-OLED	261 ± 82	267	0.12
Bottom-emitting Inverted P-OLED	265 ± 85	179	0.08
Top-emitting conventional P-OLED	155 ± 30	133	0.06
Top-emitting Inverted P-OLED	156 ± 31	87	0.04
Inorganic LED	844	90	0.04

Table 2.4. The metrics C_{dev} , C_{op} and C_{lm} , for each P-OLED device architecture and the blue inorganic LED (device areas are 1 m² in all cases).

This indicates that the top-emitting P-OLEDs are the most attractive device type in terms of up-front costs to the user. The top-emitting inverted P-OLED had the lowest C_{op} of all of the devices due to its high luminous efficacy (Figure 2.5), while the bottom-emitting conventional P-OLED had the highest C_{op} . For C_{lm} , the top-emitting conventional architecture (0.04 \$/lm) was the best performing of the P-OLEDs and cost the same as the blue inorganic LED. In short, the top-emitting inverted P-OLED is the most promising P-OLED device architecture in terms of total cost because: (1) it eliminates one of the most expensive layers (ITO) in the device composition; and (2) it has high luminous efficacy in

comparison to the other P-OLED device architectures. Furthermore, while the top-emitting P-OLED architecture has a slight advantage over the blue inorganic LED in terms of C_{op} , it is significantly cheaper in terms of C_{dev} (~5 times cheaper). Therefore, even considering the longer lifetime of the inorganic LED (1.8 times longer), the top-emitting P-OLED would still have a lower total cost when factoring in lifetime and replacement device costs (neglecting P-OLED housing and light extraction structures).

2.5. Energy and CO₂ Emissions Assessment

2.5.1. Device Embodied Energy

Powering light-emitting optoelectronic devices is tied to GHG emissions through the indirect production of CO₂ during electricity consumption. Furthermore, GHG emission is linked to the use-phase energy of the P-OLED devices, which is expected to be the most significant energy-consumption stage of the P-OLED life-cycle. As referenced in the Department of Energy study on lighting technology it has been shown that the use phase is the largest contributor to the overall energy consumption of such devices as fluorescent, incandescent, and LED lamps [23]. To illustrate this point, we determined the embodied energy, E_{mat} , in 1 m² P-OLED devices using literature values for the embodied energy of each constituent layer material and the mass of each layer of the device (Table 2.5).

Materials	Embodied Energy (MJ/kg)	Source
ITO	355753	[46,47]
PEDOT:PSS	131	[46,49]
PFO*	1843	[46,49]
LiCl [#]	220	[119]
Al	171	[41]
Ag	128	[120]
MoO ₃	80	[49]
TiO ₂	118	[49,120,121]
Glass	16	[41]
Encapsulant (1 m ²)	10 [‡]	[47]

Table 2.5: Embodied energy in MJ/kg of materials in P-OLED devices.

*Data for P3HT used here as an approximation for PFO (PFO embodied energies not available), [#]LiCl used here instead of LiF as embodied energy data was limited for LiF; [‡]value is in units of MJ/m²

As can be seen in Table 2.5, ITO and PFO have the highest embodied energies ~ 355,753 MJ/kg and ~1,843 MJ/kg respectively. We then accounted for the mass of each layer in each P-OLED architecture (Table 2.6).

Layer	Bottom-Emitting P-OLED		Top-Emitting P-OLED	
	Conventional	Inverted	Conventional	Inverted
ITO	45.89	45.89	-	-
PEDOT:PSS	0.008	-	0.008	-
PFO	0.207	0.207	0.207	0.207
LiCl [#]	0.001	-	0.001	-
Al	0.078	-	-	-
Ag	-	0.047	0.192	0.192
MoO ₃	-	0.004	-	0.004
TiO ₂	-	0.022	-	0.022
Glass	39.52	39.52	39.52	39.52
Encapsulant	9.96	9.96	9.96	9.96
Total (E_{mat})	95.67	95.65	49.90	49.93

Table 2.6: Embodied energy (in MJ) from raw material extraction per layer of material in 1 m² P-OLED devices (direct layer process energy not included).

The resulting embodied energies for 1 m² P-OLED devices were ~96 MJ and ~50

MJ for the bottom-emitting and top-emitting P-OLEDs, respectively. The major contribution to the larger bottom-emitting device embodied energy was ITO, making up approximately 48% of the embodied energy. The other layers that exhibited significant embodied energies were the glass and encapsulant layers (~39 MJ and 10 MJ, respectively); however, these were still significantly smaller than the ITO embodied energy (which was almost 46 MJ). Additionally, the embodied energies of all P-OLED devices were approximately an order of magnitude smaller than the embodied energy estimated for the inorganic LED (4,650 MJ from Ref. 41). However, the total device embodied energy (E_{mat}) for each P-OLED architecture was substantially lower than the use-phase energy (E_{use} ; converted to GJ by multiplying its value in kW h by 0.0036) which ranged from 53.4 - 62.8 GJ for the bottom-emitting P-OLEDs, was a value of 26.7 GJ for the top-emitting conventional P-OLED, and was 30.5 GJ and 56.2 GJ for the top-emitting inverted P-OLED and the blue inorganic LED, respectively. Therefore, lowering the use-phase energy should have the greatest effect on reducing environmental impacts caused by energy consumption during operation of the P-OLEDs.

2.5.2. GHG-Carbon Footprint

The CO₂ emissions from device production, $GHG-CO_{2,dev}$, were calculated for the four different architectures and the blue inorganic LED using Equation 8 and the embodied energies for raw material extraction shown in Table 2.6. In addition, $GHG-CO_{2,op}$, was calculated using Equation 9 and the devices' luminous efficacy and operational lifetime values from Table 2.3. Both metrics are displayed graphically in Figure 2.6.

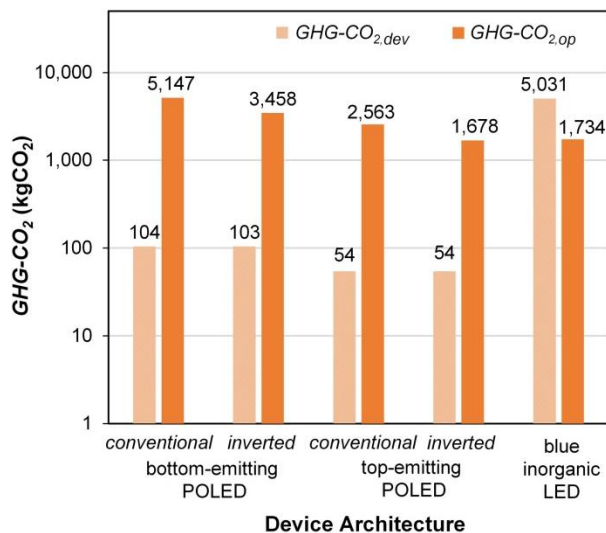


Figure 2.6: The corresponding $GHG-CO_2$ emissions for raw material extraction and device (1 m²) manufacturing ($GHG-CO_{2,dev}$) and yearly $GHG-CO_2$ emissions from operation ($GHG-CO_{2,op}$) for each P-OLED device architecture and the blue inorganic LED.

The $GHG-CO_{2,dev}$ is the lowest for the top-emitting P-OLEDs (54 kg CO₂) due to the low embodied energy for the top-emitting architecture (Table 2.6). The blue inorganic LED had a substantially higher $GHG-CO_{2,dev}$ (5,031 kg CO₂) compared to all of the P-OLED devices due to the large amount energy embodied in the materials and the correspondingly high direct process energy. The $GHG-CO_{2,op}$ was lowest for the top-emitting inverted and blue inorganic LED devices (~ 1,678 kg CO₂/yr and ~1,734 kg CO₂/yr respectively) because they are more efficient at converting electrical input power to light (Table 2.3). The top-emitting inverted P-OLED produced approximately 67% less CO₂ during operation than the bottom-emitting conventional P-OLED. Therefore, the top-emitting inverted is the most promising P-OLED architecture for maintaining a low carbon footprint.

The post-use environmental effects of both P-OLEDs and inorganic LEDs also need to be considered; however, materials toxicity and degradation, as well as materials

recycling, are complex and relatively underdeveloped topics in the context of optoelectronic devices. As a result, data is lacking on the environmental impacts and embodied energy associated with processes being used or under development for disposing of or recycling advanced electronic materials [114]. However, metals can be recycled from both types of devices (including indium, tin, silver, gallium and aluminium) either directly or as a by-product [116]. Costs of purifying the recycled metals is likely to be a compounding issue. Furthermore, it has been shown for OPV the glass substrate can be removed and reused with almost no difference in efficiency, and the polymer layers can biodegrade without leaving harmful elements in the environment [50]. While it would be ideal to recycle the P-OLED and LED devices; the energy required to recycle should be considered. Typically, the energy required to recycle a material is less than that for production of the virgin material [41]. All else being equal, based on the embodied energy (Table 2.6), the energy required to recycle the inorganic LED (4,650 MJ) would still be significantly greater than that of the P-OLEDs (~50-96 MJ) which would make the P-OLED devices the more sustainable choice.

Although recycling removes some of the contaminants; unfortunately, optoelectronic devices (recycling rate of 10%) are not recycled at the same rate as other hazardous consumer products (recycling rate of 24%-90%) [115], and large amounts of optoelectronic materials and devices still end up in landfills or recycling centers where they can adversely affect human health and the environment due to leeching and evaporation of hazardous substances such as heavy metals [117]. The actual amount of hazardous materials depends on the type of optoelectronics, but as a result of these health and environmental risks governmental agencies have begun to regulate optoelectronic

recycling [118].

2.6. Interpretation, Scenario Analysis and Conclusions

2.6.1. Interpretation

While improvements in the operational lifetime of P-OLEDs must be made to be competitive with the comparatively long operational lifetime of inorganic blue LEDs, the top-emitting inverted P-OLED device architecture appears to be the most promising device in terms of projected electrical-to-optical power efficiency, with a high luminous efficacy of 7.79 lm/W compared to the 7.54 luminous efficacy for the inorganic blue LED. Furthermore, the device costs of P-OLEDs were between 3-5 times cheaper than inorganic LED device costs, which would make P-OLED devices more immediately appealing. The embodied energy in the blue inorganic LED was significantly higher than that for all P-OLED device architectures. However, since the embodied energy was only a small fraction (~0.2% for P-OLEDs and 8% for the inorganic blue LED) of the use-phase energy of each P-OLED device, the use-phase was deemed to be the most critical stage to focus on to reduce energy consumption and environmental impacts associated with GHG-CO₂ emissions.

2.6.2. Scenario Analysis

The above interpretation compares laboratory small-scale prototype P-OLEDs to commercial-scale (i.e., mass-produced) blue inorganic LEDs with the P-OLEDs are already cheaper in terms of C_{dev} , and it is likely to remain the case during scale-up of device fabrication. However, OLED large-scale fabrication methods are not well developed and

need to be further refined. One of the current obstacles to widespread commercialization of OLEDs is their overall high cost due to small-scale manufacturing and use of ridged substrates and vacuum deposition methods during the OLED or P-OLED device fabrication. In order to produce P-OLEDs on a large scale and at low cost, the rigid substrate would need to be replaced with a flexible substrate like polyethylene terephthalate (PET) to enable reel-to-reel processing, materials wastage would need to be decreased, and material types and processing methods would need to be reevaluated. For example, the glass substrate contributed ~25% and ~44% (bottom-emitting and top-emitting, respectively) to the C_{mat} and if it was replaced with PET, assuming a thickness of 0.143 mm [47,51,124], and at a cost of ~ \$0.16 per gram, the C_{mat} for each device would be reduced by approximately 6% and 10%, respectively [48]. Furthermore, flexible substrates extend the range of applications for P-OLEDs into not only lighting and standard display options, but also such markets as wearable electronics. In addition, the U.S. Department of Energy estimates that the material utilization rate is as low as 30% for vapour deposition and as high as 90% for solution deposition fabrication [25]. In this study, we did not consider fully solution-based fabrication of all layers, thus the deposition of certain layers (e.g., the metal and ITO) by vacuum methods would result in high amounts of materials wastage and increase the predicated C_{dev} . If we account for wastage, C_{dev} is $\$548 \pm 384$ and $\$561 \pm 225$ for the conventional and inverted bottom-emitting P-OLED architectures, respectively; which represent a factor of 2.1 more than without wastage. However, C_{dev} for the top-emitting device architecture does not increase as significantly when wastage is accounted for because most layers are solution processed (i.e., ITO is eliminated) with C_{dev} increasing only by a factor of 1.25 (to $\$195 \pm 41$) for the top-emitting conventional and inverted device

architectures.

Fully solution processed fabrication of P-OLEDs would require alternative material choices to some of those listed in Table 2.1-2.2. For example, bulk silver would need to be replaced with silver ink. This alternative material would not have much effect on the overall price as the silver layer(s) do not contribute significantly to C_{dev} ; see Figure 2.5. However, full solution processing would only be possible for the top-emitting devices due to the vacuum deposition needed for deposition of ITO for conventional P-OLED devices. In addition, for fully-solution-processed, large-scale production the cost of the materials would decrease by a factor of 2, at least, compared to those reported in Table 2.2 (resulting in C_{mat} of $\$63/\text{m}^2$ - $\$123/\text{m}^2$ for the bottom-emitting P-OLED and $\$44/\text{m}^2$ - $\$65/\text{m}^2$ for the fully-solution-processed top-emitting P-OLED) because of the bulk purchase of material from the suppliers [48-54]. These estimates are on target with estimates reported by Azzopardi et al., Powell et al. and others for the total device cost of a commercial-scale OPV module which ranges from $\$45/\text{m}^2$ to $\$264/\text{m}^2$ [48-54].

When addressing the scalability of OLEDs, changes to device luminous efficacy and operational lifetime are important considerations. Large-scale production is likely to yield devices with lower luminous efficacy and operational lifetimes compared to those for small-scale prototypes, due to the increased likelihood of non-uniformities over large active areas as a result of defects, layer thickness variations and/or electrical shorts [55,125]. Reductions in luminous efficacy, in particular, are expected to increase the yearly operating cost of these P-OLED devices. While it is expected that there will be a reduction in both luminous efficacy and operational lifetime due to large-scale production, P-OLEDs are currently manufactured at the lab- and pilot-scale which makes quantification of the

reduction in performance difficult. Therefore, in order to estimate the efficiency and lifetime reduction caused by large-scale production, we draw comparisons with reports on the commercial scale-up of OPVs. Lab-scale efficiencies for optimized polymer-based OPVs have been reported to be 10% - 12% (fully solution processed and vacuum evaporated) and OPV modules produced using large-scale processing methods are approximately 2% efficient; thus indicating in a factor of up to 6 reduction in efficiency during scale-up [54,55,125]. Consequently, assuming a similar reduction in the luminous efficacy for the top-emitting, inverted P-OLED, luminous efficacy would be reduced to 1.3 lm/W for a device fabricated using large-scale production methods.

Furthermore, we can assume a worst-case operational lifetime of 1 year based on prior studies of OPV devices fabricated by large-scale production methods [126-128,45]. This assumption would reduce the top-emitting inverted P-OLED operational lifetime by a factor of 9.6 (i.e., to 2,920 h). To illustrate the effect of assuming such significant reductions in luminous efficacy and operational lifetime under a “worst-case” large-scale production scenario, we carried out a scenario analysis using the Monte-Carlo method for a top-emitting P-OLED where we calculate probability distributions for C_{op} , E_{use} and $GHG-CO_{2,op}$ under three different scenarios (Figure 2.7), assuming relative standard deviations of the luminous efficacy and operational lifetime of 25% [45,128-134].

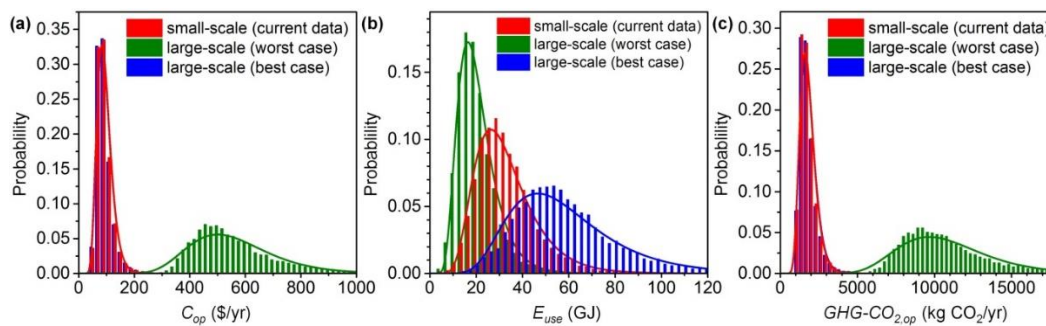


Figure 2.7: Histograms showing the probability distribution of (a) C_{op} , (b) E_{use} and (c) $GHG-CO_{2,op}$ for top-emitting inverted P-OLEDs (1 m^2) generated using the Monte-Carlo method [45] for three different scenarios: small-scale, which assumes luminous efficacy (B_f) and operational lifetime (L) values of 7.9 lm/W and $28,000 \text{ h}$ (as reported in Table 2.3); large-scale (worst case), which assumes a factor of 6 reduction in B_f compared to the small-scale scenario and a $2,920 \text{ h}$ operational lifetime (i.e., 1 year); and large-scale (best case), which assumes a future “best case” large-scale production scenario that results in P-OLEDs with B_f and L values of 7.9 lm/W and $50,000 \text{ h}$, respectively. Normal distributions for B_f and L were generated as inputs for the Monte-Carlo analysis, assuming a relative standard deviation of 25% in B_f and L to represent typical performance parameter variations for polymer optoelectronic technologies. The Monte-Carlo analysis was carried out using Microsoft Excel with 10,000 random sampling iterations of the input distributions employed to calculate the probability distribution for C_{op} , E_{use} and $GHG-CO_{2,op}$.

The first scenario, assumes average luminous efficacy and operational lifetime values achievable using current small-scale production approaches, as reported in Table 3.3. The second scenario assumes “worst-case” luminous efficacy and operational lifetime values reported above due to large-scale production methods. The third scenario assumes a future “best case” scenario in which the luminous efficacy and operational lifetime values at large-scale production are 7.9 lm/W (same as currently-achievable small-scale production value) and $50,000 \text{ h}$ (the operational lifetime of a commercial inorganic LED). Figure 2.5 shows that C_{op} was similar for small-scale and best-case, large-scale production at $94 \pm 33 \text{ \$/yr}$ and was significantly lower than C_{op} for the worst-case, large-scale production ($562 \pm 196 \text{ \$/yr}$), because C_{op} is inversely proportional to luminous efficacy and is insensitive to operational lifetime (as it is calculated on a yearly basis). However, E_{use} , is both inversely

proportional to luminous efficacy and directly proportional to operational lifetime. Therefore, the larger operational lifetime values for best-case, large-scale production resulted in larger E_{use} values (58 ± 26 GJ) compared to the small-scale (33 ± 14 GJ) and worst-case, large-scale production (21 ± 9 GJ). In other words, a given device produced under the best-case, large-scale production scenario consumes significantly more energy than a device produced at small-scale or for the worst-cast, large-scale production scenario, simply because it operates for longer. However, yearly CO₂ emissions, i.e., $GHG-CO_{2,op}$, exhibited a similar trend to the C_{op} data as it is also calculated on a yearly basis (and, therefore, is independent of operational lifetime) with small-scale and best-case, large-scale production scenarios exhibiting the lowest emissions.

Based on these scenarios, it is hypothesized that P-OLEDs would have to be mass-produced with luminous efficacy and operational lifetime values reported for small-scale devices (Table 2.3) in order for them to be viable in terms of the metrics C_{op} and $GHG-CO_{2,op}$ and competitive with commercial inorganic LED counterparts. Luminous efficacy, in particular, is the more critical performance parameter to maintain upon scale-up since the yearly cost and energy to operate P-OLED devices and the yearly CO₂ emissions during operation are significantly greater than for the production of P-OLEDs even under the best-case, large-scale production scenario. For example, the projected best-case C_{op} (\$94/yr) and $GHG-CO_{2,op}$ (~1800 kg CO₂/yr) for top-emitting, inverted P-OLEDs fabricated using large-scale production are greater than the projected C_{dev} (~\$55) and $GHG-CO_{2,dev}$ (~50 kg CO₂) for large-scale production. Therefore, we expect that regular replacement of a P-OLED device would be relatively inexpensive and would have low greenhouse gas impacts - particularly in comparison to a commercial inorganic LED with similar luminous efficacy

(C_{dev} of \$844 and $GHG-CO_{2,dev}$ of $\sim 5,000$ kg CO₂) - thereby making operational lifetime less critical. However, since processing techniques and manufacturing methods have not been standardized for P-OLEDs, it is difficult to draw definitive conclusions on what the projected device performance parameters should be for P-OLEDs upon scale-up. Therefore, studies such as this would have to obtain performance parameter data from optimized large-scale production processes for P-OLEDs (which are still under development) and draw comparisons with performance parameter data from existing optimized laboratory-scale or pilot-scale processes, which may result in currently unforeseen benchmarks [21]. Finally, it should be noted that this study focused only on blue light-emitting P-OLEDs and the metrics would most likely be improved for red and green P-OLEDs due to their higher efficiencies and longer operational lifetimes.

2.7. Conclusions

The aim of this chapter was to complete an economic and environmental assessment of four different laboratory-scale, blue-emitting P-OLED device architectures: bottom-emitting conventional; bottom-emitting inverted; top-emitting conventional; and top-emitting inverted. Further, a comparison with a ubiquitous standard, commercial-scale, blue inorganic LED device architecture was made. The various P-OLED device architectures are investigated due to their potential to increase operational lifetime (inverted) and light out-coupling efficiency (top-emitting). The following metrics are used in this assessment: device cost, yearly operating cost, optical power cost, CO₂ emissions from device production, and yearly operating CO₂ emissions. From a comparison of various P-OLEDs device architectures it was found that the top-emitting inverted P-OLED

architecture is likely to be the most promising device architecture to pursue in terms of achieving operational lifetimes and efficiencies that are competitive with commercially-available blue inorganic LEDs and to achieving fully-solution processed large-scale production. Additionally, the device costs and embodied energies for the top-emitting P-OLEDs were significantly lower than those for the blue inorganic LED, making P-OLEDs already competitive in terms of up-front cost and energy expenditures. Given these factors and the performance parameters (luminous efficacy and operational lifetime) currently-achievable at lab-/prototype-scale, top-emitting P-OLEDs could be adopted for portable optoelectronic technologies (e.g., cell phone displays; indicator lights) due to the relatively short use stage of such technologies and inexpensive materials requirements that allow consumers to dispose of them after only 5-10 years. However, the performance parameters need to remain at current lab-/prototype-scale values during development and scale-up in order to ensure their performance is competitive with inorganic LEDs. Maintaining high luminous efficacy (i.e., electricity-to-light conversion efficiency) upon scale-up will be more important than maintaining long operational lifetimes, since the yearly cost and energy to operate P-OLED devices and the greenhouse gas emissions during operation are significantly greater than for the production of P-OLEDs. Therefore, regular replacement of a P-OLED device would be relatively inexpensive and would have low greenhouse gas impacts; particularly in comparison to an inorganic LED with similar luminous efficacy.

Chapter 3.

Photoluminescence Stability of Blue Organic Phosphorescent

Materials on Silver Metasurfaces

3.1. Abstract

Emerging lighting and display technologies use phosphorescent organic light-emitting diodes (Ph-OLEDs) because they are thinner, more flexible, and less pixelated than their inorganic LED counterparts. As discussed in Chapter 2 conclusions, during scale-up efficiency and lifetime gains are necessary for laboratory/pilot-scale fluorescent P-OLEDs to be a viable option. Thus, it would be imperative for one to complete a stability assessment to determine fabrication methods for a more long-lasting fluorescent P-OLED. A compounding factor is the issue of inefficiency, which is initially enhanced through the use of phosphorescent emitters. While Ph-OLEDs can have an internal quantum efficiency of 100%, on metal electrodes the light-extraction efficiency is 5-30% primarily due to coupling to surface plasmon polariton (SPP) modes and photonic waveguide modes, with SPPs, accounting for up to 50% of the loss in light-extraction efficiency. In addition to low light-extraction efficiency, efficiency “roll-off” in Ph-OLEDs is a significant cause of device degradation at high luminance and is attributed primarily to triplet-polaron and triplet-triplet quenching processes. One way to address the efficiency “roll-off” issue is to accelerate the radiative decay rate of phosphorescence to reduce triplet quenching processes. Further, efficiency “roll-off” in blue Ph-OLEDs is very pronounced due to high triplet energies and significant triplet-polaron and triplet-triplet quenching relative to red and green Ph-OLED counterparts.

The aim of this study is to experimentally investigate the use of silver plasmonic metasurface films to increase the radiative decay rate of triplet emission from blue organic phosphorescent films, and, hence, to minimize triplet quenching processes that cause unstable emission. We use the host poly(N-vinylcarbazole) (PVK) with the blue phosphorescent dopant, bis[2-(4,6-difluorophenyl)pyridinato-C2,N](picolinato) iridium(III) (FIrpic), which is commonly-used in blue Ph-OLED prototypes. This host-dopant combination has been shown to improve light out coupling and enhance triplet excitation because the host assists in charge transport and excitation energy transfer, while the dopant provides color and increases intersystem crossing which improves the internal quantum efficiency (IQE). PVK:FIrpic thin film samples are spin coated onto planar silver, 1D Ag grating (1.6 μm and 0.7 μm), nanoporous (NPO) silver, and nanoparticle (NPT) silver metasurfaces. Each silver plasmonic metasurface is prepared with 50 nm of silver using nanoimprint lithography deposition for 1D Ag grating (1.6 μm and 0.7 μm) and dewetting deposition for NPO and NPT. In addition PVK, FIrpic, and PVK:FIrpic thin films on glass are used as a reference. The silver plasmonic metasurfaces are chosen due to their ability to increase light emission through light scattering and the possibility of intense localized electric near fields arising from localized surface plasmon resonances. These near-field are expected to lead to changes in the decay rate of emission from nearby molecules. The samples are characterized using photoluminescence (PL) stability, PL lifetime, and PL quantum yield measurements to investigate the relationship between silver plasmonic metasurfaces and improved phosphorescence stability. Results have shown a correlation between enhanced PL stability and PL lifetime of silver plasmonic metasurfaces relative to a planar silver surface. In addition, PL quantum yield measurements of

PVK:FIrpic thin films on silver plasmonic metasurfaces relative to planar silver show that NPT metasurfaces result in the greatest improvement in both the stability and efficiency of PVK:FIrpic thin films.

3.2. Introduction

Organic light-emitting devices (OLEDs) are used in next-generation flat panel display devices such as televisions, cell phones, and tablets. They are cheaper, more flexible, thinner, and less pixelated on large screens than inorganic LEDs and liquid crystal displays (LCDs) [135,136]. As discussed in Chapter 2 conclusions, during scale-up efficiency and lifetime gains are necessary for laboratory/pilot- scale fluorescent P-OLEDs to be a viable option. Thus, it would be imperative for one to complete a stability assessment to determine fabrication methods for a more long-lasting fluorescent P-OLEDs. A compounding factor is the issue of inefficiency, which is initially enhanced through the use of phosphorescent emitters. Phosphorescence can harvest singlet and triplet excitons due, in part, to the use of heavy metal atoms in the molecule's structure (which causes spin-orbit coupling), and therefore, phosphorescent OLEDs (Ph-OLEDs) theoretically can emit with 100% internal electroluminescence quantum efficiency (IQE) [137,139,146,159]. However, for fluorescent OLEDs the theoretical IQE is at best 25% due to the prohibition of triplet exciton emission; thus, only singlet excitons are harvested. Therefore, the ideal scenario of high efficiency and long lifetime can only be achieved through the use of phosphorescent materials. However, when operating devices at the industry-standard brightness (i.e., luminance) of 1000 cd/m² or higher, quenching mechanisms can occur due to exciton-exciton and exciton-charge annihilation interactions, thus resulting in a

significant decrease in device efficiency over time [149]. The cause of this efficiency “roll-off” as a function of device operating time has been attributed to: (1) an imbalanced hole-electron current; (2) triplet-triplet exciton annihilation (TTA); and (3) triplet-polaron annihilation (TPA) [145,149-153]. The nonradiative quenching processes TTA and TPA have been ascribed to be the primary loss mechanisms in efficiency roll-off at high luminance [145,149-153]. TTA occurs when there is an accumulation of triplet excitons in a high-energy excited state due to the long lifetime of the emitting triplet state, while TPA occurs when an excited polaron state pairs with a triplet exciton and in both instances the excess energy is lost by thermalization [149-153].

Scientists and engineers have explored mechanisms for improving phosphorescent light emission efficiency to be closer to the theoretical maximum internal quantum efficiency value. While, there has been great success in creating highly-efficient and stable red and green phosphorescent materials; blue phosphorescent materials remains unstable due to TTA and TPA [137,144,146]. Some methods to address efficiency “roll-off” are double emission layers [148,154], alternative high mobility electron transport layers [148,158], and mixed host structures [145,155]; however, further strategies need to be explored because stabilities are still below ~5000 h for blue organic phosphorescent materials. TTA is proportional to the square of triplet exciton density, and the TPA scales with the triplet exciton density [155,158]. During operation the exciton density is proportional to the exciton lifetime [156,158]. Therefore, one way to address the efficiency “roll-off” issue is to accelerate the radiative decay rate (i.e., to decrease the radiative lifetime) of the triplet excitons in phosphorescent OLED materials.

This study aims to experimentally investigate the use of silver plasmonic metasurface films to increase the radiative decay rate of triplet exciton emission from blue organic phosphorescent films. Using this approach, we hypothesize that TPA and TTA processes that cause unstable emission can be reduced. Strong localized electromagnetic fields are created when noble metals, such as silver, are nanostructured which increases the local density of optical states in the near-field (i.e., within 100 nm) of the metal. We hypothesize that by increasing the available local density of optical states that the excitons in the triplet state of the phosphorescent emitter can couple to, the phosphorescence decay rate will increase (i.e., the phosphorescent lifetime will decrease), thus, reducing the probability of TTA and TPA and increasing the phosphorescence stability [147].

3.3. Methods

3.3.1. Sample Set Preparation

Data is reported for measurements carried out on different sets of samples (i.e., “Sets”) and on different days (“Trials”) to check the repeatability of the data, as follows: Sample Set 1 Trial 1 (S1T1), Sample Set 2 Trial 1 (S2T1) and Sample Set 2 Trial 2 (S2T2) Sample Set 2 Trial 3 (S2T3). Initial data is obtained from Sample Set 1 (S1), and the preparation for the phosphorescent film and metasurfaces will be detailed in subsequent sections. Initial photoluminescent (PL) spectra are taken on S1 after which changes are made to S2 (Trial 1 to Trial 3) in order to obtain a more consistent comparison across metasurfaces. In the sections that follow, the methods for fabricating S1 and S2 are described in detail

3.3.2. Preparation of Phosphorescent Organic Thin-Films

To prepare thin films of poly(N-vinylcarbazole) (PVK) containing the blue phosphorescent dopant, bis[2-(4,6-difluorophenyl)pyridinato-C₂,N](picolinato)iridium(III) (FIrpic), first, a host:dopant solution of PVK:FIrpic, was prepared in either a 19:1 ratio (S1) or a 9:1 ratio (S2) (i.e., 10 wt% dopant concentration) to create a 20 g/L solution [145]. For S1, PVK (0.019 g) was added to 1 mL of FIrpic stock solution (0.2 g FIrpic dissolved in 200 mL of chlorobenzene). For S2, PVK (0.3604 g) and 0.0404 g FIrpic was dissolved in 10 mL of chlorobenzene. 5 mL of each were then added into a glass vial to prepare the PVK:FIrpic solution. The 9:1 host:dopant ratio is more consistent with what has been previously shown in the literature for PVK:FIrpic thin films [135139]. The solution was prepared in an amber 2mL glass vial for S1 and 15 mL beaker for S2 that contained a 5 mm x 2 mm polytetrafluoroethylene (PTFE)-coated magnetic stirring rod which assisted in dissolution of the solid. The solution was placed in a water bath on a hotplate and heated to 40 °C with 1000 rpm spin speed for 10 minutes so that the PVK would fully dissolve into the solution. The same method was used to dissolve the FIrpic in chlorobenzene. The PVK:FIrpic solution was then used to prepare PVK:FIrpic thin-film samples to be characterized for sample thickness using the following steps. First, glass microscope slides were cut into approximately 1 cm x 1 cm pieces, and cleaned with the standard glass cleaning procedure as follows: immersed in Sparkleen solution (from a stock solution of 5 g Sparkleen powder in 2 L of deionized (DI) water), sonicated for 15 minutes, rinsed in DI water 3 times, submerged in 50:50 hydrochloric acid and ethanol solution (approximately 60 mL) for 15 minutes, rinsed in DI water 3 times, and dried using an air gun. Then, 50 μ L of the 19:1 PVK:FIrpic solution was spin coated onto the glass

substrates. Spin coating parameters such as concentration, spin speed, spin time, and the amount of solution injected onto the substrate were varied to determine the optimal dynamic spin coating parameters. These were 50 μL drop volume, 20 g/L total concentration, 1000 rpm spin speed, 30 s spin time for S1 and 100 μL drop volume, 20 g/L total concentration, 2000 rpm spin speed, 25 s spin time for S2. Spin coating was used because this method is cheaper, more commercializable, uses less energy, and does not waste as much organic material as thermal evaporation [136,137,138]. Following spin coating, these samples were annealed at 80 $^{\circ}\text{C}$ for 30 min on a hot plate in ambient conditions to remove residual solvent.

The PVK:Firpic thickness was determined from an analysis of the absorption spectra of planar PVK:Firpic films on glass substrates obtained using a SI Photonics CCD Array UV-visible absorption spectrometer. To extract film thickness from absorption spectra, an adapted version of Beer-Lambert's law for solids was employed which consisted of the following equations: $A = \log[1/T]$; $x = \ln[T]/-\alpha$ and $\alpha = 4 \pi k / \lambda$, where α is the absorption coefficient, A is absorbance, T is transmittance, x is PVK:Firpic film thickness, and k is the imaginary part of the refractive index (i.e., extinction coefficient). Using these equations, the measured absorbance spectra and $\alpha = 46,675.1 \text{ cm}^{-1}$ from the literature [135], we found the PVK:Firpic samples to have a thickness of $87 \text{ nm} \pm 3.5 \text{ nm}$ for S1 (which we confirmed with atomic force microscopy (AFM) measurements) and $62 \text{ nm} \pm 8.1 \text{ nm}$ for S2.

3.3.3. Metasurface Preparation

The aforementioned PVK:Firpic solution and spin coating parameters were then used to prepare five PVK:Firpic thin film samples on differing silver (meta)surfaces: planar

silver, nanoimprinted 1D Ag gratings with 1.6 μm pitch and 0.7 μm pitch, nanoporous (NPO) silver, and nanoparticle (NPT) silver. The samples were passivated by bonding a thin glass cover slip to the PVK:FIrpic sample side with UV-curable optical epoxy (Norland 63) in order to reduce photooxidation and photobleaching which can lead to degradation of the PVK:FIrpic emission. For S1, after passivating, the samples were annealed at 80 $^{\circ}\text{C}$ for 30 min. on a hot-plate under ambient conditions with the film side facing up to promote further crosslinking in phosphorescent emitter. However, for S2 post annealing was not carried out after passivating with optical epoxy because the anneal step was found to degrade the PVK:FIrpic emission and to potentially change in phosphorescent emitter morphology.

The Ag metasurfaces were prepared using the following nanofabrication methods. Nanoimprint lithography was employed for fabrication of 1D Ag gratings with 1.6 μm and 0.7 μm pitch. A polydimethylsiloxane (PDMS) silicone elastomer with a base to curing ratio of 10:1 was created through constant mixing to ensure effective crosslinking. Then a cleaned 1.6 μm and 0.7 μm grating disk from a CD or DVD was placed into a petri dish with the viscous PDMS and annealed in an ambient condition oven at 130 $^{\circ}\text{C}$ for 30 minutes. Once cooled the petri dish was removed from the oven and the PDMS mold was removed from the petri dish and cut into 2 cm x 2 cm squares. A poly (methyl methacrylate) (PMMA) resist was created by spin coating PMMA solution onto clean coverslip glass with the following spin coating parameters: 6000 revolutions per minutes, 60 seconds, and 20 μL . The PDMS 2 cm x 2 cm mold was then placed onto the PMMA cover slip glass with imprint side face down to ensure grating transfer. The PDMS mold/ PMMA cover slip was then placed on a metal slab with an additional metal slab with weights placed on top.

It was then placed back into the ambient conditions oven and annealed at 170 °C for 2.5 hours. Once cooled it was removed and was prepared for metal evaporation. Ag was thermally evaporated to a thickness of 50 nm on the PMMA gratings on glass to create the 1D Ag grating metasurfaces.

Thermally-assisted dewetting of silver thin films was employed for the fabrication of NPO and NPT Ag metasurfaces [140] with an effective thickness of 100 nm of silver for S1 and 50 nm of silver for S2. The NPO were fabricated through the following method: 50 nm or 100 nm of Ag was thermally evaporated onto a cover slip glass and the Ag cover slip was placed in an argon filled glovebox; annealed at 200 °C for 20 minutes; and then cooled to room temperature. For NPT Ag for S1, a 100 nm thick Ag film was thermally evaporated onto a glass cover slip and the Ag cover slip was placed into argon glovebox. It was then annealed at 540 °C for 5 minutes to form nanoparticles and then allowed to cool to room temperature. After which it was removed from the glovebox. For NPT Ag for S2, initially, 10 nm of Ag was thermally evaporated onto a glass cover slip and the Ag-covered substrate was placed into an argon filled glovebox. It was then annealed at 540 °C for 5 minutes to form nanoparticles and then allowed to cool to room temperature. After which it was removed from the glovebox and then 40 nm of Ag was thermally evaporated onto the substrate.

While the metasurfaces fabrication methods remained the same for S1 and S2 except for the NPT films, in S2 the volume of metal used to fabricate the metasurfaces was kept consistent across all samples to an effective thickness of 50 nm. This was done in order to minimize back reflections and maintain a similar metasurfaces transmittance, thus reducing the impact metallic film thickness may have on PL spectral results. For all sample

types, the silver metasurface quality and uniformity was investigated with both scanning electron microscopy (SEM) and reflection-mode, dark-field (DF) optical microscopy. Further, UV-visible transmission and DF spectra were used to investigate the optical response of each Ag metasurface.

3.3.4. Characterization Methods

Upon completion of the sample fabrication and optimization, photoluminescence (PL) spectroscopy was used to measure the stability of PVK:Flrpic films on various (meta)surfaces by recording the PL intensity every 2 min. for a total of 30 min. These PL stability measurements were performed with 355 nm laser excitation and a 400 nm long pass filter in the collection optical path. The typical laser power density and repetition rate were approximately 1500 mW/cm² and 1000 Hz but were varied somewhat to obtain a particular luminance at the sample. The appropriate laser power density and repetition rate required to obtain a particular luminance was calculated using the photopic spectral luminous efficiency curve [142]. A non-linear regression fit to the photopic spectral luminous efficiency curve experimental data yields the approximation [142]:

$$V(\lambda) = 1.019e^{-285.4(\lambda-0.559)^2} \quad (3.1)$$

where, $V(\lambda)$, is the photopic spectral luminous efficiency and the wavelength, λ , is in micrometers. We then calculated the luminance, B (in cd/m²), at a wavelength of 450 nm as follows:

$$B = V(\lambda) * n_{PL} * P_w * 683 * \pi \quad (3.2)$$

where (n_{PL}) is the PL quantum efficiency of PVK:Flrpic (chosen to be a value of 51 %), P_w is the average laser power in W/m². The constant 683 converts Watts to lumens and the

factor π converts lumens to candela. The target was a luminance of 1000 cd/m² due to the current stability and lifetime testing targets of OLEDs on the market [18,40,59-66]. The PL spectra were acquired using a Andor Shamrock SR 303i imaging spectrometer with 50 accumulations, and the exposure time for each accumulation was 0.02 s for a 1 s total exposure time (Figure 3.1). The average laser power, P_w , reading was taken during each spectral acquisition step to account for laser fluctuations with time. Planar PVK:FIrpic film on glass and on planar silver were used as control samples (Figure 3.3b- e). The intensity of the 0-1 excitonic transition from the FIrpic emission was extracted from the PL spectra and plotted versus time and then divided by the laser power recorded for each respective PL spectrum. The final PL spectra were intensity normalized to the highest PL peak intensity value (Figure 3.4).

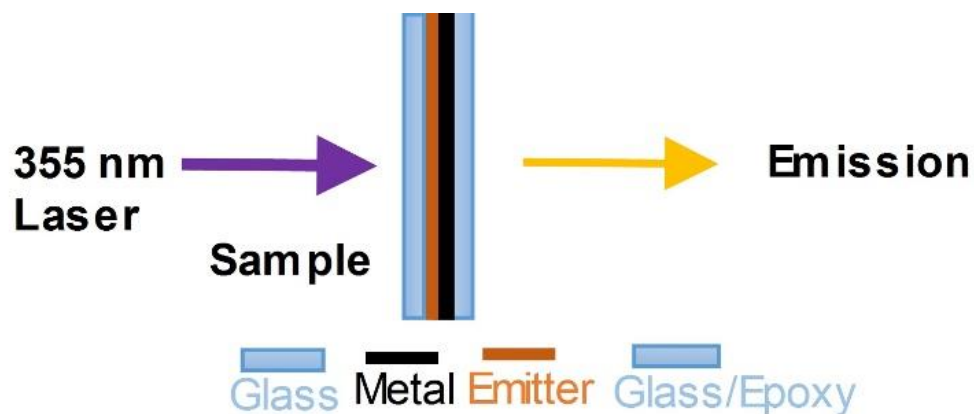


Figure 3.1: Schematic of the sample configuration used for the PL stability measurements.

Transient PL lifetime measurements were then completed in collaboration with Zeqing Shen at Brookhaven National Laboratory to determine the mechanism behind the stability changes. The PL lifetime decay curves of passivated samples were measured using a FluoTime 200 spectrometer (PicoQuant). A 375 nm laser beam (Spectra-Physics MaiTai BB Ti:Sapphire laser (pulse width < 80 ps) with a frequency doubler) was used as

excitation source. The incident and collection angles were 45° with regards to sample surface. The laser repetition rate was set as 400 kHz. A 410 nm long-pass filter was placed in the optical collection path. The emission at 470 nm was detected by applying a monochromator before the detector (MCP-PMT type, Hamamatsu, 45 ps response time) (Figure 3.2). The decay data were recorded using a TimeHarp 260 NANO (PicoQuant) working in time-correlated single photon counting (TCSPC) mode with 250 ps time resolution. The acquired data were then analyzed in FluoFit software (PicoQuant) to get the PL lifetime decay constants of each sample.

3.4. Results and Discussion

The purpose of this study is to investigate if Ag metasurfaces can modify the stability of

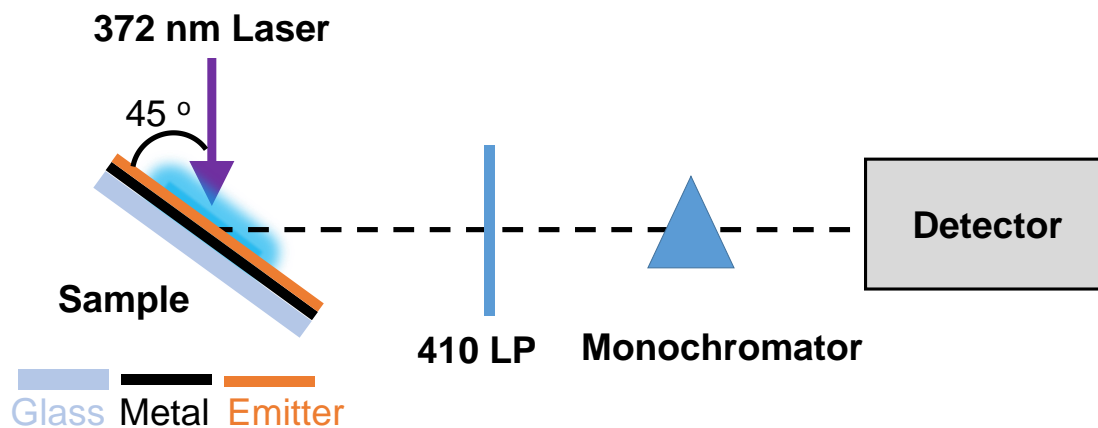


Figure 3.2: Schematic of the experimental configuration used for the transient PL lifetime measurements

blue phosphorescent OLED (Ph-OLED) materials. For this study, we used the host poly(N-vinylcarbazole) (PVK) with the blue phosphorescent dopant bis[2-(4,6-difluorophenyl)pyridinato- C^2,N](picolinato)iridium(III) (FIrpic) which are commonly-

used in Ph-OLEDs [138,142,144]. This host-dopant matrix has been shown to improve light out coupling and enhance triplet excitation because the host assists in charge transport and excitation energy transfer, while the dopant provides color and increases intersystem crossing which improves the internal quantum efficiency [138,142,144]. The chemical structures of the organic materials used are shown in Figure 3.3a. A blend solution containing the host and dopant was spin coated onto five different Ag metasurfaces: planar silver, nanoimprinted silver gratings (1.6 μm pitch 1D grating and 0.7 μm pitch 1D grating), nanoporous (NPO) silver, and nanoparticle (NPT) silver (Figure 3.3b.-e.); see Methods.

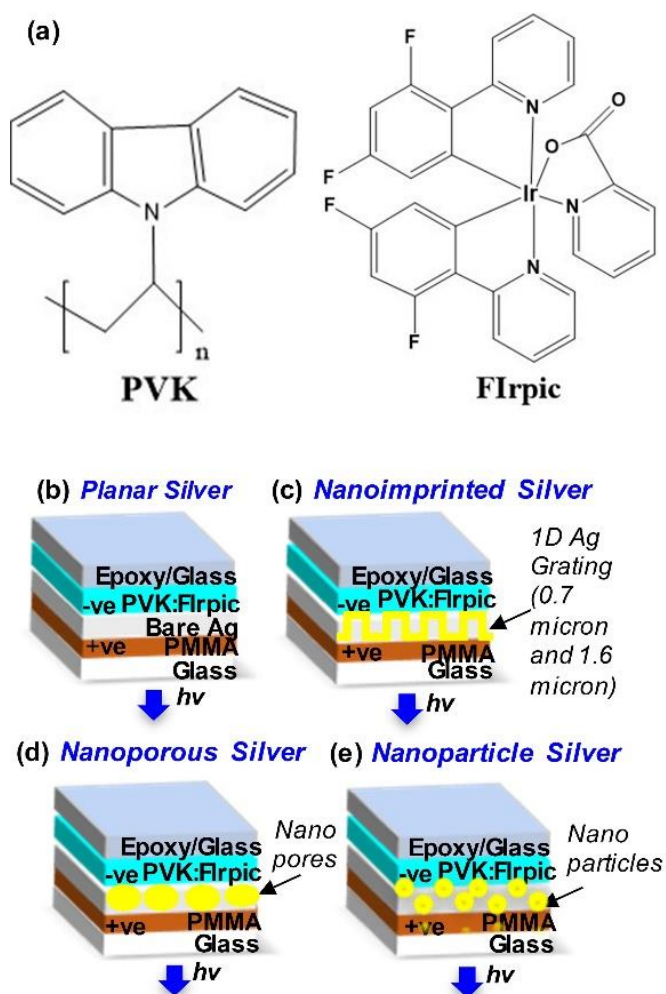


Figure 3.3: (a) The chemical structures of the poly(N-vinylcarbazole) (PVK) and bis[2-(4,6-difluorophenyl)pyridinato-C²,N](picolinato)iridium(III) (FIrpic) molecules. (b-e) Schematic cross sectional diagrams of PVK:FIrpic host:dopant thin-films on five different (meta)surface types: (b) planar silver, (c) nanoimprinted 1D silver gratings (both 1.6 μm grating pitch and 0.7 μm grating pitch); (d) nanoporous (NPO) silver, and (e) nanoparticle (NPT) silver.

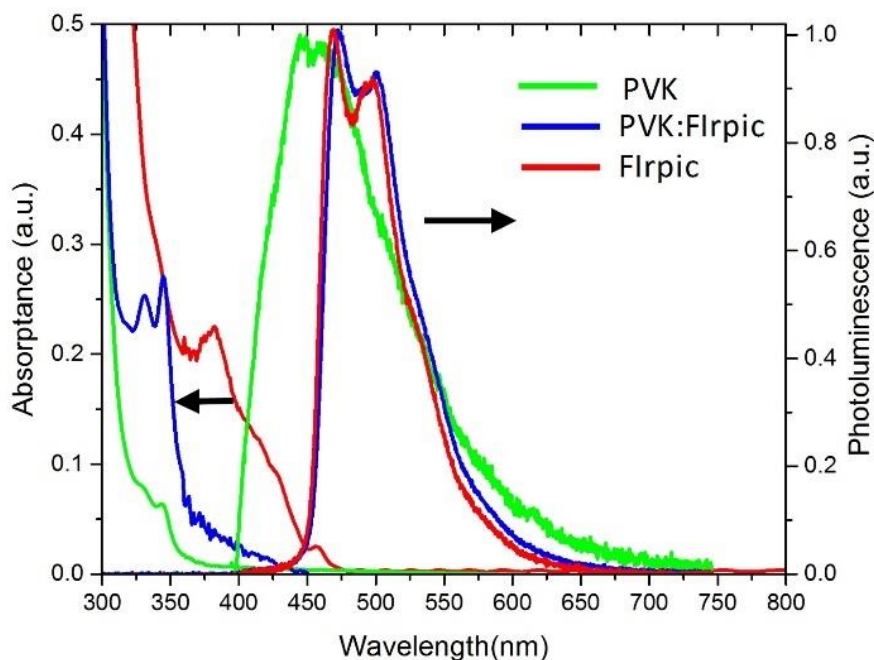


Figure 3.4: The absorption and intensity normalized photoluminescence spectra of thin film host PVK, the dopant FIrpic, and the blend PVK:FIrpic.

The characteristic absorption and normalized PL spectra for thin films of neat PVK, FIrpic and the PVK:FIrpic blend on glass are shown in Figure 3.4; see Methods. The photoluminescence spectrum of PVK:FIrpic follows the characteristic FIrpic spectrum exhibiting two peaks at 472 nm and 500 nm, thus signifying proper energy transfer from the host, PVK, to the dopant, FIrpic. The peak absorption intensity of PVK is at

approximately 350 nm, which is slightly shifted from, the expected PVK peak at a wavelength of 342 nm [139]. However, there is spectral overlap of the absorption spectrum of the dopant, Flrpic, and the photoluminescence spectrum of the host, PVK, in the wavelength range between 400 nm to 470 nm, which accounts for efficient energy transfer.

After investigating the spectral properties of each organic thin film, the metasurface substrates were characterized using scanning electron microscopy (SEM), dark-field (DF) optical microscopy, and UV-visible transmission spectroscopy (Figure 3.5).

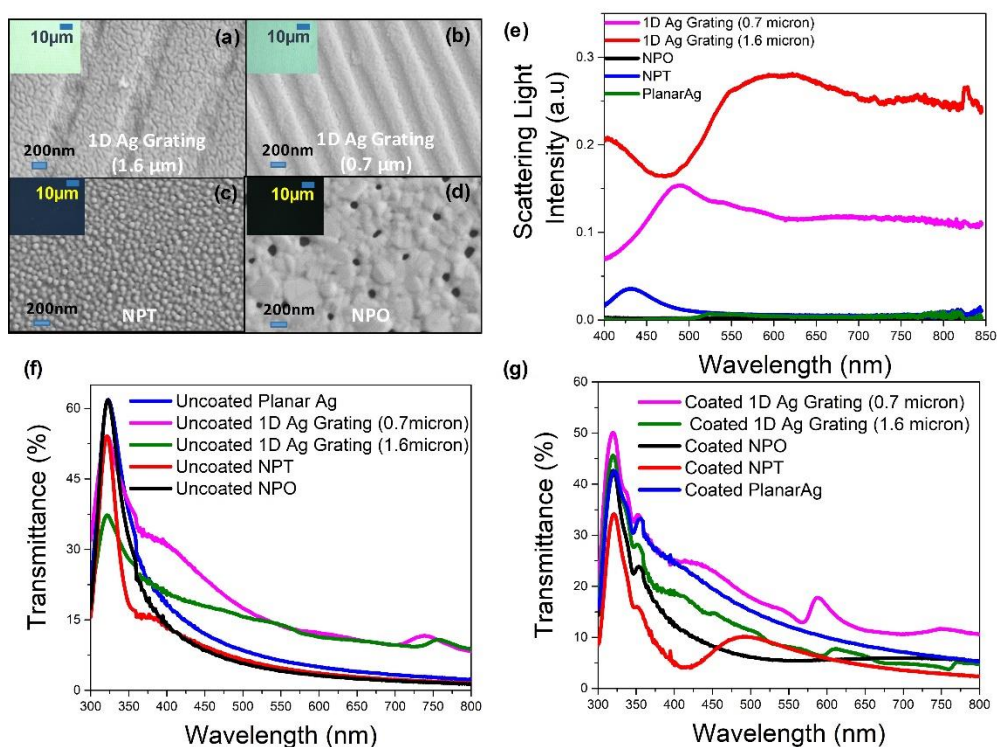


Figure 3.5: SEM images of Ag metasurfaces: (a) the 1.6- μm -pitch 1D Ag grating, (b) the 0.7- μm -pitch 1D Ag grating, (c) Ag nanoparticles (NPT), and (d) nanoporous Ag (NPO). Insets in (a-d) are reflected-light, DF optical images. (e) DF spectra of the Ag metasurfaces. (f, g) Transmission spectra of (f) bare Ag metasurfaces and (g) PVK:Flrpic-coated Ag metasurfaces.

The 1.6 μm and 0.7 μm 1D Ag gratings, NPT Ag, and NPO Ag metasurfaces were all chosen due to their potential to increase light emission of PVK:Flrpic through resonant

light scattering or through local electric-field enhancement at the emission wavelength. The SEM images of the metasurfaces show uniform pattern transfer for the 1D Ag gratings with the 1.6 μm gratings larger in size than 0.7 μm gratings. Both 1D Ag gratings have granular Ag films. The NPT Ag metasurfaces have dense (~ 10 particles per μm^2), quasi-hemispherically-shaped nanoparticles on their surface with a diameter ranging between 10 nm and 100 nm. The NPO Ag metasurfaces had sparse (~ 1 pores per μm^2), irregularly-shaped pores, approximately 50 nm to 200 nm in size, and the Ag regions between the pores had a polycrystalline appearance with Ag grains ~ 200 nm in size. The reflected-light, DF optical images at 100x magnification show that NPT Ag are significantly scattering the light with a high brightness. In contrast, NPO exhibits almost no scattering and 1.6 and 0.7 μm 1-D Ag gratings show intermediate scattering intensity (Figure 3.5a-d, insets). These observations are further corroborated by the DF intensity spectra (Figure 3.5e). The DF spectra of the various Ag metasurfaces show a characteristic localized surface plasmon resonance peak for silver in the 400 nm to 500 nm wavelength range, as well as additional peaks that result from higher order localized surface plasmon modes or out-coupled surface plasmon polaritons supported by the nanostructured metal (Figure 3.5e). Using the DF spectra we expect good spectral overlap of the Ag metasurface scattering with the blue phosphorescent PVK:Flrpic films, which is necessary for effective optical coupling. In the case of the 0.7 μm and 1.6 μm 1-D Ag gratings there are additional peaks at ~ 425 nm, 725 nm, 475 nm, and 625 nm, respectively (Figure 3.5e). The DF spectrum of NPT Ag had a distinct peak at 430 nm, indicative of the localized surface plasmon resonance of individual, spherical nanoparticles, and no significant scattering at longer wavelengths. Weak scattering occurred from NPO Ag at 750 nm, but overall this metasurface did not exhibit

significant scattering. The transmittance spectra of the uncoated Ag metasurfaces show peaks from 300 nm to 350 nm due to bulk plasma frequency of Ag for all metasurfaces. The uncoated 1D Ag grating 0.7 μm and NPT transmittance spectra has a slight shoulder at 350 nm to 400nm with an additional long wavelength peak at 750nm for the gratings. The transmittance is approximately 60% for the uncoated planar Ag, 1D Ag grating 0.7 μm , and NPO, while the transmittance is slightly less for the NPT and approximately a half as transmissive as the 1D Ag gratings 1.6 μm . Further, as expected, the transmittance of the PVK:Flrpic-coated Ag metasurfaces decreased in comparison to the bare metasurfaces, with a shoulder and peak emerging around 350 nm and 370 nm respectively (Figure 3.5f-g). Further, there are additional peaks around 500 nm and 750 nm in the 1D Ag grating spectra which are attributed to surface plasmon polariton modes excited by the gratings.

The initial investigation of the polymer blend and metasurface substrates suggested that the 1.6 μm and 0.7 μm 1-D Ag gratings or NPT Ag would provide the greatest enhancement due to the spectral overlap of scattering with the emission from the PVK:Flrpic blend. However, stability testing was completed for PVK:Flrpic thin films on the following substrates: glass, planar Ag, 1.6 μm and 0.7 μm 1-D Ag gratings patterns, NPT Ag and NPO Ag in order to confirm the initial hypothesis. In addition, the stability of PVK and Flrpic thin films on glass substrates was also monitored. The PL stability results from Sample Set 2 Trial 3 show that the emission from PVK:Flrpic on the NPT Ag and on the 0.7 μm 1-D Ag gratings was more stable relative to that on the planar Ag film, with an increased half-life, L_{50} , (i.e., time to reach 50% of the initial PL intensity) of 5.5 minutes

and 3.7 minutes compared to 3.6 minutes, respectively (Figure 3.6 a-b).

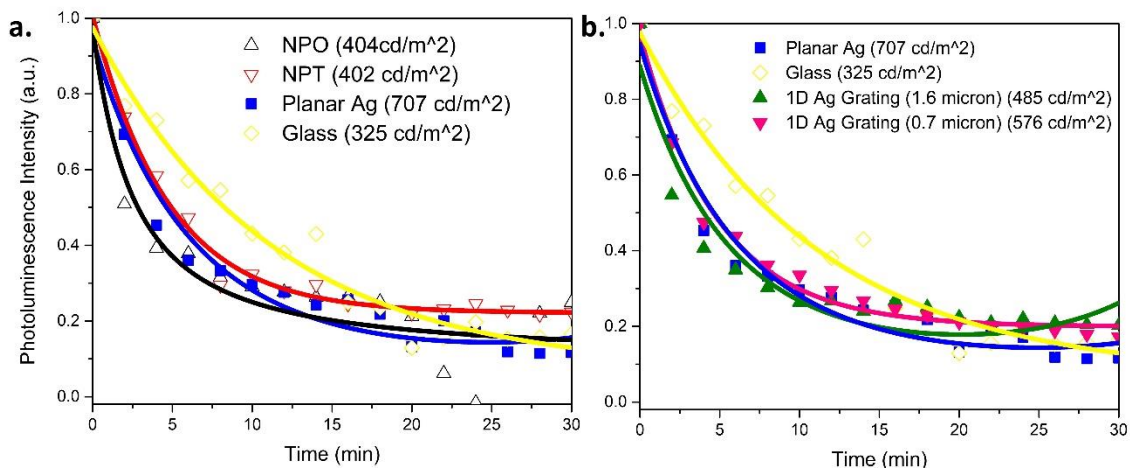


Figure 3.6: PL stability (a,b) curves of PVK:Flrpic thin films on various substrates. For the PL stability measurements, all samples were continuously exposed to a 355-nm laser. For the stability testing (a,b), 1.6 μm 1-D Ag grating, 0.7 μm 1-D Ag grating were all on a PMMA/glass substrate with silver thin films. The planar silver, 1.6 μm grating, and 0.7 μm grating all had 50 nm thick silver films, while the NPO and NPT were fabricated by dewetting from 50 nm thick silver films. All samples were spin coated with 20 g/L of PVK:Flrpic yielding a film thickness of ~ 100 nm. The values in the parenthesis represent the luminance at the power meter (calculated using Equation 3.2) for each sample measurement; thus, the luminance at the sample is one order of magnitude larger.

These L_{50} changes represent enhancements in stability by factors of 1.51 and 1.02 for NPT and 1-D Ag 0.7 μm , respectively. Although these metasurfaces resulted in stability enhancements relative to planar Ag, the stability was reduced by a factor of 2 relative to PVK:Flrpic on glass. The reduced stability on metal substrates compared to glass stems from the increased excitation power in the PVK:Flrpic on metal samples due to reflection of excitation light back into the PVK:Flrpic thin film that was not absorbed on the first

pass through PVK:FIrpic. It should be noted that within optoelectronic devices, PVK:FIrpic thin films will be in the presence of metallic electrode surfaces thus the stability comparison with PVK:FIrpic on planar Ag rather than on glass is more appropriate. When making comparisons across sample sets and trails, we see that for Sample Set 1 Trial 1 the 1.6 μm 1-D Ag gratings and NPT Ag result in the most stable PVK:FIrpic emission, with stability enhancements of 4.4 and 4.3 respectively. For Sample Set 2 Trial 1, NPO is the most stable with a stability enhancement of 1.1. Thus, across all stability measurements PVK:FIrpic-coated NPT Ag is the most stable metasurfaces for S1T1 and S2T3.

Substrate Type	L_{50} (min.)		
	S1T1*	S2T1 ⁺	S2T3*
Glass	9.48	-	2.42
Planar Ag	1	1	1
1-D Ag Grating (1.6 μm)	4.43	0.58	0.72
1-D Ag Grating (0.7 μm)	1.30	0.42	1.02
NPT Ag	4.26	0.23	1.51
NPO Ag	1.30	1.09	0.58

Table 3.1: The stability enhancements (i.e., enhancements in the half-life (L_{50})) of PVK:FIrpic thin films on various substrate types. Data is reported for measurements carried out on different sets of samples (i.e., “Sets”) and on different days (“Trials”) to check the repeatability of the data, as follows: Sample Set 1 Trial 1 (S1T1), Sample Set 2 Trial 1 (S2T1) and Sample Set 2 Trial 3 (S2T3). The various substrate types are glass, planar Ag, 1.6 μm 1-D Ag grating and 0.7 μm 1-D Ag grating patterned metasurfaces, and NPT and NPO nanostructured metasurfaces. Two different luminances were employed for the stability measurements: 10,000 cd/m^2 (indicated by (*)) and 1,000 cd/m^2 (indicated by (+)) which were determined from the measured excitation power densities. All

metallic substrate types (except “Glass”) had an underlying glass coverslip as the substrate.

Transient PL lifetime testing for PVK:Flrpic on each Ag metasurface type was used to determine if enhanced PL stability correlates with enhanced PL lifetime. Overall, PVK:Flrpic thin films on metallic surfaces shortens the average PL lifetime, τ_{avg} , by a factor of 2.8 compared to on glass (Table 3.2). The long average PL lifetime decay constant ($\tau_{avg} = 0.96 \mu\text{s}$) of PVK:Flrpic when on glass can be attributed primarily to the natural phosphorescence lifetime decay of the dopant Flrpic [R]. The results show in all cases that there are fast and slow lifetime decay time constants which contribute to the overall shape of the decay curves (Figure 3.7a-b) (i.e., PL lifetime decay curves were best fit with double or triple exponential decay functions); see Table 3.2.

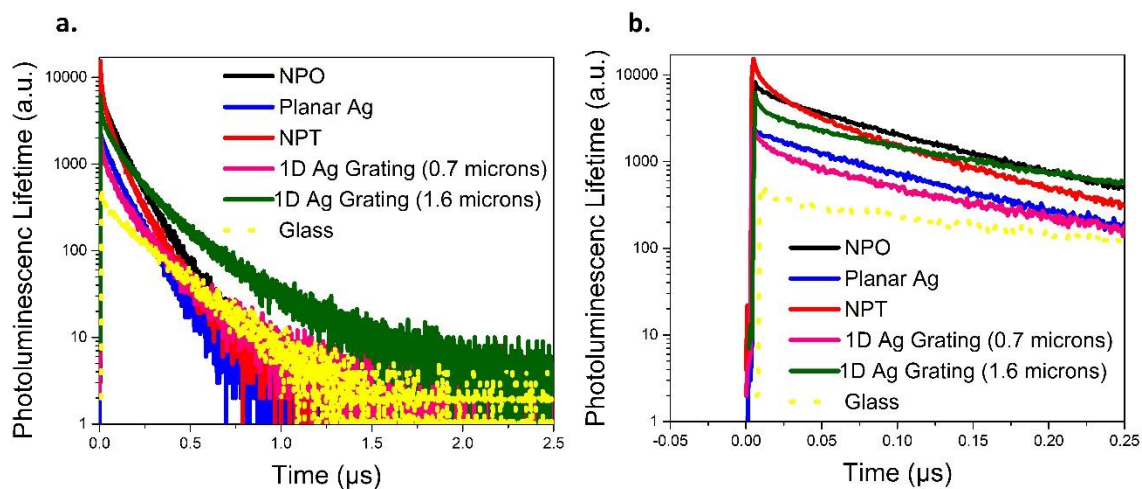


Figure 3.7: PL lifetime (a) curves of PVK:Flrpic thin films on various substrates and (b) the zoomed in time $t=0$ intensity peak. A 372-nm laser was employed for the PL lifetime measurements. The 1.6 μm 1-D Ag grating, 0.7 μm 1-D Ag grating were all on a PMMA/glass substrate with silver thin films. The planar silver, 1.6 μm grating, and 0.7 μm grating all had 50 nm thick silver films, while the NPO and NPT were fabricated by dewetting from 50 nm thick silver

films. All samples were spin coated with 20 g/L of PVK:FIrpic yielding a film thickness of ~100 nm.

The PL lifetime of PVK:FIrpic on planar Ag have two components with time constants of 0.3 μs and ~0.6 μs (Table 3.2). There is a new fast initial exponential decay on 0.7 μm and 1.6 μm 1-D Ag gratings ($\tau_1 \approx 0.07 \mu\text{s}$) and an even faster initial decay on NPT metasurfaces ($\tau_1 \approx 0.04 \mu\text{s}$), not observed on planar Ag, which contribute significantly to the average PL lifetime (30% - 43%). This fast component is also observed on NPO but it has a less significant contribution to the average lifetime (21 %). The second slower lifetime component on NPT ($\tau_2 \approx 0.2 \mu\text{s}$), NPO ($\tau_2 \approx 0.3 \mu\text{s}$), 0.7 μm ($\tau_2 \approx 0.4 \mu\text{s}$) and 1.6 μm 1-D Ag gratings ($\tau_2 \approx 0.5 \mu\text{s}$) are approximately the same time scale as the initial PVK:FIrpic on planar Ag time constant ($\tau_1 \approx 0.3 \mu\text{s}$), accounting for 40-60% of the average PL lifetime. However, while the longest component for the PVK:FIrpic on NPT and NPO ($\tau_3 \approx 0.6 \mu\text{s}$) is the same as the second PVK:FIrpic on planar Ag time constant ($\tau_2 \approx 0.6 \mu\text{s}$), the time constant for the PVK:FIrpic on 0.7 μm and 1.6 μm 1-D Ag gratings ($\tau_3 \approx 1 \mu\text{s}$) is much longer, possibly due to emitter-metal non-radiative interactions. As a result, the average PL lifetime is shortened for the PVK:FIrpic on NPT ($\tau_{avg} \approx 0.3 \mu\text{s}$) and approximately the same for the PVK:FIrpic on NPO ($\tau_{avg} \approx 0.4 \mu\text{s}$), while it is lengthened for PVK:FIrpic on 0.7 μm ($\tau_{avg} \approx 0.6 \mu\text{s}$) and 1.6 μm ($\tau_{avg} \approx 0.8 \mu\text{s}$) 1-D Ag gratings, respectively relative to planar Ag ($\tau_{avg} \approx 0.4 \mu\text{s}$).

Substrate	τ_{average} (microsec)	Intensity at peak intensity	τ_1 (microsec)	τ_2 (microsec)	τ_3 (microsec)	χ^2
Glass						

	0.9630	477	0.1717 (24.71%)	1.0073 (75.29%)		0.931
Planar Ag (2 nd order)	0.43620	2333	0.29867 (73.53%)	0.62014 (26.47%)		0.981
Planar Ag (3 rd order)	0.44553	2333	0.1512 (24.11%)	0.41827 (73.14%)	1.0858 (2.74%)	0.871
1-D Ag Grating (1.6 μm)	0.79503	6186	0.0670 (31.87%)	0.46180 (53.81%)	1.3167 (14.32%)	1.014
1-D Ag Grating (0.7 μm)	0.63587	2608	0.07214 (40.10%)	0.41241 (49.32%)	1.1455 (10.58%)	1.019
NPT Ag	0.34089	15319	0.03933 (43.13%)	0.21612 (42.16%)	0.54607 (14.71%)	0.957
NPO Ag	0.42423	8222	0.05305 (21.26%)	0.31489 (59.08%)	0.62410 (19.66%)	1.038

Table 3.2: The average PL lifetime (τ_{average}), intensity at time, $t = 0$, shortest PL lifetime decay component (τ_1), longer PL lifetime decay component (τ_2), and the longest PL lifetime decay component (τ_3) for PVK:Flrpic thin films on glass, planar Ag, 1.6 μm 1-D Ag grating and 0.7 μm 1-D Ag grating patterned, NPT and NPO nanostructured Ag metasurfaces. The PL lifetime components were extracted from fits to the data using a second or third order exponential decay function. Planar Ag and 1D Ag gratings had an underlying glass coverslip or PMMA/glass coverslip as the substrate.

In the transient PL lifetime data, at peak intensity, there is an increased PL intensity compared to PVK:Flrpic on planar Ag for PVK:Flrpic on all Ag metasurface cases on NPO; 8,222 counts on NPT, 15,319 counts on 0.7 μm 1-D Ag grating, and 2,608 counts on 1.6 μm 1-D Ag grating relative to 6,186 counts μs for PVK:Flrpic on planar Ag. The PL intensity enhancement can be a measure of quantum efficiency enhancement, E_{PL} , assuming all radiated PL is collected by the measurement optics. The E_{PL} relative to planar Ag is 6.6 on NPT, 3.5 on NPO, 1.1 on 0.7 μm 1-D Ag grating, 2.7 on 1.6 μm 1-D Ag grating. Further, quantum yield (QY) spectra were obtained for Sample Set 1 with the sample excitation wavelength and sample configuration as for the PL stability

measurements. The QY values trend with E_{PL} in that the QY on planar Ag increases relative to glass (~ 22 % to 31 %, respectively). In addition, QY increases for 1-D Ag Grating (0.7 μ m), but decreases for NPO Ag relative to planar Ag (~ 48 % and ~25 %, respectively).

In summary, the PVK:Flrpic on NPT is the most stable relative to the PVK:Flrpic on planar Ag, with the most intense and rapid PL lifetime, as well as most enhancement quantum efficiency (Figure 3.6a-b and 3.7a-b). Therefore, in the case of the PVK:Flrpic on NPT metasurface there is a correlation between enhanced stability and shortened PL lifetime at 0.46 μ s relative to 0.88 μ s for the PVK:Flrpic on planar Ag (Table 3.3).

Substrate Type	L_{50} (min.)			τ_{PL} (sec.)			E_{PL}	QY (%)
	S1T1*	S2T1 ⁺	S2T3*	S1T1	S2T1	S2	S1	
Glass	9.48	-	2.42	0.09	0.96	0.20	22.4 \pm 8.6	
Planar Ag	1	1	1	0.48	0.44	1	31.2 \pm 7.6	
1-D Ag Grating (1.6 μ m)	4.43	0.58	0.72	0.46	0.80	2.65	-	
1-D Ag Grating (0.7 μ m)	1.30	0.42	1.02	0.62	0.64	1.12	48 \pm 6.6	
NPT Ag	4.26	0.23	1.51	0.66	0.34	6.57	-	
NPO Ag	1.30	1.09	0.58	0.47	0.42	3.52	24.6 \pm 6.5	

Table 3.3: The stability enhancement (i.e., enhancement in the half-life (L_{50})), average PL lifetime (τ_{avg}), and PL intensity enhancement (E_{PL}) of PVK:Flrpic on various substrate types. Data is reported for measurements carried out on different sets of samples (i.e., “Sets”) and on different days (“Trials”) to check the repeatability of the data, as follows: Sample Set 1 Trial 1 (S1T1), Sample Set 2 Trial 1 (S2T1) and Sample Set 2 Trial 3 (S2T3). The various substrate types are glass, planar Ag, 1.6 μ m 1-D Ag grating and 0.7 μ m 1-D Ag grating patterned metasurfaces, and NPT and NPO nanostructured metasurfaces. Two different luminances were employed for the stability measurements: 10,000 cd/m² (indicated by (*)) and 1,000 cd/m² (indicated by (+)) which were determined from the measured excitation power densities. The PL quantum yield (QY) for Sample

Set 1 for PVK:FIrpic thin films on glass, planar Ag, 1.6 μm 1-D Ag grating and 0.7 μm 1-D Ag grating patterned, NPT and NPO nanostructured Ag metasurfaces PL lifetime and QY measurements were carried out in collaboration with Zeqing Shen and Kun Zhu. Planar Ag and 1D Ag gratings had an underlying glass coverslip or PMMA/glass coverslip as the substrate.

3.5. Conclusions

The aim of this study is to experimentally investigate the use of silver plasmonic metasurface films to increase the radiative decay rate of triplet emission from blue organic phosphorescent films, and, hence, to minimize triplet quenching processes that cause unstable emission. Here, we alter the amount of ready available optical states that emission can couple to through the use of Ag metasurfaces. In summary, we demonstrate an improvement in the stability of photoluminescence emission from blue organic phosphorescent OLED material on certain nanostructured silver metasurfaces compared to those on planar silver. A well-known conjugated polymer:organometallic complex combination, PVK:FIrpic, was employed as the blue phosphorescent thin film which was spin coated on various Ag metasurfaces. The various metasurface types that were studied include: 1D Ag gratings with 1.6 μm pitch and 0.7 μm pitch fabricated using nanoimprint lithography; and nanoporous (NPO) and nanoparticle (NPT) silver thin films fabricated using thermally-assisted dewetting. These Ag plasmonic metasurfaces were chosen due to their potential ability to increase light emission through light scattering and the possibility of intense localized electric near fields arising from localized surface plasmon resonances and surface plasmon polariton modes. The PVK:FIrpic-coated metasurfaces were characterized using photoluminescence (PL) stability, PL lifetime, and PL quantum yield measurements and compared to corresponding data for PVK:FIrpic on planar silver films

to investigate the relationship between silver plasmonic metasurfaces and improved phosphorescence stability. The PVK:FIrpic thin films on NPT Ag were the most promising with an average photoluminescence stability enhancement factor of 2, a reduction in the average photoluminescent lifetime by a factor of 1.25, and an average photoluminescent enhancement factor of 9 relative to PVK:FIrpic on planar Ag. Overall, the results have shown a correlation between enhanced PL stability and PL lifetime of PVK:FIrpic on silver plasmonic metasurfaces relative to a planar silver surfaces. This study demonstrates that plasmonic metasurfaces are promising electrode for use in future phosphorescent OLED devices that required stable blue phosphorescence emission.

Chapter 4.

Theoretical Predictions of Light-Extraction Efficiency of Planar OLED Device Architectures

4.1. Abstract

In Chapter 3 of this thesis, a stability study was completed for Ph-OLEDs in order to address the issues with operational lifetime experienced by blue-emitting OLEDs. In addition to addressing stability issues, improvements in blue OLED efficiency are also necessary to improve the cost, energy efficiency and sustainability metrics discussed in Chapter 2. Despite high internal quantum efficiencies, blue-emitting, thin-film organic light-emitting diodes suffer from low overall efficiencies due to low light-extraction efficiencies. This is primarily caused by a large portion of the active-layer emission being trapped inside photonic and plasmonic waveguide modes arising from total internal reflections and electromagnetic energy trapped between the layers of the device. As a result, only ~20% of the internally-produced light is emitted to air following electrical excitation. Therefore, it would be advantageous to improve optical properties of the device by altering the device architecture or the addition of light management layers and/or structures to increase light out-coupling efficiency. Fabricating and testing such devices and structures can be time consuming and costly; therefore, optical modelling, such as electromagnetic simulations are important to predict limitations and investigate the effectiveness new device designs for improving light extraction efficiency.

Theoretical electromagnetic simulation approaches, such as finite-element and finite-difference-time-domain (FDTD) methods, have been widely-used to optimize OLEDs composed of submicron thick layers [180-186]. However, a comparison of the

theoretical light-extraction efficiency has not been carried out for the various categories of OLED device architectures. In this Chapter, light extraction efficiency (LEE) electromagnetic simulations are carried out for the four OLED device architectures (bottom-emitting conventional, top-emitting conventional, bottom-emitting inverted, and top-emitting inverted), which have been proposed to address the efficiency and stability drawbacks, as discussed in Chapter 2. The LEE of these OLED device architectures are carried out using FDTD simulations that solve Maxwell's Equations across multiple device layers and that use an electric dipole source placed in the active layer to mimic an emitting molecule. In addition to LEE, we assess which layer of each device architecture impact LEE the most. In the case of phosphorescent emitters the theoretical internal quantum efficiency is 100 %; thus, the electric dipole emitter is assumed to be 100 % efficient.

We show that LEE is strongly dependent on electric dipole orientation, with an electric dipole oriented in the plane of the device (x or y dipole orientation) having the highest contribution to the total light extraction efficiency LEE_{total} in all device configurations. Further, the bottom-emitting conventional device has the highest LEE_{total} of 28 % and the top-emitting conventional has the lowest LEE_{total} of 1 %. To determine in which layers optical power loss occurs, power absorption, P_{abs} , simulations were completed. For the bottom-emitting device structures, the metallic layers account for the most power dissipated with $P_{abs,x} = 5\%$ and $P_{abs,z} = 14\%$ for conventional and $P_{abs,x} = 19\%$ and $P_{abs,z} = 74\%$ for inverted. The silver layer in the bottom-emitting inverted configuration accounts for more of the P_{abs} than the aluminum layer in the bottom-emitting conventional configuration despite the being approximately 4 times thinner. While for the top-emitting device structure Ag accounts for the most power absorption with $P_{abs,x} = 19\%$

- 22% and $P_{abs,z} = 38\% - 41\%$. A comparison between bottom-emitting and top-emitting device configurations P_{abs} show that $P_{abs,x}$ is a factor of 2 greater in the emissive layer for the top-emitting configurations, thus accounting for the decreased P_{abs} in the top-emitting configurations. These results coincide with the negligible LEE in the z dipole oriented direction for bottom-emitting device structure and minimal LEE in the x dipole oriented for top-emitting device structure.

Further, the averaged power absorption per layer in the emissive layer is ~6% for all devices and the metallic layers range from 10% for aluminium up to 46% for silver. Thus, most of the loss can be attributed to optical coupling between the active layer and the metal in the form of SPP modes. Thus, it would be advantageous to utilize surfaces or structures embedded in the metallic anode or cathode layers to minimize power absorption.

4.2 Introduction

Organic light-emitting diodes (OLEDs) have recently been explored as luminaire and display sources due to their ability for wide viewing angles and the possibility of being made thin, transparent, and flexible. However, in comparison to inorganic LEDs they typically have a lower brightness. The decreased brightness is, in part, due to a large portion of the emission being trapped inside photonic and plasmonic waveguide modes arising from total internal reflections and electromagnetic energy trapped between the layers of the device. As a result, only ~20% of the internally-produced light following electrical excitation is emitted to air. Therefore, it would be advantageous to design an optical device with light management layers and/or structures to increase light out-coupling efficiency. Fabricating such structures can be time consuming and costly; therefore, optical modelling

such as electromagnetic simulations to predict limitations, and theoretical solutions has been widely-used to optimize OLEDs composed of submicron thick layers [180]. For example, electromagnetic simulations of the light-extraction efficiencies of OLEDs have been completed by Shi *et al.* using the finite difference time domain (FDTD) method [181]. In their study, broadband emission for a green top-emitting phosphorescent OLED (TOLED) was calculated and compared to a bottom-emitting OLED (BOLED). They obtained an optimal TOLED device configuration by varying the thickness and, hence, optical cavity length of the device (i.e. recombination zone) and by varying the location of the active layer within the simulation. They observed that the TOLED had a more concentrated spectral radiance energy than the BOLED and a higher light out-coupling efficiency (51% for the TOLED as compared to 21% for the BOLED). Rostami *et al* utilized FDTD simulations to model a multilayer OLED structure that optimized light extraction efficiency by minimizing quenched emission due to total internal reflections at the ITO/glass interface. Using various design principles, they found that the optimal device structure incorporated 9 alternating layers of TiO_2 and SiO_2 with 2.15 μm layer thickness between the indium tin oxide (ITO) layer and the glass substrate. This new device design showed a 40% light extraction efficiency improvement relative to an OLED device structure without the 9 alternating layers [182].

In addition, interference effects can modify the light extraction efficiency (LEE) and the emission spectrum of polymer-based devices comprised of device layers with differing refractive indices and thicknesses on the order of the optical wavelength of emission. To model interference effects of polymer-based OLED devices it should be noted that due to the preferential polymer chain alignment and material optical properties, the

device emission is anisotropic [182,184]. Work by McBranch *et al.* has completed polarized optical transmission and reflection measurements for PPV derivatives. They found that polymer chains of spin-cast thin films of the a electroluminescent polymer lie primarily in the plane of the film; thus, electroluminescence is preferentially emitted in a direction perpendicular to the plane of the polymer film with the relevant dielectric and electrical transport properties being in the perpendicular direction as well [184,185]. S. M. King *et al* concluded similar findings for polyfluorene derivatives and that fluorescent emission of the polymer is polarized along the polymer backbone; however, the phosphorescence emission of the polymer is dominated by a component perpendicular to the chain suggesting that the T_1 triplet excited state is oriented perpendicular to the backbone of the polymer, most likely out of the plane of the molecule [184,186].

In OLEDs, electroluminescence emission arises from radiative recombination of an excited electronic dipole, where the emissive dipole transition has a particular orientation with respect to the OLED device layer stack. In this study, emission is modelled classically as an arbitrarily oriented electric dipole emitter with contributions in the parallel (“||”) and perpendicular (“ \perp ”) directions with respect to the plane of the device (i.e., x (||), y (||), and z (\perp) orientations) in order to account for the isotropic emission [184]. It should be noted that dipole emitters oriented perpendicularly emit their radiation into the plane of the device rather than perpendicular to the plane of the device [184]. Further, different interface conditions effect the dipole emitter differently when oriented in x, y, and z directions. Thus, the x and z dipole should be weighted in proportion to their contribution to the overall electroluminescent emission for an accurate electroluminescence calculation. M. Flammich completed a quantitative *in situ* analysis via optical characterization and

determined that for a polymeric emitter material (i.e., anisotropic emitter) in an OLED device that 93.5% parallel and 6.5% perpendicular dipole moments contribute to the radiation pattern corresponding to a Gaussian dipole emitter distribution [184]. However, for an isotropic emitter there are 66.7% parallel and 33.3% perpendicular dipole moments. Therefore, one can see how the dipole orientation in spontaneous emission is dependent on the molecular morphology of the material, which has a major impact on OLED device efficiency and performance. While FDTD electromagnetic simulations can be used to calculate light-extraction efficiency, a large portion of the light generated inside an OLED will be trapped within optical channels due to interband electronic absorption, photonic waveguide modes (WGM) in the active layer, interlayers and substrate, and surface plasmon polaritons (SPP) modes supported by metal electrode layers. Theoretically, approximately 50% of optical loss is expected to be due to WGM and SPP modes (Figure 4.1) [187]. Therefore, in this work, in addition to light-extraction simulations, absorption simulations were carried out to identify the optical loss channels within each layer of a given device configuration. The motivation for the work reported in this Chapter is to theoretically optimize and predict the light-extraction efficiency for four different polymer-based (P-OLED) configurations: conventional bottom- and top-emitting P-OLEDs and inverted bottom- and top-emitting P-OLEDs. To evaluate and optimize the light-extraction efficiencies theoretical finite-difference time domain (FDTD) electromagnetic simulations were carried out with attention paid to absorption within each device material layer and dipole emitter orientation.

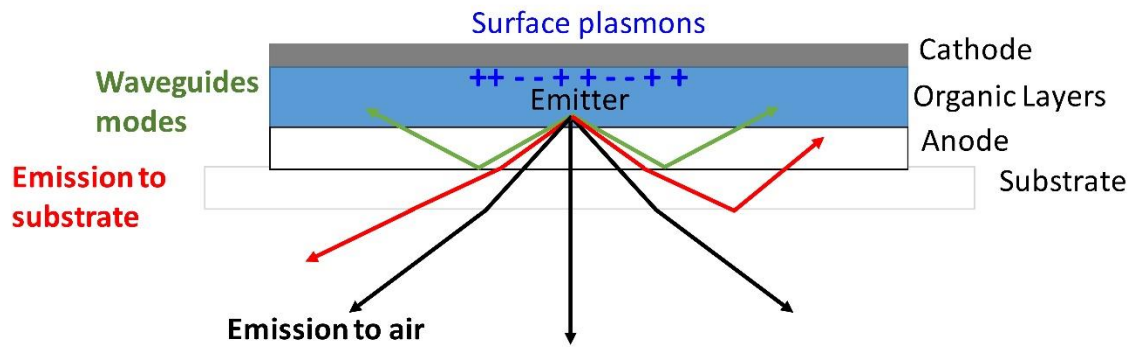


Figure 4.1: Schematic of the optical loss channels within a conventional OLED device architecture [Reproduced from Ref. 187].

4.3 Methods

The FDTD electromagnetic method employed here was a 3D Maxwell solver that captures the (sub-) wavelength-scale electromagnetic fields within materials and the impacts on optical device efficiency by using material input parameters such as wavelength-dependent dielectric constants and material thicknesses, as well as source properties and simulation boundary conditions [188]. OLED device efficiency is usually determined from two quantities: (1) light-extraction efficiency, LEE , which is the percentage of photons generated within the OLED that emit into air; and (2) internal quantum efficiency (n_{IQE}), which is the percentage of photons generated per injected electron and hole. The external quantum efficiency (n_{EQE}) of an OLED device is then defined as $n_{EQE} = LEE * n_{IQE}$ [187]. Here, we assume $n_{IQE} = 100\%$ and focus on accessing LEE for the different device architectures.

Light created by spontaneous emission from molecules within the active layer (i.e., photons) can be treated classically as an electric dipole point source, which is an oscillating

dipole field that has a specific orientation, phase, frequency, and polarization. The optical constants of the active layer used here were taken from those of polyfluorene (PFO) which is a typical organic polymer semiconductor material with a dispersive dielectric constant and which behaves as an incoherent emitting source of photons. Incoherent emission of photons results in random and frequent phase changes, thus making it difficult to control when an excited molecule will lose energy in the form of radiation. Therefore, an average emitted electromagnetic field intensity, $|\hat{E}|^2$ for incoherent isotropic dipole emitters, in an organic emissive layer can be calculated by:

$$\langle |\hat{E}|^2 \rangle = \frac{|p_o|^2}{3} \{|E_x|^2 + |E_y|^2 + |E_z|^2\} \quad [4.1]$$

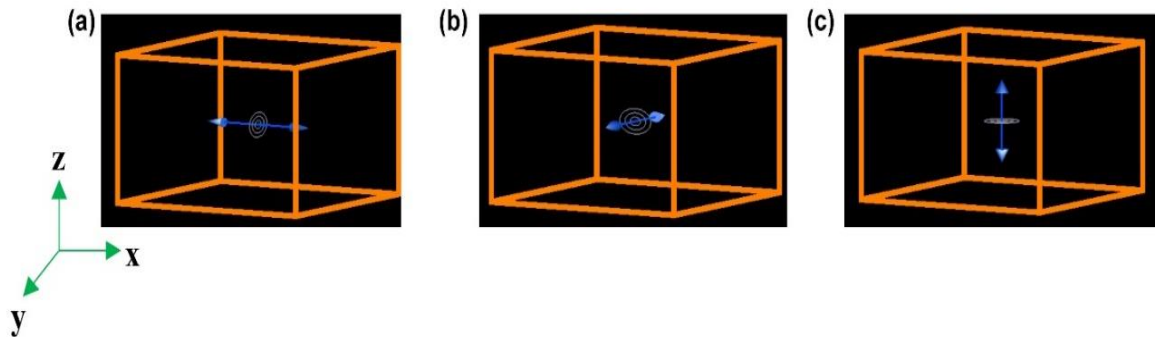


Figure 4.2: A dipole (blue arrow) suspended in free space oriented in either the (a) x , (b) y , and (c) z axes directions, respectively. The gray concentric circles correspond to the direction of propagation of the electric field away from the center of the dipole. The average emitted electromagnetic field is calculated by the magnitude of the electric field in the E_x , E_y , and E_z directions [187].

where E_x , E_y , and E_z are the electromagnetic field amplitudes generated by a single electric dipole source (i.e., molecular transition dipole) along the x , y and z axes and $|p_o|^2$ is the dipole moment (Figure 4,2). Since FDTD is a coherent simulation method,

three separate simulations were run with an electric dipole source oriented along the x , y , and z axes and average the resulting electric field intensities $|E_x|^2$, $|E_y|^2$, and $|E_z|^2$. However, due to the use of metal boundaries above the cathode within the simulation and a perfectly matched (PML) boundary in the x -, y -, and z - directions in the simulations, E_z is the independent variable with E_x and E_y being equal [189]. The materials employed in the simulated devices were as follows: ITO, PEDOT:PSS, PFO, LiF and Al with layer thicknesses of 108 nm, 57 nm, 108 nm, 2.3 nm and 151 nm for the conventional bottom-emitting device structure; ZnO, PFO, MoO₃, Ag with layer thickness of 36.5 nm, 108 nm, 11 nm, and 35 nm for the inverted bottom-emitting device structure; Ag, PEDOT:PSS, PFO, LiF, Ag with layer thickness of 125 nm, 57 nm, 108 nm, 2.3 nm, and 17.8 nm for the top-emitting conventional device structure; and Ag, ZnO, PFO, MoO₃, Ag with layer thickness of 17.8 nm, 36.5 nm, 108 nm, 11 nm, and 125 nm for the top-emitting inverted device structure all on 100-nm-thick glass substrate with a 50 nm thick capping layer of PDMS. All layer thicknesses were set to match those described in Chapter 2 except for the TiO₂ which was been replaced with zinc oxide, ZnO, in all inverted device simulations with a thickness of 36.5 nm. The thickness value were obtained from a literature review of layer thicknesses for the various OLED device architectures.

The optical constants for Al, ITO, LiF, MoO₃, and PEDOT:PSS were obtained from a dielectric constant library compiled by Burkhardt *et al* [190]; the optical constants of ZnO were obtained from spectroscopic ellipsometry measurements by Postava *et al* [191]; the optical constants of Ag are provided by Lumerical FDTD Solutions and were obtained from the CRC Handbook [187]; and the optical constants of PFO were calculated at the 440 nm wavelength employed for the electric dipole sources from work by Campoy-Quiles

et al [192]. A two-dimensional time-domain monitor (light-extraction monitor; see Figure 4.3) was placed above or below each architecture, depending on the direction of light emittance, to capture the transmittance fraction of electric dipole emission out of the device. A $15 \text{ nm} \times 15 \text{ nm} \times 15 \text{ nm}$ dipole transmission box (consisting of a set of six 2D transmission monitors) was also placed around the electric dipole to obtain the transmittance of the electric dipole within the active area; this represents the total electric field intensity emitted by the electric dipole (i.e., the dipole power). We observed that defining the appropriate mesh size was critical to obtaining accurate results. We defined the dipole mesh size of $3 \text{ nm} \times 3 \text{ nm} \times 3 \text{ nm}$ and in the x , y and z directions, respectively.

We used the aforementioned example from the literature by Shi *et al* to obtain a verified methodology by which to use FDTD simulations to calculate light-extraction for the OLED device architectures under study in this work; however, the setup differed slightly due to non-negligible imaginary part of the refractive index (k value) in the dispersive active layer [180].

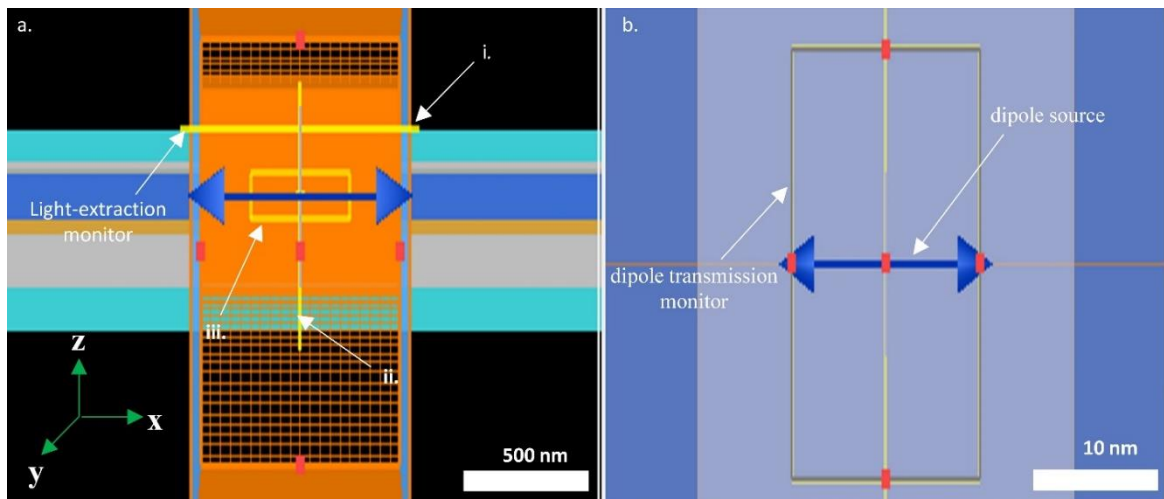


Figure 4.3: (a) Top-emitting inverted OLED cross-sectional image with dipole emitter located within the active layer and three power monitors quantify and visualize light emitted out of the

device (i) the electric field in the x -direction (ii), and the electric field in the z -direction (iii). (b) The dipole transmission monitor ($15 \text{ nm} \times 15 \text{ nm} \times 15 \text{ nm}$) encases only the dipole source within the active layer.

As shown in Figure 4.3 we can see an image in the x - z plane of a top-emitting inverted OLED structure with a dipole emitter embedded within the active layer. The layer thicknesses that were used are the same as those described above. There are three monitors located within the simulations: a light-extraction monitor (i) above the device to capture the light emitted from the device as well as power monitors in the x (ii.) and z (iii.) directions used to capture cross-sectional images of the electric field profiles; and a dipole transmission monitor (b) encasing the dipole in order to capture the light emitted from the dipole within the active layer. The transmittance from the light-extraction monitor located above the OLED is divided by the transmittance from the dipole transmission box located around the dipole to calculate the light-extraction efficiency (Table 4.1).

As discussed previously, light-extraction efficiency is defined as the fraction of useful power emitted above or below the OLED over the total optical power emitted in the active layer of the OLED; assuming light-extraction with 100% electrical internal quantum efficiency for a unpolarized dipole source with isotropic emission we then take:

$$n^{100\%elec}_{extraction} = \frac{\text{useful power}}{\text{total dipole power}} = \frac{1}{3} \left(\frac{P_z}{\text{dipole power}} + \frac{2P_x}{\text{dipole power}} \right) \quad [4.1]$$

where P_z is the transmitted power through the light-extraction monitor (Figure 4.5a) when the dipole is oriented in the z -direction and $2P_x$ is the transmitted power through the light-extraction monitor when the dipole is oriented in the x -direction making sure to account for the dipole oriented in the y direction using the factor of 2, and total dipole power is the transmitted power into the simulation by a dipole source through the $15 \text{ nm} \times 15 \text{ nm} \times 15$

nm size (in x , y , z direction, respectively) dipole transmission box monitor (Figure 4.5b).

Since the materials in OLED devices exhibit inherent losses due to parasitic absorption (i.e., non-negligible imaginary part of the refractive index), electric field intensity profiles are useful to observe how light is dissipated throughout the device (Figure 4.4).

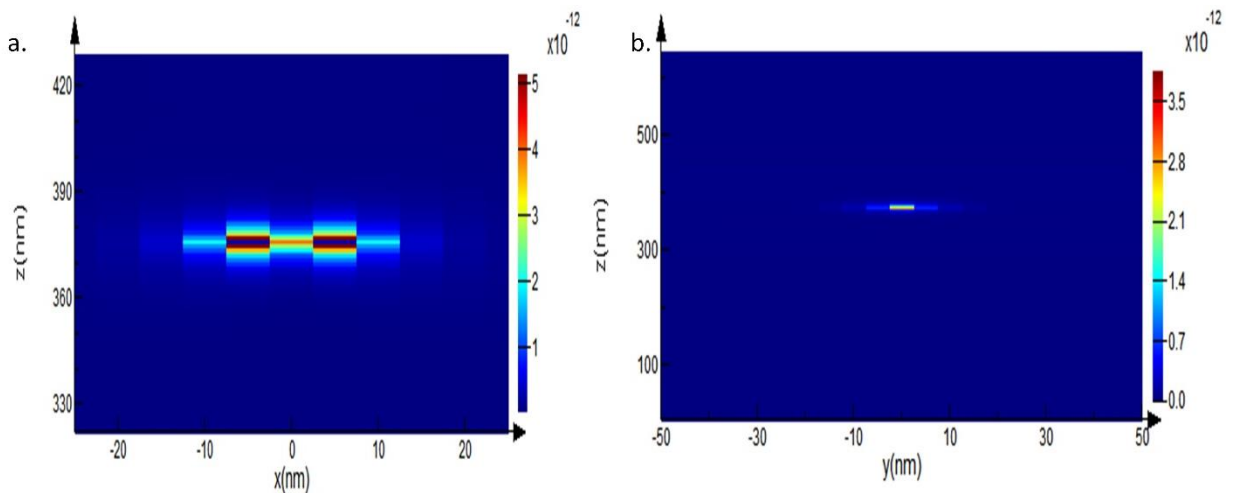


Figure 4.4: The electric field intensity profiles for electric dipoles within a PFO layer, polarized in the (a) x -direction and (b) z -direction.

As can be seen within the electric field intensity profiles the electric field intensity is greatest closest to the dipole in both the x and z directions thus showing that a large amount of loss occurs even prior to light reaching the glass substrate. As a result, a brief study on the effects of dipole orientation on the LEE was completed. Further, FDTD simulations were completed that analyse the power absorption per layer in order to observe the optical loss channels within the various OLED device structures under study. The simulation setup was similar to Figure 4.3 with additional power absorbed and transmission boxes placed around each material layer (Figure 4.5).

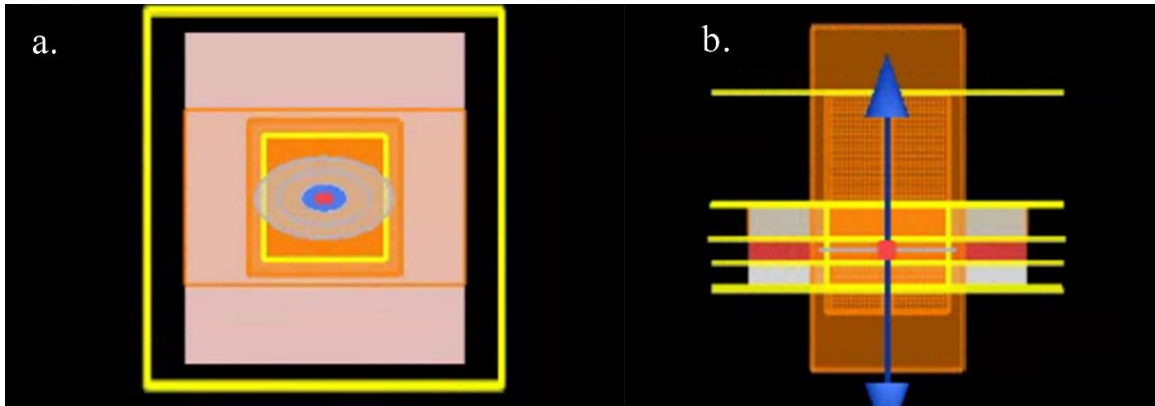


Figure 4.5: (a) Bottom-emitting conventional OLED cross-sectional image with dipole emitter located within the active layer. (b) Bottom-emitting conventional OLED with three power monitors oriented around each device layer and the entire device structure, light extraction monitors oriented above the device structure, and dipole transmission monitor in the x-z plane.

4.4. Results and Discussion

4.4.1. LEE Results for Different Device Architectures

The LEE was calculated using both the real and complex dielectric constants for all materials within the device structure. As observed when only the real dielectric constant is used, the bottom-emitting and top-emitting conventional architectures have LEE values that are comparable to the literature [181]. For the bottom-emitting device configuration the LEE ranged from 51% to 68% and for the top-emitting conventional configuration the LEE was 51%. The LEE of the top-emitting configuration agreed with the results of the Shi *et al*; however, the LEE of the bottom-emitting configuration was greater than that reported by Shi *et al* (BOLED LEE of 21% and TOLED LEE of 51%) (Table 4.1) [181]. Although, the top-emitting inverted LEE was only 4%. However, when complex dielectric constants were used the LEE results are negligible, with all device configurations exhibiting LEE values significantly less than 1% (Table 4.1). Clearly, including a non-

negligible imaginary part of the refractive index in all of the device layers causes unrealistically large absorption of the source light.

	Device Layers	Device Thickness (nm)	Refractive Index $\tilde{n} = n + ik$	LEE $\tilde{n} = n$ (except metal)	LEE $\tilde{n} = n + ik$
Shi <i>et al.</i> [181]	Glass	-	1.51	TOLED:	-
	Al	150		51%	
	MoO ₃	3	1.77	BOLED:	
	HTL	40	1.77	21%	
	EML	15	1.77		
	ETL	55	1.77		
	Liq	1	1.77		
	Al	1			
	Ag	22			
	CL	80	2.2		
Bottom-Emitting Conventional	Glass	100	1.45	68%	0.7%
	ITO	108	1.92 + 0.001i		
	PEDOT:PSS	57	1.55 + 0.011i		
	PFO	108	1.81 + 0.034i		
	LiF	2.3	1.28 + 0.175i		
	Al	151	0.598 + 5.38i		
	PDMS	50	1.4		
Bottom-Emitting Inverted	Glass	100	1.45	51%	0.8%
	ZnO	36.5	2.08 + 0.002i		
	PFO	108	1.81 + 0.034i		
	MoO ₃	11	2.39 + 0.003i		
	Ag	35	0.598 + 5.38i		
	PDMS	50	1.4		
Top-Emitting Inverted	Glass	100	1.45	4%	3.37*10 ⁻¹⁹ %
	Ag	125			
	ZnO	36.5	2.08 + 0.002i		
	PFO	108	1.81 + 0.034i		
	MoO ₃	11	2.39 + 0.003i		
	Ag	17.8			
	PDMS	50	1.4		
Top-Emitting Conventional	Glass	100	1.45	51%	3.35*10 ⁻³² %
	Ag	125	Ag		
	PEDOT:PSS	57	1.55 + 0.011i		
	PFO	108	1.81 + 0.034i		
	LiF	2.3	1.28 + 0.176i		
	Ag	17.8			
	PDMS	50	1.4		

Table 4.1: Device layers, layer thicknesses and refractive indices used in the theoretical FDTD simulation of LEE for the four different OLED device architectures. The LEE results using real and complex refractive indices for the four device configurations (bottom-emitting conventional and inverted, and top-emitting conventional and inverted) are reported in the two right-most columns. In the top row, the simulation parameters and LEE results from Shi *et al.* for bottom-emitting and top-emitting conventional device configurations are reported for comparison.

4.4.2. Effect of Dipole Orientation on LEE Results for Different Device Architectures

To examine the mechanisms behind the reported LEE values for each device configuration, dipole orientation dependent simulations were completed. For this analysis, all simulations were completed using the real refractive index for all materials except metals. Additionally, the effect of dipole orientation on LEE is assessed for planar OLED architectures without charge transport layers. The use of basic OLED device architectures results in a decrease in LEE_{total} for all P-OLED device configurations except the top-emitting inverted, which is expected due to charge injection difficulty into wide band gap PFO (Table 4.1 and 4.2). As shown in Table 4.2, the bottom-emitting configurations have the highest LEE_{total} . Further, the x -oriented dipole contributes to the LEE_{total} more than the z -oriented dipole, with the bottom-emitting conventional device having the highest LEE_{total} of 28 %, and the top-emitting conventional device having with the lowest LEE_{total} of 1 % (Table 4.2). These results are consistent with the expected radiation direct of each dipole and with previously-discussed theoretical predictions by M. Flammich *et al* [184]: emission is more effectively radiated out of the device structure (i.e., in the direction perpendicular to the plane of the device) when the dipole is x -oriented; and emission is efficiently coupled into photonic waveguide modes in the plane of the device when the

dipole is z-oriented.

Device Configuration	Device Layers	LEE_x	LEE_z	LEE_{total}
Bottom-Emitting Conventional	ITO (108 nm)	42.38%	0.48%	28.41%
	PFO (108 nm)			
	Al (151 nm)			
Bottom-Emitting Inverted	ZnO (36.5 nm)	29.93%	1.15%	20.44%
	PFO (108 nm)			
	Ag (35 nm)			
Top-Emitting Conventional	Ag (125 nm)	1.07%	1.46%	1.18%
	PFO (108 nm)			
	Ag (17.8 nm)			
Top-Emitting Inverted	Ag (17.8 nm)	12.19%	0.89%	8.43%
	PFO (108 nm)			
	Ag (125 nm)			

Table 4.2: Dipole-orientation-dependent LEE and LEE_{total} for the four OLED device configurations: bottom-emitting conventional and inverted and top-emitting conventional and inverted. Device layers and thicknesses are also shown.

4.4.3. Power Absorption Per Layer for Different Device Architectures

To identify the power absorption, P_{abs} , that occurs in each device structure it was necessary to identify in which layers the emission attenuates. All simulations were completed in the same manner as in Section 4.4.2. To determine in which layers optical power loss occurs P_{abs} simulations were completed. For the bottom-emitting device structures, the metallic layers account for the most power dissipated with $P_{abs,x} = 5\%$ and

$P_{abs,z} = 14\%$ for conventional and $P_{abs,x} = 19\%$ and $P_{abs,z} = 74\%$ for inverted. The silver layer in the bottom-emitting inverted configuration accounts for more of the P_{abs} than the aluminum layer in the bottom-emitting conventional configuration despite the being approximately 4 times thinner. While for the top-emitting device structure Ag accounts for the most power absorption with $P_{abs,x} = 19\% - 22\%$ and $P_{abs,z} = 38\% - 41\%$. Comparison between bottom-emitting and top-emitting devices showed that P_{abs} in PFO is twice as much in the z dipole orientation compared to the x dipole orientation. This accounts for the decreased LEE_{total} in the top-emitting device configurations. The power absorbed results are consistent with the negligible LEE_z for the z dipole orientation direction for bottom-emitting device structure and the minimal LEE_x for the x dipole orientation direction for top-emitting device structure.

Device Configuration	Configuration Dipole Orientation	Electric Dipole Power Dissipated, P_{abs} , Per Layer			
		Refractive Index $\tilde{n} = n$ (except for metal) x dipole	Refractive Index $\tilde{n} = n$ (except for metal) z dipole	Refractive Index $\tilde{n} = n$ (except for metal) Averaged	
Bottom-Emitting	ITO (108 nm)	0 %	0 %	0%	
	Conventional	PFO (108 nm)	2.41 %	8.74 %	5.58%
	Al (151 nm)	5.07 %	14.30 %	9.69%	
Bottom-Emitting	ZnO (36.5 nm)	0 %	0 %	0%	
	Inverted	PFO (108 nm)	2.31 %	8.48 %	5.40%
	Ag (35 nm)	19.06 %	73.55 %	46.305	
Top-Emitting	Ag (125 nm)	19.06 %	38.86 %	28.96%	

Conventional	PFO (108 nm)	4.33 %	8.22 %	6.28%
	Ag (17.5 nm)	21.81 %	39.71 %	30.76%
Top-Emitting	Ag (17.5 nm)	18.82 %	37.71 %	28.27%
Inverted	PFO (108 nm)	4.33 %	8.22 %	6.28%
	Ag (125 nm)	22.44 %	41.14 %	43.14%

Table 4.3: The simulated power absorption per layer for dipoles oriented in the x and z directions for four device configurations: bottom-emitting conventional and inverted, and top-emitting conventional and inverted.

Further, the averaged absorption, $P_{abs,averaged}$ in PFO is ~6% for all devices with power dissipated in the metallic layers ranging from 10% for aluminium up to 46% for silver. Thus, most of the loss can be attributed to optical coupling between the active layer and the SPP modes of the metal, as mentioned in Section 4.2. Thus, it would be advantageous to utilize surfaces or structures embedded in the metallic anode or cathode layers to minimize power absorption by outcoupling SPPs. It should be noted that the emissive zone was in the center of the PFO emitter material due to the location of the dipole source position. However, differences in electron and hole mobility in the p-type organic semiconductor emissive layer would move the emissive zone closer to the cathode at the emissive layer/cathode interface in real devices. As a result, the power absorption would increase at the emissive layer/cathode interface and the overall P_{abs} would be expected to decrease for all configurations except for the bottom-emitting inverted configuration due to negligible absorption in the ZnO layer.

4.5 Conclusions and Future Directions

The aim of the work reported in this Chapter was to theoretically predict and understand the light-extraction efficiency of four different OLED device configurations: conventional bottom- and top-emitting OLEDs and inverted bottom- and top-emitting OLEDs. To evaluate the light-extraction efficiencies, theoretical finite-difference-time-domain electromagnetic simulations were carried out with attention paid to absorption within each device material layer and dipole emitter orientation. We found that LEE_{total} is the highest for the bottom-emitting device configurations (LEE_{total} of 28 %) and is the lowest for the top-emitting conventional device (LEE_{total} of 1 %). Further, the x -oriented dipole contributes to the LEE_{total} more than the z -oriented dipole, which coincides with experimental observations that have found that due to centrifugal forces during spin coating, polymer chains align flat in the plane of an OLED device with emission primarily radiating perpendicularly out of the device. It should be noted that LEE_{total} was calculated with LEE_x and LEE_z equally weighted contributions. If accounting for the preferential in-plane dipole emitter orientation in a real device, LEE_x and LEE_z would change according to the percentages discussed in Section 4.2 for anisotropic radiation patterns. Thus, LEE_{total} would increase for each device configurations as follows: 53% (bottom-emitting conventional), 50% (bottom-emitting inverted), 24% (top-emitting conventional), and 27% (top-emitting inverted). Therefore, it would be advantageous to enhance the emission in the z -direction to increase the overall LEE using plasmonic surfaces or structures. In addition, power absorption, P_{abs} , simulations have shown that a large portion of the power absorption in the devices occurs in the metallic layers, particularly when the dipole is oriented in the z direction, with $P_{abs,x} = 5$ % and $P_{abs,z} = 14$ % for the bottom-emitting conventional device, and $P_{abs,x} = 19$ % and $P_{abs,z} = 74$ % for the bottom-emitting inverted

device. While for the top-emitting conventional device, $P_{abs,x} = 19\% - 22\%$ and for the top-emitting inverted device, $P_{abs,z} = 38\% - 41\%$ due to emission coupling to SPP modes between the metal/dielectric interface. Comparison between bottom-emitting and top-emitting devices showed that P_{abs} in PFO is twice as much in the z dipole orientation compared to the x dipole orientation. This accounts for the decreased LEE_{total} in the top-emitting device configurations. The power absorbed results are consistent with the negligible LEE_z for the z dipole orientation direction for the bottom-emitting device structure and the minimal LEE_x for the x dipole orientation direction for the top-emitting device structure. These theoretical electromagnetic simulations can provide information to experimentalists on the optimal device configuration to fabricate, as well as additional information on which device layers would benefit the most from the implementation of plasmonic structures.

5. Thesis Summary, Conclusions and Future Directions

5.1. Thesis Summary and Conclusions

Proponents for sustainable alternative lighting and display options advocate for organic light-emitting diodes (OLEDs), particularly polymer-based organic light-emitting diodes (P-OLEDs), because of their potential for low-cost fabrication, more versatile device formats and lower power consumption compared to traditional options. In Chapter 2 of this thesis, an economic, energy and CO₂ emissions assessment was carried out for four different laboratory-scale, blue-emitting P-OLED device architectures: bottom-emitting conventional; bottom-emitting inverted; top-emitting conventional; and top-emitting inverted. Additionally, comparisons with a standard, commercial-scale, blue inorganic light-emitting diode (LED) device architecture are made. The various P-OLED device architectures were investigated due to their potential to increase operational lifetime (inverted) and light out-coupling efficiency (top-emitting). The following metrics are used in this assessment: device cost, yearly operating cost, optical power cost, CO₂ emissions from device production, and yearly operating CO₂ emissions. We show that the top-emitting inverted device architecture significantly reduces the device cost, yearly operating cost, optical power cost and CO₂ emissions for the P-OLED devices, due to elimination of indium tin oxide and its comparatively high luminous efficacy and longer lifetime. In addition, the top-emitting inverted P-OLED device architecture performs competitively at the laboratory scale with commercial-scale inorganic LEDs for all metrics. However, if top-emitting P-OLEDs are to be manufactured on a large scale, the luminous efficacy assumed for laboratory-scale devices needs to remain constant throughout development to remain competitive.

As discussed in Chapter 2 conclusions, during scale-up efficiency and lifetime gains are necessary for laboratory/pilot- scale fluorescent P-OLEDs to be a viable option. Thus, it would be imperative for one to complete a stability assessment to determine fabrication methods for a more long-lasting fluorescent P-OLEDs. A compounding factor is the issue of inefficiency, which is initially enhanced through the use of phosphorescent emitters. While Ph-OLEDs can have an internal quantum efficiency of 100%, on metal electrodes the light-extraction efficiency is 5-30% primarily due to coupling to surface plasmon polariton (SPP) modes and photonic waveguide modes, with SPPs, accounting for up to 50% of the loss in light-extraction efficiency. In addition to low light-extraction efficiency, efficiency “roll-off” in Ph-OLEDs is a significant cause of device degradation at high luminance and is attributed primarily to triplet-polaron and triplet-triplet quenching processes. One way to address the efficiency “roll-off” issue is to accelerate the radiative decay rate of phosphorescence to reduce triplet quenching processes. Further, efficiency “roll-off” in blue Ph-OLEDs is very pronounced due to high triplet energies and significant triplet-polaron and triplet-triplet quenching relative to red and green Ph-OLED counterparts.

The aim of this study is to experimentally investigate the use of silver plasmonic metasurface films to increase the radiative decay rate of triplet emission from blue organic phosphorescent films, and, hence, to minimize triplet quenching processes that cause unstable emission. We use the host poly(N-vinylcarbazole) (PVK) with the blue phosphorescent dopant, bis[2-(4,6-difluorophenyl)pyridinato-C2,N](picolato) iridium(III) (FIrpic), which is commonly-used in blue Ph-OLED prototypes. This host-dopant combination has been shown to improve light out coupling and enhance triplet

excitation because the host assists in charge transport and excitation energy transfer, while the dopant provides color and increases intersystem crossing which improves the internal quantum efficiency. PVK:FIrpic thin film samples are spin coated onto planar silver, 1D Ag grating (1.6 μm and 0.7 μm), nanoporous (NPO) silver, and nanoparticle (NPT) silver metasurfaces. Each silver plasmonic metasurface is prepared with 50 nm of silver using nanoimprint lithography deposition for 1D Ag grating (1.6 μm and 0.7 μm) and dewetting deposition for NPO and NPT. In addition PVK, FIrpic, and PVK:FIrpic thin films on glass are used as a reference. The silver plasmonic metasurfaces are chosen due to their ability to increase light emission through light scattering and the possibility of intense localized electric near fields arising from localized surface plasmon resonances. These near-fields are expected to lead to changes in the decay rate of emission from nearby molecules. The samples are characterized using photoluminescence (PL) stability, PL lifetime, and PL quantum yield measurements to investigate the relationship between silver plasmonic metasurfaces and improved phosphorescence stability. Results have shown a correlation between enhanced PL stability and PL lifetime of silver plasmonic metasurfaces relative to a planar silver surface. In addition, PL quantum yield measurements of PVK:FIrpic thin films on silver plasmonic metasurfaces relative to planar silver show that NPT metasurfaces result in the greatest improvement in both the stability and efficiency of PVK:FIrpic thin films.

In Chapter 2, a stability study was completed for Ph-OLED in order to address the lifetime issues experienced by OLEDs. Therefore, emphasis on improving efficiency is necessary to address metrics standards developed for OLED scale-up in Chapter 1. One way to determine efficiency is through the use of light-extraction efficiency (LEE)

simulations. Organic light-emitting diodes have recently been explored as luminaire and display sources due to their ability for wide viewing angles and the possibility of being made thin, transparent, and flexible. However, in comparison to inorganic LEDs they typically have a lower brightness. The decreased brightness is, in part, due to a large portion of the emission being trapped inside photonic and plasmonic waveguide modes arising from total internal reflections and electromagnetic energy trapped between the layers of the device. As a result, only ~20% of the internally-produced light following electrical excitation is emitted to air. In the case of phosphorescent emitters the theoretical internal quantum efficiency is 100 %, thus; LEE would need improvements in fluorescent emitter OLEDs. In Chapter 3 of this thesis, a stability study was completed for Ph-OLEDs in order to address the issues with operational lifetime experienced by blue-emitting OLEDs. In addition to addressing stability issues, improvements in blue OLED efficiency are also necessary to improve the cost, energy efficiency and sustainability metrics discussed in Chapter 2. Despite high internal quantum efficiencies, blue-emitting, thin-film organic light-emitting diodes suffer from low overall efficiencies due to low light-extraction efficiencies. This is primarily caused by a large portion of the active-layer emission being trapped inside photonic and plasmonic waveguide modes arising from total internal reflections and electromagnetic energy trapped between the layers of the device. As a result, only ~20% of the internally-produced light is emitted to air following electrical excitation. Therefore, it would be advantageous to improve optical properties of the device by altering the device architecture or addition of light management layers and/or structures to increase light out-coupling efficiency. Fabricating and testing such devices and structures can be time consuming and costly; therefore, optical modelling, such as

electromagnetic simulations are important to predict limitations and investigate the effectiveness new device designs for improving light extraction efficiency.

Theoretical electromagnetic simulation approaches, such as finite-element and finite-difference-time-domain (FDTD) methods, have been widely-used to optimize OLEDs composed of submicron thick layers [180-186]. However, a comparison of the theoretical light-extraction efficiency (LEE) has not been carried out for the various categories of OLED device architectures. In this Chapter, LEE electromagnetic simulations are carried out for the four OLED device architectures (bottom-emitting conventional, top-emitting conventional, bottom-emitting inverted, and top-emitting inverted), which have been proposed to address the efficiency and stability drawbacks, as discussed in Chapter 2. The LEE of these OLED device architectures are carried out using FDTD simulations that solve Maxwell's Equations across multiple device layers and that use an electric dipole source placed in the active layer to mimic an emitting molecule. In addition to LEE, we assess which layer of each device architecture impact LEE the most. In the case of phosphorescent emitters the theoretical internal quantum efficiency is 100 %; thus, the electric dipole emitter is assumed to be 100 % efficient. We show that LEE is strongly dependent on electric dipole orientation, with an electric dipole oriented in the plane of the device (x or y dipole orientation) having the highest contribution to the total light extraction efficiency LEE_{total} in all device configurations. Further, the bottom-emitting conventional device has the highest LEE_{total} of 28 % and the top-emitting conventional has the lowest LEE_{total} of 1 %. To determine in which layers optical power loss occurs, power absorption, P_{abs} , simulations were completed. For the bottom-emitting device structures, the metallic layers account for the most power dissipated with $P_{abs,x} = 5\%$ and $P_{abs,z} = 14\%$ for

conventional and $P_{abs,x} = 19\%$ and $P_{abs,z} = 74\%$ for inverted. The silver layer in the bottom-emitting inverted configuration accounts for more of the P_{abs} than the aluminum layer in the bottom-emitting conventional configuration despite the being approximately 4 times thinner. While for the top-emitting device structure Ag accounts for the most power absorption with $P_{abs,x} = 19\% - 22\%$ and $P_{abs,z} = 38\% - 41\%$. A comparison between bottom-emitting and top-emitting device configurations P_{abs} show that $P_{abs,x}$ is a factor of 2 greater in the emissive layer for the top-emitting configurations, thus accounting for the decreased P_{abs} in the top-emitting configurations. These results coincide with the negligible LEE in the z dipole oriented direction for bottom-emitting device structure and minimal LEE in the x dipole oriented for top-emitting device structure. Further, the averaged power absorption per layer in the emissive layer is $\sim 6\%$ for all devices and the metallic layers range from 10% for aluminium up to 46% for silver. Thus, most of the loss can be attributed to optical coupling between the active layer and the metal in the form of SPP modes. Thus, it would be advantageous to utilize surfaces or structures embedded in the metallic anode or cathode layers to minimize power absorption.

In conclusion, the work reported in this thesis studies the efficiency and stability gains arising from the implementation of new device architectures and structures using experimental and theoretical methods. The work is original in that it consists of the first quantitative assessment of economic, energy and sustainability impacts of different OLED device architectures. Additionally, the demonstration that the local electromagnetic fields of metasurfaces can be used to improve the stability of phosphorescent OLED materials is unique and is relevant to the implementation of blue phosphorescence emitters in commercial OLEDs. The approaches to improve OLED device performance reported in

this thesis have the potential to save on capital costs and on energy consumption, and to minimize the carbon footprint associated with OLED devices.

5.2. Future Directions

5.2.1. Economic, Efficiency, and Environmental Assessment (Extension)

The economic, efficiency, and environmental assessment was completed for different P-OLEDs, however; assumptions had to be made which limited the scope of results. The assumptions in regard to the economic and environmental impacts should be addressed to expand the current knowledge on this area. The assumption was made that the manufacturing cost would be a percentage of the materials cost. A further exploration into the cost of manufacturing P-OLEDs at the pilot-scale and then data could be extrapolated for scale-up. This methodology would provide a more accurate approximation of the upfront cost to the consumer. Further, each economic metric was calculated for the use of electricity and it would be interesting to see if there are regional differences. Therefore, assessments can be completed for the south, west, and midwest regions, as well as the entire United States. This can provide additional information on whether the P-OLED device can be a viable device for other areas besides New Jersey. As new data is released from the DOE in subsequent years on fossil fuel consumption for the United States the environmental CO₂ contribution of each device configuration should be updated. As the United States move to more renewable resources its dependence on fossil fuels will decrease, thus; improving the carbon footprint for all devices.

5.2.2. Characterization of the Operational Device Lifetime

The development metrics of increased stability for P-OLEDs in Chapter 1 for commercialization purposes prompts a further study into methods to remedy this issue. The device stability of a P-OLEDs is dependent on the stabilization of charge transport layers and the reduction of oxygen and water vapour ingress into the device. Typically, to achieve stabilization and oxygen and vapour permeation reduction alternative device materials for the HTL and ETL layers have been explored as well as encapsulants and getters to enclose the device and prevent permeation [160, 161]. Thus, next steps would be to complete a comparative P-OLED study, where the effects of alternative encapsulant materials such as Al₂O₃ deposited by atomic layer deposition (ALD) and Parylene C layers deposited by thermal chemical vapour deposition (CVD) on the device operational lifetime are explored. The study of two issues in relation to device lifetime can occur: (1) storage lifetime, the device's ability to maintain performance over a certain storage period; and (2) continuous-use lifetime, the device's ability to maintain performance while operating continuously [161]. The lifetime can be measured by the amount of time it takes for the device to reach L₅₀ of its initial device performance. This would require an additional PL stability study of the NPT metasurfaces to determine if there can be further stability increases by varying NPT size and packing fraction, or use of other metasurface material, as well as EL stability testing, which then can be correlated with transient EL lifetime and EL quantum efficiency data. In addition, X-ray photoelectron spectroscopy (XPS) spectra of the surfaces between the active layer and the charge transport layers by separating the layers of the device after device operation. The XPS emission spectra and signal intensity can be used to identify surface, interface, and impurity levels, thus providing information on charge carrier

layer/active layer interface and active layer surface quality. Improving the quality of these surfaces will enhance the charge-injection efficiency and indirectly improve the lifetime of the device.

5.2.3. Optimization of Active Layer Thickness

As issues of stability are addressed so must issues of inefficiency, as both are imperative for wide spread commercialization. As light-extraction efficiency is one method to study efficiency. It has been shown in Chapter 4 that there is negligible light-extraction efficiency with the complex dielectric constants for each material layer. This can prompt an additional study on optimizing active layer film thickness with and without charge injection layers as the initial study was completed with the real dielectric constant of each material except the metal electrodes. The layer thickness can be determined using thin film interference theory where constructive or destructive interference is determined by the following equations $2d = m \frac{\lambda_{vac}}{n_2}$ or $2d = (m + \frac{1}{2}) \frac{\lambda_{vac}}{n_2}$ where d is the active layer thickness, m is an integer value, and λ_{vac} is the wavelength in a vacuum (440nm) providing information on the optimal device configuration for experimental fabrication.

5.2.4. Theoretical Calculation of External Quantum Efficiency with and without Plasmonic Nanostructures

Once the device layer thicknesses have been optimized optical and electrical losses can be accounted for with the internal quantum efficiency for both the far-field (Method 1) and near-field (Method 2) calculations; see Appendix B.1. The far-field method (Method 1) can provide information on light-extraction efficiency changes due to changes in the

extraction emission profile, while the near-field method (Method 2) can provide additional information on the presence of hotspots (i.e., intense, localized optical near-fields) within the P-OLED devices. Both are essential in characterizing the performance viability of the various P-OLED architectures with and without plasmonic nanostructures. For Methods 1 and 2, FDTD simulations with dipole emitters embedded within the active layer in the presence and absence of plasmonic nanostructures for a finite simulation region and device structure should be carried out. These simulations can be carried out for the different P-OLED architectures comparing planar versus nanostructured geometries (See Appendix B).

5.2.5. Conclusions

Future directions include completing light-extraction and radiative decay rate simulations for various nanostructured OLED geometries incorporating plasmonic metasurfaces, fabricating planar and nanostructured P-OLEDs for EL and PL spectroscopy, and determining new materials to minimize the energy barrier between the active layer and charge transport layers. The device and metasurface designs and studies in this thesis and future work discussed in this chapter are expected to impact the organic light-emitting diode community as well as those generally interested in energy efficiency and sustainable lighting and display technologies.

Appendix A:

Supplemental PL Stability and PL Lifetime Data for Chapter 3.

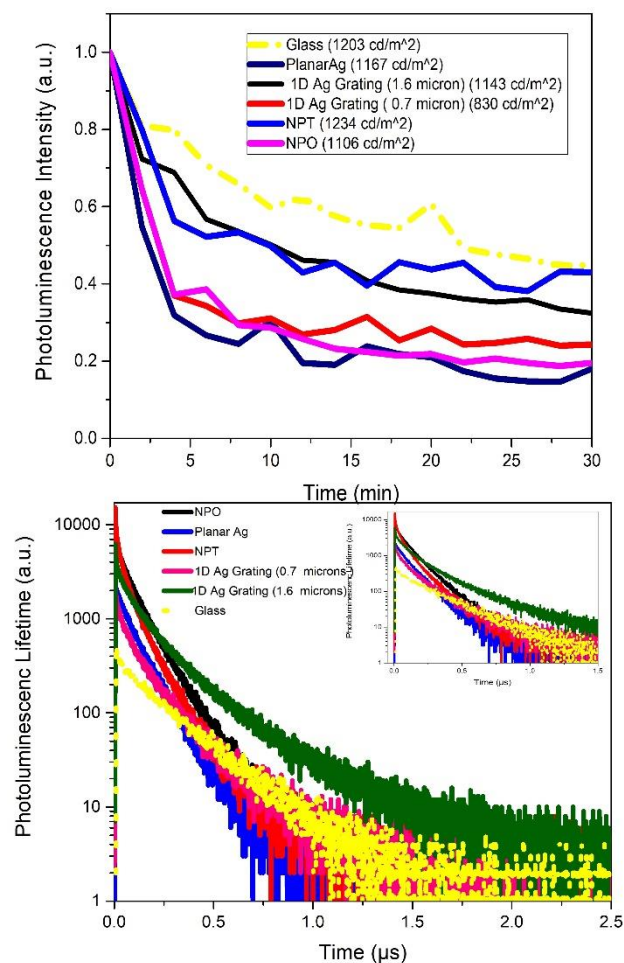


Figure A1: (Top) PL stability of Sample Set 1 (see Chapter 3, Methods). (Bottom) PL lifetime of Sample Set 1. All samples were continuously exposed to the 355-nm laser and 372-nm laser for the photoluminescence stability and lifetime testing, respectively. For the stability testing the 1D Ag Grating (1.6 μm) and 1D Ag Grating (0.7 μm) were on PMMA/glass substrates with 50 nm silver thin films. The NPO and NPT Ag were directly on glass substrates. All samples were spin coated with 20 g/μL of PVK:Firpic.

Appendix B:

Methodology for Simulating Light-Extraction Efficiency of OLEDs that Incorporate Plasmonic Nanostructures

One method to assist in light-out-coupling is through the implementation of plasmonic nanostructures. These simulations are run with the same parameters as Section 4.2. with the additional implementation of plasmonic nanostructures into the P-OLEDs. Plasmonic nanostructures have the potential to enhance the light-extraction efficiency due to their strong light scattering cross-sections, thus, the influence of copper, Cu, gold, Au, and silver, Ag, rods, spheres, nanohole array and nanoparticle arrays and other anisotropic structures (such as rectangles, stars, and hexagons) embedded within the active layer, charge injection layers, and nanostructured electrodes on light-extraction efficiency is studied (Figure B1).

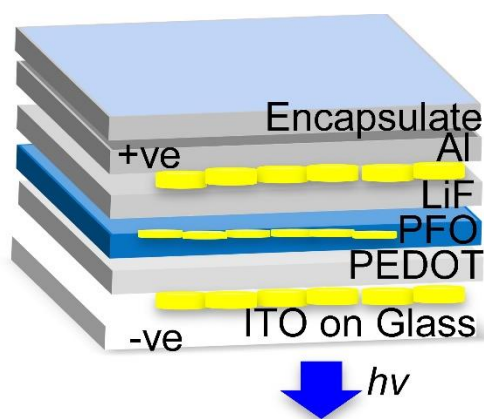


Figure B1: Schematic of a bottom-emitting P-OLED with nanostructures embedded within the active layer, and, in between the anode and HTL, and cathode and ETL layers.

The light-extraction efficiency enhancement factor for the nanostructured cases relative to the planar devices is quantified as follows:

$$n_{\text{extraction factor}} = \frac{n_{\text{extraction nanostructured}}}{n_{\text{extraction}}} \quad [\text{B1}]$$

While the light-extraction efficiency gives us information about the amount of photons emitted into the air the internal quantum efficiency provides information on radiative emission from a source within a medium.

B.1. Internal Quantum Efficiency

Method 1:

The electrical internal quantum efficiency $n_{IQE}^{\text{electrical}}$ is composed of the current injection efficiency $n_{\text{injection}}$ and the optical internal quantum efficiency n_{IQE}^{optical} [195, 196]:

$$n_{IQE}^{\text{electrical}} = n_{\text{injection}} * n_{IQE}^{\text{optical}} \quad [\text{B2}]$$

where $n_{\text{injection}}$ is the fraction of charges that will recombine within the active area (radiatively or non-radiatively) and is defined as:

$$n_{\text{injection}} = \gamma * \chi \quad [\text{B3}]$$

where γ is the charge carrier balance factor, i.e., the probability that an electron-hole pair will recombine and form an exciton and χ is the exciton spin factor which accounts for the exciton spin statistics [195,196] . When the charge mobility is unbalanced, holes and electrons have a high probability of traveling through the device without recombining which leads to a large leakage current and low $n_{IQE}^{\text{electrical}}$. The introduction of charge injection layers remedies this issue by minimizing mean free path of the charges and reducing the energy barriers relative to the active layer and charge transport layers, and in turn, by raising the charge carrier balance factor, γ , to nearly 100% [196]. Some examples

of various ETL and HTL materials are seen in Figure 2.2. The effect on $n^{electrical}_{IQE}$ by implementing various charge injection layers such as metal oxides (NiO_x , Ag_xO , Cu_xO , and MoO_3) within P-OLED devices is explored based on knowledge of, γ , for the various HTL and ETL materials from the literature and comparisons are drawn between the different P-OLED architectures. In the case of fluorescent emitters' exciton spin factor, χ , only singlets are allowed to decay to the ground state. However, under electrical excitation there is typically a 1:3 singlet-to-triplet production ratio for organic semiconductors, thus, allowing only a $\sim 25\%$ exciton spin factor, χ [195, 196]. The optical internal quantum efficiency $n^{optical}_{IQE}$ is the probability that recombination will result in radiative (photon) emission (i.e., singlet excitation). The optical internal quantum efficiency $n^{optical}_{IQE}$ is defined as:

$$n^{optical}_{IQE} = \frac{\text{radiated power by optical excitation}}{\text{total power}} = \frac{\Gamma_{radiated}}{\Gamma_{radiated} + \Gamma_{non\ radiated}} \quad [B4]$$

where $\Gamma_{radiated}$ is the decay rate of photons emitted and $\Gamma_{non\ radiated}$ is the decay rate of photons not emitted due to absorption and intrinsic material loss. For Method 1 it is assumed $n^{optical}_{IQE} = \text{PLQY}$, where PLQY is the intrinsic photoluminescence quantum yield of the material (45 - 78% for PFO [197,198]), and $n^{electrical}_{IQE}$ can be calculated from the earlier equations.

Method 2:

Spontaneous emission is affected by the medium within which the source resides due to the density of states and electromagnetic modes. In 1945, Purcell predicted that spontaneous emission occurs faster within a wavelength-sized cavity than in free space

[199]. This local-field effect is explained by Fermi's Golden Rule in which the transition rate is proportional to the density of optical states as follows. Given a system with an initial excited state, $|i, 0_k\rangle$, with i representing a higher energy state and 0_k represents the absence of photons, and a final state $|f, 1_k\rangle$ with f representing a lower energy state exhibiting emission of a photon with wavenumber, k , Fermi's Golden rule for the transition rate Γ_{if} is as follows:

$$\Gamma_{if} = \frac{2\pi}{\hbar} \rho(\hbar\omega_k) |\langle f, 1_k | H_{int} | i, 0_k \rangle|^2 \quad [\text{B5}]$$

where $H_{int} = -\mathbf{D} \cdot \mathbf{E}$, with \mathbf{D} being the electric dipole moment and \mathbf{E} is the second-quantized electric field at the location of the dipole. $\rho(\hbar\omega_k)$ is the density of states at frequency ω_k , with $k = 2\pi/\lambda$, where λ is the wavelength [200]. When in the presence of an external field the density of states of the source couple to the electromagnetic modes of the field in which the intensity of that field is influenced by the geometry of the medium. Therefore, plasmonic nanostructures have the potential to increase the radiative decay rate by increasing the local density of optical states (i.e., number of optical modes), thus increasing the internal quantum efficiency and resulting in a radiative decay rate enhancement factor [200].

Thus a future direction for this work is to calculate the radiative and non-radiative decay rates using a method similar to that reported by O'Carroll *et al* [201,202]. A box of power monitors is placed around the dipole source as well as around the entire device to compute total power and radiated power, respectively. The total decay rate is computed by integrating the Poynting vector over the closed monitor surface around the dipole emitter. The radiative decay rate is determined by integrating the Poynting vector over the closed monitor surface around the entire device incorporating the dipole emitter, P-OLED

structure and plasmonic nanostructures. The total and radiative decay rates to that in free space is normalized to free space.

The radiative decay rate enhancement factor (F_{rad}) or Purcell factor is the enhancement of the local density of optical states in the active layer, which in turn is equal to the power radiated by a dipole source in an FDTD simulation normalized to the power radiated in a homogeneous medium (typically, free space). Therefore, Purcell factor is written as follows:

$$F_{rad} = \frac{\Gamma_{rad}^{PLED}}{\Gamma_{rad}^o} \quad [B6]$$

where Γ_{rad}^{PLED} is the radiative decay rate for the P-OLED architecture and Γ_{rad}^o is the radiative decay rate in free space. A similar equation is employed to calculate the enhancement in non-radiated decay rate (E_{nrad}) in which the non-radiated decay rate for the material (Γ_{nrad}^{PLED}) is normalized by the radiative decay rate in free space (Γ_{rad}^o), thus resulting in a non-radiated decay rate enhancement. These relative enhancements are used to calculate the internal quantum efficiency for the P-OLED architectures, n_{IQE}^{PLED} as follows:

$$n_{IQE}^{PLED} = \frac{\frac{\Gamma_{rad}^{PLED}}{\Gamma_{rad}^o}}{\frac{\Gamma_{rad}^{PLED}}{\Gamma_{rad}^o} + \frac{\Gamma_{nrad}^{PLED}}{\Gamma_{rad}^o} + \left(\frac{1-n_{IQE}^{electrical}}{n_{IQE}^{electrical}}\right)} \quad [B7]$$

where the relative enhancement factors are given by $\frac{\Gamma_{rad}^{PLED}}{\Gamma_{rad}^o} = F_{rad}$, $\frac{\Gamma_{nrad}^{PLED}}{\Gamma_{rad}^o} = E_{nrad}$ and

$\frac{1-n_{IQE}^{electrical}}{n_{IQE}^{electrical}}$ represents the intrinsic loss associated with the material. Similar to the light-

extraction efficiency enhancement factor the radiative decay rate enhancement factor is determined by the ratio of the Purcell Factor for one nanostructured geometry to a planar reference geometry thus providing information on which nanostructured material and

structure provides the greatest enhancement.

B.2 External Quantum Efficiency

The external quantum efficiency, n_{EQE} , for the P-OLED architectures is calculated by multiplying $n^{100\%elec}_{extraction}$ and $n^{electrical}_{IQE}$; alternatively to account for the local field effects in order to determine n_{EQE} one can multiple $n^{100\%elec}_{extraction}$ and n^{PLED}_{IQE} . The light-extraction efficiency enhancement factor coupled with the radiative decay rate enhancements provides information on the external quantum efficiency enhancement and, hence which nanostructured device should be fabricated and characterized.

Appendix C:

Methods for the Fabrication, Optical and Optoelectronic

Characterization of Polymer Light-Emitting Diode Architectures

Fabrication of the architecture that provides the largest light-extraction efficiency and external quantum efficiency enhancements in the aforementioned simulations is carried out. A procedure for conventional bottom-emitting P-OLED fabrication has been developed in collaboration with undergraduates Sivarampragadeesh Siva and Xiaojun Wang with an emphasis on layer development and thickness optimization. The fabrication procedure includes etching of the anode (ITO) to define the transparent electrode stripes, spin coating of the polymer layers, and thermal evaporation of the metal layers (Fig. C1).

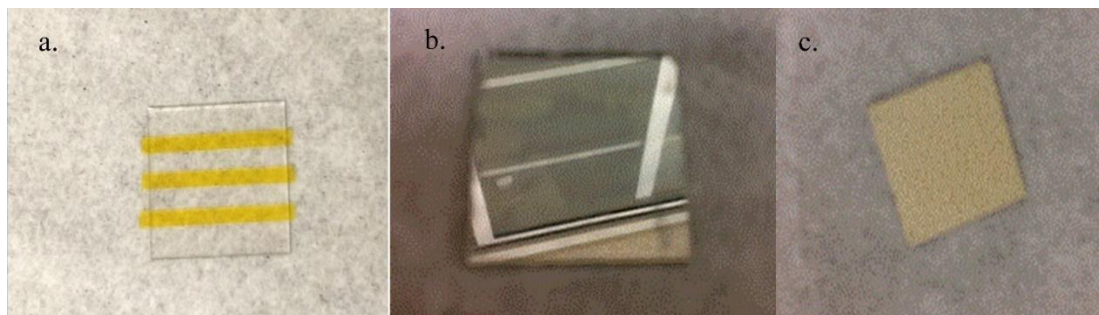


Figure C1: The steps for P-OLED fabrication include etching of the ITO (a), the spin coating of the polymer layers (b), and the thermal evaporation of the metallic layers (c).

The ITO electrodes are defined by placing strips of Kapton™ tape on ITO coated glass and then etching excess ITO with 20% HCl, 5% HNO₃, and 75% water. The polymer layers: PEDOT:PSS and PFO are spin coated with 1.2 weight percent wt% in water and 3000 revolutions per minute (rpm) spin speed and 15 mg/ml in chloroform with 2000 rpm spin

speed respectively onto a glass/ITO substrate. The metal layers: LiF and Al are thermally evaporated at a pressure of $\sim 10^{-6}$ mbar with a deposition rate of ~ 0.1 nm/s and evaporation current of 30 A and 50 A respectively. The final thicknesses are as follows: LiF ~ 2 nm and Al ~ 100 nm. This procedure is a guide for fabricating the planar and nanostructured P-OLED architectures. The plasmonic nanostructures are deposited using spin coating and drop casting using as-synthesised Au, Ag and Cu nanostructures. Nanostructured electrodes are fabricated using methods such as nanoimprint lithography (using polycarbonate (pc) gratings from DVD or CD rotated imprints), dealloying (cothermally evaporated metals are immersed in etchant leaving behind nanoporous metal) and dewetting (thermally evaporated metals are annealed in argon atmosphere glovebox resulting in different porosities and pore areas). These prototypes then undergo optical and optoelectronic characterization to better understand the materials and device physics. Both atomic force spectroscopy (AFM) and ultraviolet-visible (UV-vis) spectroscopy are completed to determine layer thickness. Steps are created on each layer with a toothpick and line scans are averaged from the AFM scans to obtain layer thickness. Using a UV-visible absorption spectrometer the layer thickness is determined from Beers law $T=I/I_0=e^{-\alpha x}$ where T is transmittance, I is the intensity, α is the absorption coefficient, and x is the thickness. Transmittance and reflectance spectra is obtained to determine how transmissive of the transparent electrode layers. The resistivity of the layers is examined using a 4-point probe setup (Figure C2).

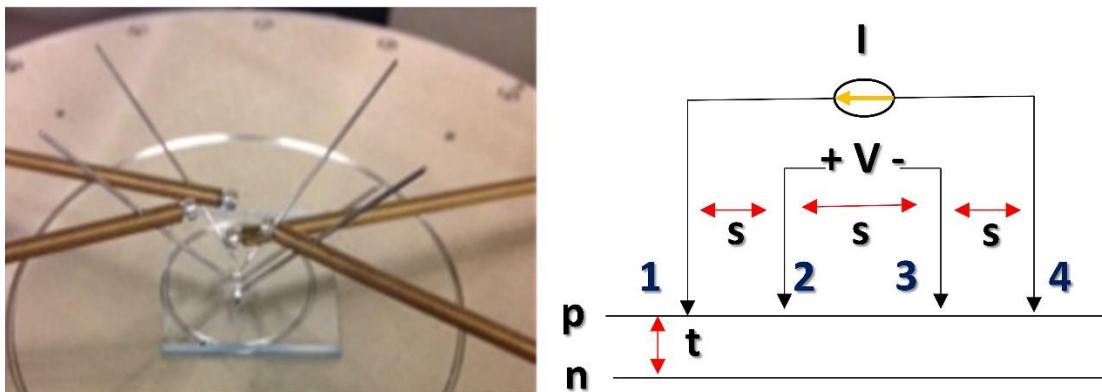


Figure C2: 4-point probe measurements of PEDOT:PSS with current being injected through probes 1 and 4 and voltage being measured between probes 2 and 3.

A fixed current is injected into the two outer probes (1&4) from a Keithley source measure unit and the voltage is measured between the two inner probes (2&3); see Figure C2. A Labview program displays current-voltage (I - V) and resistance ($R=V/I$) plots using the input data from the Keithley and output data from the voltage drop experienced between the two probes. The resistivity, ρ , is then calculated. If the probes have uniform spacing, s , and are placed on an infinite slab material, then the resistivity is given by:

$$\rho = (\pi t \ln 2) V / I \text{ [}\mu\text{Ohm-centimeters]} \text{ for } s \gg t \text{ [C1]}$$

with t representing the thickness of the thin film, V is voltage and I is the current.

Electroluminescence (EL) measurements, the basis of light emission within the devices (radiative recombination following electrical charge injection), is conducted by applying a fixed voltage to the different device architectures. Current-voltage (I - V) and luminance-voltage (L - V) plots are generated using a 2-point probe setup which includes an electrical probe station, Keithley source measure unit (to sweep V), and photodetector to monitor emitted intensity. Using these plots the turn-on voltage of the P-OLEDs and efficacy in (lm/W) for a given luminance (cd/m^2) is determined. The efficacy is calculated using the

photodetector intensity at a given input power ($I \times V$). The luminance is calculated at a particular input power using the detector intensity divided by the light-emitting area of the device (defined by the area of the two overlapping electrodes).

In addition, photoluminescence (PL) spectroscopy is conducted by monitoring the luminescence from P-OLEDs over the visible wavelength range following excitation with a monochromatic laser to incite optical excitation transitions within the P-OLEDs. The resulting PL emission spectra provides information on the electronic energy level structure of the P-OLEDs. Further, EL spectroscopy is completed by modifying the existing PL spectroscopy setup to incorporate electrical probes. The EL spectral emission profile enables one to study charge carrier injection, charge carrier transport and recombination mechanisms that occur during the time lapse between electrical stimulation and emission since the shape of the emission profile is dependent on charge mobility and injection conditions. The PL and EL spectral enhancements is compared between planar and nanostructured devices.

The theoretical external quantum efficiency for the P-OLED architectures is be compared to the experimental external quantum efficiency results calculated from the measured efficacy at a given luminance describe above. In order to convert efficacy (in lumens/W; i.e., optical power/electrical power) to external quantum efficiency, the emitted optical power in lumens must be converted to optical power in watts. First, the luminous flux, Φ , the energy per unit time that is radiated from a material over the visible wavelength range, in lumens for the P-OLED architectures by carrying out EL vs. emission angle measurements is measured. Then, the results for the luminous flux will be divided by the efficacy to obtain power $P_{\text{out}}^{\text{W}} = \Phi / E_f$.

References

1. N. Karl, "Organic Semiconductors", in O. Madelung, M. Schulz, and H. Weiss (eds.), LandoltBoernstein (New Series), Group III, Vol. 17, Semiconductors, Subvolume 17i, p. 106. Springer, Berlin, 1985.
2. E. A. Silinsh, Organic Molecular Crystals. Springer, Berlin 1980.
3. M. Pope and C. E. Swenberg, Electronic Processes in Organic Crystals and Polymers. Oxford University Press, Oxford 1999.
4. A. J. Heeger (2001) Semiconducting and metallic polymers: the fourth generation of polymeric materials (Nobel lecture). *Angew. Chem. Int. Ed.* **40** (14), 2591.
5. C. K. Chiang *et al* (1977) Electrical conductivity in doped polyacetylene. *Phys. Rev. Lett.* **39** (17), 1098.
6. C.W. Tang and S.A. VanSlyke (1987) Organic electroluminescent diodes. *Appl. Phys. Lett.* **51** (12), 913.
7. J. H. Burroughes *et al* (1990) Light-emitting diodes based on conjugated polymers. *Nat.* **347**, 539.
8. W. Brütting, "Organic Semiconductors," Semiconductors, vol. 6, 1–11, 2005.
9. K. M. Pelzer *et al* (2017) Molecular dynamics and charge transport in organic semiconductors: a classical approach to modeling electron transfer. *Chem. Sci.* **8**, 2597.
10. C. Groves (2017) Simulating charge transport in organic semiconductors and devices: a review *Rep. Prog. Phys.* **80**, 026502.

11. H. Bassler and A. Kohler (2102) Charge Transport in Organic Semiconductors. *Top Curr Chem.* **312**, 1.
12. S. Reineke *et al* (2013) White organic light-emitting diodes: *Status and perspective. Reviews of Modern Physics.* **85**, 1.
13. P. I. Djurovich, E. I. Mayo, S. R. Forrest, and M. E. Thompson (2009) Measurement of the lowest unoccupied molecular orbital energies of molecular organic semiconductors. *Org. Electron.* **10**, 515.
14. S. M. Tadayyon *et al* (2004) Reliable and reproducible determination of work function and ionization potentials of layers and surfaces relevant to organic light emitting diodes. *Org. Electron.* **5**, 199.
15. C. Sekine *et al* (2014) Recent progress of high performance polymer OLED and OPV materials for organic printed electronics. *Sci. Technol. Adv. Mater.* **15**, 1.
16. A. Swist and J. Soloducho (2012) Organic semiconductors – materials of the future? *CHEMIK.* **66** (4), 289.
17. C. F. Wang *et al* (2013). Functionalized terfluorene for solution- processed high efficiency blue fluorescence OLED and electrophosphorescent devices. *Org. Electron.* **14**, 1958.
18. D. Fyfe (2009). Organic displays come of age. *Nat. Photon.* **3**, 453.
19. F. So and D. Kondakov (2010). Degradation Mechanisms in Small- Molecule and Polymer Organic Light-Emitting Diodes. *Adv. Mater.* **22**, 3762.
20. C. J. M. Emmott, A. Urbina and J. Nelson (2012). Environmental and economic assessment of ITO-free electrodes for organic solar cells. *Sol. Energy Mater. Sol. Cells.* **97**, 14.

21. S. Lizin *et al* (2013). Life cycle analyses of organic photovoltaics: a review. *Energy Environ. Sci.* **6**, 3136
22. S. B. Darling and F. You (2013). The case of organic photovoltaics. *RSC Adv.* **3**, 17633.
23. U. S. Department of Energy (2012). Life-Cycle Assessment of Energy and Environmental Impacts of LED Lighting Products, Part I: Review of the Life-Cycle Energy Consumption of Incandescent, Compact Fluorescent, and LED Lamps. Solid-State Lighting Program. U.S. Department of Energy. Available from: http://apps1.eere.energy.gov/buildings/publications/pdfs/ssl/2012_LED_Lifecycle_Report.pdf (accessed February 2014).
24. P. de Bruyn, D. J. D. Moet and P. W. M. Blom (2012). All- solution processed polymer light-emitting diodes with air stable metal-oxide electrodes. *Org. Elect.* **13**, 1023.
25. U. S. Department of Energy (2014). Solid-State Lighting Manufacturing Research and Development Roadmap. Available from: http://apps1.eere.energy.gov/buildings/publications/pdfs/ssl/ssl_mfg_roadmap_aug_2014.pdf (accessed October 2015).
26. S. R. Tseng *et al* (2007). High-efficiency blue multilayer polymer light-emitting diode based on poly(9,9-dioctylfluorene). *J. Appl. Phys.* **101**, 1.
27. R. Trattnig *et al* (2013). Bright Blue Solution Processed Triple-Layer Polymer Light-Emitting Diodes Realized by Thermal Layer Stabilization and Orthogonal Solvents. *Adv Func. Mat.* **23**, 4897.

28. H. Zheng *et al* (2013). All-solution processed polymer light-emitting diode displays. *Nat. Commun.* **4**,1.
29. V. Bodrozic *et al* (2008). The Built In Potential in Blue Polyfluorene-Based Light Emitting Diodes. *Adv. Mat.* **20**, 2410.
30. H. Yan *et al* (2003). High-Brightness Blue Light-Emitting Polymer Diodes via Anode Modification Using a Self- Assembled Monolayer. *Adv. Mater.* **10**, 835.
31. T. M. Brown *et al* (1999). Built in field electroabsorption spectroscopy of polymer light-emitting diodes incorporating a doped poly(3,4-ethylene dioxythiophene) hole injection layer. *Appl. Phys. Lett.* **75**, 1679.
32. C. C. Hsiao, A.E. Hsiao, and S.A. Chen (2008). Design of Hole Blocking Layer with Electron Transport Channels for High Performance Polymer Light-Emitting Diodes. *Adv. Mater.* **20**, 1982.
33. T. M. Brown and R. H. Friend (2003). Electronic line-up in light-emitting diodes with alkali-halide/metal cathodes. *Appl. Phys. Lett.* **93**, 6159.
34. E. L. William *et al* (2007). Excimer-based white phosphorescent organic light-emitting diodes with nearly 100% internal quantum efficiency. *Adv. Mater.* **19**, 197.
35. S. Y. Kim and J. J. Kim (2010). Outcoupling efficiency of organic light emitting diodes and the effect of ITO thickness. *Org. Electron.* **11**, 1010.
36. C. F. Madigan, M. H. Lu and J. C. Sturm (2000). Improvement of output coupling efficiency of organic light-emitting diodes by backside substrate modification. *Appl. Phys. Lett.* **76**, 1650.
37. X. Y. Deng (2011). Lighting- Emitting Devices with Conjugated Polymers. *Int. J. Mol. Sci.* **12**, 1575.

38. S. H. Chen and S. C. Chan (2012). Light Enhancement of Plasmonic Nanostructures for Polymer Light-Emitting Diodes at Different Wavelengths. *Appl. Phys. Express* **5**, 1.
39. X. H. Li *et al* (2012). Efficient Inverted Polymer Solar Cells with Directly Patterned Active Layer and Silver Back Grating. *J. Phys. Chem. C*. **116**, 7200.
40. J. Zhong *et al* (2012). Effect of Encapsulation Technology on Organic Light Emitting Diode Lifetime. *Opt. Rev.* **19**, 82.
41. M. F. Ashby (2013). *Materials and the Environment*. Butterworth-Heinemann 2nd edition.
42. T Swarr *et al* (2011) *Environmental life cycle costing: a code of practice*. SETAC Press, Pensacola, ISBN 978-1-880611- 87-6.
43. N. Espinosa and F. C. Krebs (2014). Life cycle analysis of organic tandem solar cells: When are they warranted? *Sol. Energy Mater. Sol. Cells*. **120**, 692.
44. L. Tahkamo *et al* (2013). Life cycle assessment of light-emitting diode downlight luminaire - a case study. *Int. J. Life Cycle Assess.* **18**, 1009.
45. D. Yue *et al* (2012). Deciphering the uncertainties in life cycle energy and environmental analysis of organic photovoltaics. *Energy Environ. Sci.* **5**, 9163.
46. R. Garcí'a-Valverde, J. A. Cherni and A. Urbina (2010). Life cycle analysis of organic photovoltaics. *Prog. Photovolt: Res. Appl.* **18**, 535.
47. N. Espinosa *et al* (2011). A life cycle analysis of polymer solar cell modules prepared using roll-to-roll methods under ambient conditions. *Sol. Energy Mater. Sol. Cells* **95**, 1293.

48. B. Azzopardi et al (2011). Economic Assessment of Solar Electricity Production from Organic-Based Photovoltaic Modules In A Domestic Environment. *Energy Environ. Sci.* **4**, 3741.
49. Anctil et al (2012). Cumulative energy demand for small molecule and polymer photovoltaics. *Prog. Photovolt.: Res. Appl.* **21**, 1541.
50. Y.S. Zimmerman et al. (2012). Organic photovoltaics: Potential fate and effects in the environment. *Environ. Int.* **49**, 128.
51. C. Kapnopoulos *et al* (2016). Fully gravure printed organic photovoltaic modules: A straightforward process with a high potential for large scale production. *Sol. Energy Mater. Sol. Cells.* **144**, 724.
52. M. T. Llyod et al. (2011). Influence of the hole-transport layer on the initial behavior and lifetime of inverted organic photovoltaics. *Sol. Energy Mater. Sol. Cells.* **95**, 1382.
53. Y. L. Powell and T. Bender (2012). Using stochastic model to determine financial indicator and technical objectives for organic solar cells. *Sol. Energy Mater. Sol. Cells.* **107**, 236.
54. C. J. Mulligan et al (2014). A projection of commercial scale organic photovoltaic module costs. *Sol. Energy Mater. Sol. Cells.* **120**, 9.
55. J. Schmidtke (2010). Commercial status of thin-film photovoltaic devices and materials. *Opt. Express.* **18**, A477.
56. E. Alsema (1998). Energy requirements of thin-film solar cell modules - a review. *Renew. Sustain. Energy Rev.* **2**, 387.

57. International Organization for, Standardization, ISO 14040 series. Environmental management --- life cycle assessment, 2006.
58. H. Bauman and A.M. Tillman (2004). *The Hitch Hiker's Guide to LCA*. Studentlitteratur AB, Lund, ISBN-10:9144023642.
59. J. H. Youn *et al* (2013). Improving the lifetime of a polymer light-emitting diode by introducing solution processed tungsten oxide. *J. Mater. Chem. C*, **1**, 3250.
60. M. Roberts *et al* (2013). High efficiency Polymer OLEDs - analysis and progress. *SPIE Opt. Photon.* <https://www.cdtltd.co.uk/pdf/spie2013-mroberts-cdt.pdf> (accessed Feb. 09 2016).
61. T. -Y. Chu *et al* (2006). Highly efficient and stable inverted bottom-emission organic light emitting devices. *Appl. Phys. Lett.* **89**, 053503.
62. S. -Y. Chen *et al* (2006). Stable inverted bottom-emitting organic electroluminescent devices with molecular doping and morphology improvement. *Appl. Phys. Lett.* **89**, 053518.
63. D. Fyfe (2009). Organic displays come of age. *Nat. Photon.* **3**, 453.
64. E. Fred Schubert, *Light-Emitting Diodes*, Chapter 16, Cambridge University Press, Cambridge, UK (2006).
65. N. Na, J. Jang and H.-J. Suk (2014). Dynamics of Backlight Luminance for Using Smartphone in Dark Environment. *Proc. of SPIE*, **9014**, 1.
66. M. H. Chang *et al* (2012). Light emitting diodes reliability review. *Microelec. Reliability* **5**, 762.
67. Joint Research Centre of the European Commission (2012). International Reference Life Cycle Data System (ILCD) Handbook, General Guide for Life Cycle

Assessment, detailed guidance, Joint Research Centre, Institute for Environment and Sustainability, Publications Office of the European Union, Luxembourg, 2010. Available from: http://publications.jrc.ec.europa.eu/repository/bitstream/JRC48157/ilcd_handbook-general_guide_for_lca-detailed_guidance_12march2010_isbn_fin.pdf (accessed May 2016).

68. A. Kohler and H. Bassler (2015). *Electronic Processes in Organic Semiconductors: An Introduction*. Wiley Press, ISBN: 978-3-527-33292-2.
69. B. D. Chin *et al* (2004). Effects of cathode thickness and thermal treatment on the design of balanced blue light-emitting polymer device. *Appl. Phys. Lett.* **85**, 4496.
70. H. J. Bolink *et al* (2007). Air stable hybrid organic-inorganic light emitting diodes using ZnO as the cathode. *Appl. Phys. Lett.* **91**, 1.
71. C. Y. Wu *et al* (2010). Flexible inverted bottom-emitting organic light-emitting devices with semi-transparent metal-assisted electron-injection layer. *J. Soc. Info. Display* **18**, 76.
72. W. Liu *et al* (2014). Efficient inverted organic light-emitting devices with self or intentionally Ag-doped interlayer modified cathode. *Appl. Phys. Lett.* **104**, 1.
73. J. Liu *et al* (2014). Achieving above 30% external quantum efficiency for inverted phosphorescence organic light-emitting diodes based on ultrathin emitting layer. *Org. Electron.* **15**, 2492.
74. X. W. Zhang *et al* (2012). A very simple method of constructing efficient inverted top-emitting organic light-emitting diode based on Ag/Al bilayer reflective cathode. *J. Luminesce.* **132**, 1.

75. K. A. Knauer *et al* (2012). Inverted top-emitting blue electrophosphorescent organic light-emitting diodes with high current efficacy. *Appl. Phys. Lett.* **101**, 103304.
76. S. Hofle *et al* (2014). Solution processed, white emitting tandem organic light-emitting diodes with inverted device architecture. *Adv. Mater.* **26**, 5155.
77. J. Chem (2012). Solution-processable small molecules as efficient universal bipolar host for blue, green, and red phosphorescent inverted OLEDs. *J. Mater. Chem.* **22**, 5164.
78. Super Bright LEDs Inc., Super-Blue LED (InGaN), Part Number: RL5-B55a5, <https://www.superbrightleds.com/moreinfo/through-hole/5mm-blue-led-15-degree-viewing-angle-5500-mcd/269/> (May 2016).
79. JKL Components Corp., T-1 3/4 Wedge Base 12 Volt LED, Part Number LE-0504-01B, <http://www.jkllamps.com/led/wedgebaseleds> (May 2016).
80. TAIWAN HongGuang 3W RGB LED Emitter (white) (distributed by Fancy Cost, Item Code 1068112); only specifications for the blue LED component used in this study.
81. CREE, Inc., Xlmap MC-E RGBW (<http://www.cree.com/LED-Components-and-Modules/Products/XLamp/Arrays-Directional/XLamp-MCE>); only specifications for the blue LED component was used in this study.
82. O. V. Mikhnenko, P. W. M. Blom and T. Q. Nguyen (2015). Exciton diffusion in organic semiconductors, *Energy Environ. Sci.* **8**, 1867.
83. Euro to dollar conversion factor of 1.35 was employed (November, 2013).
84. N.Narendran *et al* (2004) Solid- state lighting: Failure analysis of white LEDs. *J. Cryst. Grow.* **268**, 449.

85. State Electricity Profile 2010. DOE/EIA-0348(01)/2. Released January 27, 2012. <http://www.eia.gov/electricity/state/pdf/sep2010.pdf> (accessed October 2015).
86. J. A. deGouw *et al* (2014). Reduced emissions of CO₂, NO_x, and SO₂ from U.S. power plants owing to switch from coal to natural gas with combined cycle technology. *Earth's Future*, **2**, 75-82, doi:10.1002/2013EF000196.
87. M. Lu, P. Bruyn, H. T. Nicolai and G. J. Wetzelaer (2012). Hole-enhanced electron injection from ZnO in inverted polymer light-emitting diodes. *Org. Elect.* **13**, 1693.
88. V. N. Bliznyuk *et al* (1999). Electrical and Photoinduced Degradation of Polyfluorene Based Films and Light Emitting Devices. *Macromol.* **32**, 361.
89. S. A. Choulis *et al* (2005). The effect of interfacial layer on the performance of organic light emitting diodes. *Appl. Phys. Lett.* **87**, 1.
90. D. Kasama *et al* (2009). Improved Light Emission Utilizing Polyfluorene Derivatives by Thermal Printing and Solution Process. *Proc. SPIE.* **7415**, 1.
91. Q. Zhao, S.J. Liu and W. Huang (2009). Polyfluorene-Based Blue-Emitting Materials. *Macro. Chem. Phys.* **210**, 1580.
92. T. F. Guo *et al* (2001). High Performance Polymer Light- Emitting Diodes Fabricated by a Low Temperature Lamination Process. *Adv. Funct. Mat.* **11**, 339.
93. H. J. Bolink *et al* (2008). Inverted Solution Processable OLEDs using a metal oxide as electron injection contact. *Proc. of SPIE* **6999**, 69992X1.
94. H. Choi *et al* (2011). Combination of Titanium Oxide and a Conjugated Polyelectrolyte for High-Performance Inverted Type Organic Optoelectronic Devices. *Adv. Mater.* **23**, 2759.

95. D. Kabra *et al* (2010). Efficient Single Layer Polymer Light Emitting Diodes. *Adv. Mater.* **22**, 3194.
96. F. So and D. Kondakov (2010). Degradation Mechanisms in Small- Molecule and Polymer Organic Light-Emitting Diodes. *Adv. Mater.* **22**, 3762.
97. X. H. Li *et al* (2012). Efficient Inverted Polymer Solar Cells with Directly Patterned Active Layer and Silver Back Grating. *J. Phys. Chem. C* **116**, 7200.
98. H. J. Bolink *et al* (2010). Phosphorescent Hybrid Organic-Inorganic Light-Emitting Diodes. *Adv. Mater.* **2**, 2198.
99. S. N. Hsieh *et al* (2009). Surface modification of TiO₂ by a self-assembly monolayer in inverted-type polymer light emitting devices. *Org. Elect.* **10**, 1626.
100. J. S. Park *et al* (2011). High performance polymer light-emitting diodes with n-type metal oxide/conjugated polyelectrolyte hybrid charge transport layers. *Appl. Phys. Lett.* **99**, 163305-1.
101. X. W. Zhang *et al* (2013). Improving electron injection and microcavity effect for constructing highly efficient inverted top-emitting organic light-emitting diode. *Opt. Laser Technol.* **45**, 181.
102. Y. Y. Zhang and Y. A. Yin (2011). Performance enhancement of blue light-emitting diodes with a special designed AlGa_N/Ga_N superlattice electron-blocking layer. *Appl. Phys. Lett.* **99**, 221103.
103. R. Dahal *et al* (2010). 1.54 μm emitters based on erbium doped InGa_N p-i-n junctions. *Appl. Phys. Lett.* **97**, 141109.
104. Ted Pella, Inc. "Glass Microscope Slide" (Nov 20 2012)
http://www.tedpella.com/histo_html/slides.htm

105. S. Xiao *et al* (2005). Effects of Solvent on Fabrication of Polymeric Light Emitting Devices. *Mat. Lett.* **59**, 694.
106. Heraeus Clevios. "Printing Conductivity" (Nov. 20 2012) <http://www.heraeus-clevios.com/media/webmedia_local/media/technical_informations_flyer/document_HCS_Flyer_CLEVIOS_Printing.pdf>
107. Sigma Aldrich "655201 - Poly(3,4-ethylenedioxythiophene)-poly(styrenesulfonate)" (Oct 11 2013)
<http://www.sigmaaldrich.com/catalog/product/aldrich/655201?lang=en®ion=US>
108. Sigma Aldrich. "571652 - Poly(9,9-di-n-octylfluorenyl-2,7-diyl)" (Oct 11 2013)
<http://www.sigmaaldrich.com/catalog/product/aldrich/571652?lang=en®ion=US>
109. Sigma Aldrich. "449903 - Lithium fluoride" (Oct 11 2013)
<http://www.sigmaaldrich.com/catalog/product/aldrich/449903?lang=en®ion=US>
110. Sigma Aldrich "266523 - Aluminum" (Oct 11 2013)
<http://www.sigmaaldrich.com/catalog/product/sial/266523?lang=en®ion=US>
111. Sigma Aldrich. "204757-Titanium(IV) oxide" (Oct 11 2013)
<http://www.sigmaaldrich.com/catalog/product/aldrich/204757?lang=en®ion=US>
112. Sigma Aldrich. "203815 - Molybdenum(VI) oxide" (Oct 11 2013)
<http://www.sigmaaldrich.com/catalog/product/aldrich/203815?lang=en®ion=US>

113. Sigma Aldrich. “327050-Silver” (Oct 11 2013)
<http://www.sigmaaldrich.com/catalog/product/aldrich/327050?lang=en®ion=US>
114. O. Tsydenova and M. Bengtsson (2011). Chemical hazards associated with treatment of waste electrical and electronic equipment. *Waste Manage.* **31**, 45.
115. J. D. Lincoln *et al* (2007). Leaching Assessments of Hazardous Materials in Cellular Telephones. *Environ. Sci. Technol.* **41**, 2572.
116. <http://minerals.usgs.gov/minerals/pubs/commodity/recycle/recymyb01.pdf>
117. R. Geyer and V. D. Blass (2010). The economics of cell phone reuse and recycling. *Int. J Adv. Manuf. Technol.* **47**, 515.
118. B. H. Robinson (2009). E-waste: An assessment of global production and environmental impacts. *Sci. Total Environ.* **408**, 183.
119. J. L. Sullivan and L. Gaines (2012). Status of life cycle inventories for batteries. *Energy Convers. Manage.* **58**, 34.
120. G. P. Hammond and C. I. Jones (2008). Embodied energy and carbon in construction materials. *Proc. Inst. Civil Eng. – Energy.* **161**, 87.
121. G.F. Grubb and B.R. Bakshi (2010). Life Cycle of Titanium Dioxide Nanoparticle Production. *J. Ind. Ecol.* **15**, 81.
122. N. Osterwalder *et al* (2006). Energy consumption during nanoparticle production: How economic is dry synthesis? *J. Nanopart. Res.* **8**, 1.
123. S. J. Hong, *Characteristics of Indium Tin Oxide (ITO) Glass Re-Used from Old TFT-LCD Panel*, (<https://www.jim.or.jp/journal/e/pdf3/53/05/968.pdf>).

- 124.V. Zardetto *et al* (2011). Substrates for Flexible Electronics: A Practical Investigation on the Electrical, Film Flexibility, Optical, Temperature, and Solvent Resistance. *J. Poly. Sci. Part B: Poly. Phys.* **49**, 638.
- 125.ARENA (2014). Market Technology Analysis Lessons Learnt. Australian Renewable Energy Agency. Available from:http://arena.gov.au/files/2014/06/Market-Technology-Analysis_-_Lessons-Learnt.pdf (Accessed May 2016).
- 126.F. C. Krebs *et al* (2014). 25th Anniversary Article: Rise to Power - OPV-Based Solar Parks. *Adv. Mater.* **26**, 29.
- 127.M. Corazza, F. C. Krebs, S. A. Gevorgyan (2015). Lifetime of organic photovoltaics: Linking outdoor and indoor tests. *Sol. Energy Mater. Sol. Cells.* **143**, 467.
- 128.C. J. M. Emmott *et al* (2016). In-situ, long-term operational stability of organic photovoltaics for off-grid applications in Africa. *Sol. Energy Mater. Sol. Cells.* **149**, 284.
- 129.P. Kumar *et al* (2016). Comparing the degradation of organic photovoltaic devices under ISOS testing protocols. *Sol. Energy Mater. Sol. Cells.* **149**, 179.
- 130.Z. Ding *et al* (2016). Efficient solar cells are more stable: the impact of polymer molecular weight on performance of organic photovoltaics. *J. Mater. Chem. A* **4**, 7274.
- 131.S. A. Gevorgyan *et al* (2016). Lifetime of Organic Photovoltaics: Status and Predictions. *Adv. Energy Mater.* **6**, 1501208.

132. C. H. Peters *et al* (2011). High Efficiency Polymer Solar Cells with Long Operating Lifetimes. *Adv. Energy Mater.* **1**, 491.
133. T. T. Larsen-Olsen *et al* (2013). A round robin study of polymer solar cells and small modules across China. *Sol. Energy Mater. Sol. Cells* **117**, 382.
134. A. M. Nardes *et al* (2014). Thermal annealing affects vertical morphology, doping and defect density in BHJ OPV devices. *40th IEEE Photovoltaic Specialist Conference (IEEE-PVSC)* 2575.
135. M. C. Gather, A. Koehnen, and K. Meerholz, (2011). White organic light-emitting diodes. *Adv. Mater.* **23**(2), 233.
136. W. Jiang *et al* (2011). High-triplet-energy tri-carbazole derivatives as host materials for efficient solution-processed blue phosphorescent devices. *J. Mater. Chem.* **21**(13), 4918.
137. H. Liu *et al* (2014). Solution-processable hosts constructed by Carbazole/PO substituted tetraphenylsilanes for efficient blue electrophosphorescent devices. *Adv. Funct. Mater.* **24**(37), 5881.
138. D. Ma, L. Duan, and Y. Qiu (2016). Toward highly efficient blue organic light-emitting diodes: Fabricating a good-quality emissive layer cast from suitable solvents. *Dalton Transactions.* **45**(14), 6118.
139. Y. Qian, F. Cao, and W. Guo (2013). High thermal stability 3, 6-fluorene-carbazole-dendrimers as host materials for efficient solution-processed blue phosphorescent devices. *Tetrahedron.* **69**(21), 4169.

- 140.Z. Shen and D. M. O'Carroll (2015). Nanoporous Silver Thin Films: Multifunctional Platforms for Influencing Chain Morphology and Optical Properties of Conjugated Polymers. *Adv Funct Mater*, **25**, 3302.
- 141.M. Siss (2015). Spectroscopy of Light Emitting Polymers on Nano-Structured Metal Electrodes. Fall Progress Report.
142. Thorlabs. Light Emitting Diode Technologies. Radiometric vs. Photometric Units. <https://www.thorlabs.de/catalogPages/506.pdf>
- 143.S. Su *et al* (2009). Structure-property relationship of pyridine-containing triphenyl benzene electron-transport materials for highly efficient blue phosphorescent OLEDs. *Adv Funct Mater*, **19**(8), 1260.
- 144.Y. Tao, C. Yang, and J. Qin (2011). Organic host materials for phosphorescent organic light-emitting diodes. *Chem Soc Rev*. **40**(5), 2943.
- 145.J. Wang *et al* (2015). Origin of efficiency roll-off for FIrpic based blue organic light-emitting diodes and implications on phosphorescent molecule design. *Jpn. J. Appl. Phys.* **54**(10), 1016001-1.
146. Y. Zhang *et al* (2015). Spiro-fused N-phenylcarbazole-based host materials for blue phosphorescent organic light-emitting diodes. *Org Elec.* **20**, 112.
- 147.Y. Zhao *et al* (2016). Efficiency roll-off suppression in organic light-emitting diodes at high current densities using gold bowtie nanoantennas. *Appl Phys Exp.***20**, 022101-1.
- 148.M. T. Lee *et al* (2009). Suppression of efficiency roll off in blue phosphorescent organic light-emitting devices using double emission layers with additional carrier-transporting material. *Appl Phys Lett.* **94**, 083506-1.

- 149.H. Eersel *et al* (2014). Monte Carlo study of efficiency roll off of phosphorescent organic light-emitting diodes: Evidence for dominant role of triplet-polaron quenching. *Appl Phys Lett.* **105**, 143303-1.
- 150.M. A. Baldo, C. Adachi, and S. R. Forrest (2000). Transient analysis of organic electrophosphorescence: I. Transient analysis of triplet energy transfer. *Phys. Rev. B.* **62**, 10967.
- 151.F. X. Zang *et al* (2008). Reduced efficiency roll- off in phosphorescent organic light emitting diodes at ultrahigh current densities by suppression of triplet-polaron quenching. *Appl. Phys. Lett.* **93**, 023309.
- 152.N. C. Giebink and S. R. Forrest (2008). Quantum efficiency roll-off at high brightness in fluorescent and phosphorescent organic light emitting diodes. *Phys. Rev. B.* **77**, 235215.
- 153.D. Song *et al* (2010). Causes of efficiency roll- off in phosphorescent organic light emitting devices: Triplet – triplet annihilation versus triplet-polaron quenching. *Appl. Phys. Lett.* **97**, 243304.
154. S. II. Yoo *et al* (2015). Improvement of efficiency roll-off in blue phosphorescent OLED using double dopants emissive layer. *Jour of Luminescence.* **160**, 346.
- 155.S. H. Kim *et al* (2008). Stable efficiency roll-off in phosphorescent organic light-emitting diodes *Appl. Phys. Lett.* **92**, 023513.
- 156.F. X. Zang *et al* (2008). Reduced efficiency roll- off in phosphorescent organic light emitting diodes at ultrahigh current densities by suppression of triplet-polaron quenching. *Appl. Phys. Lett.* **93**, 023309.

- 157.S. Reineke, K. Walzer, and K. Leo (2007). Triplet-exciton quenching in organic phosphorescent light-emitting diodes with Ir-based emitters. *Phys. Rev. B.* **75**, 125328.
158. W. Ji, L. Zhang, W. Xie (2012). Improving efficiency roll-off in phosphorescence OLEDs by modifying the exciton lifetime. *Opt Lett.* **37** (11), 2019.
- 159.C. Xiang *et al* (2016). Efficiency Roll-Off in Blue Emitting Phosphorescent Organic Light Emitting Diodes with Carbazole Host Materials. *Adv Funct Mater.* **26**, 1463.
- 160.M.T. Lloyd *et al* (2011). Influence of the hole-transport layer on the initial behavior and lifetime of inverted organic photovoltaics. *Sol. Energy Mater. Sol. Cells.* **95**, 1382.
- 161.S.P. Subbarao, M.E. Bahlke, and I. Kymissis (2010). Laboratory thin-film encapsulation of air-sensitive organic semiconductor devices. *IEEE Trans. Electron Dev.*, **57** (1) 153.
- 162.I.D. Parker, Y. Cao, and C.Y. Tang (1999). Lifetime and degradation effects in polymer light-emitting diodes. *Jour Appl Phys.* **85** (4), 2441.
- 163.Y.C. Tsai and J.H. Jou (2006). Long-lifetime, high efficiency white organic light-emitting diodes with mixed host composing double emission layers. *Appl Phys Lett* **89**, 24352-1.
- 164.D. Kasama *et al* (2009). Improved Light Emission Utilizing Polyfluorene Derivatives by Thermal Printing and Solution Process. *Proc. SPIE.* **7415**, 1.
- 165.Q. Zhao, S.J. Liu and W. Huang (2009). Polyfluorene-Based Blue-Emitting Materials. *Macro. Chem. Phys.* **210**, 1580.

- 166.T. F. Guo *et al* (2001). High Performance Polymer Light- Emitting Diodes Fabricated by a Low Temperature Lamination Process. *Adv. Funct. Mat.* **11**, 339.
- 167.H. J. Bolink *et al* (2008). Inverted Solution Processable OLEDs using a metal oxide as electron injection contact. *Proc. of SPIE* **6999**, 69992X1.
- 168.H. Choi *et al* (2011). Combination of Titanium Oxide and a Conjugated Polyelectrolyte for High-Performance Inverted Type Organic Optoelectronic Devices. *Adv. Mater.* **23**, 2759.
- 169.D. Kabra *et al* (2010). Efficient Single Layer Polymer Light Emitting Diodes. *Adv. Mater.* **22**, 3194.
- 170.F. So and D. Kondakov (2010). Degradation Mechanisms in Small- Molecule and Polymer Organic Light-Emitting Diodes. *Adv. Mater.* **22**, 3762-3777.
- 171.X. H. Li *et al* (2012). Efficient Inverted Polymer Solar Cells with Directly Patterned Active Layer and Silver Back Grating. *J. Phys. Chem. C.* **116**, 7200.
- 172.H. J. Bolink *et al* (2010). Phosphorescent Hybrid Organic-Inorganic Light-Emitting Diodes. *Adv. Mater.* **2**, 2198.
- 173.S. N. Hsieh *et al* (2009). Surface modification of TiO₂ by a self-assembly monolayer in inverted-type polymer light emitting devices. *Org. Elect.* **10**, 1626.
- 174.J. S. Park *et al* (2011). High performance polymer light-emitting diodes with n-type metal oxide/conjugated polyelectrolyte hybrid charge transport layers. *Appl. Phys. Lett.* **99**, 163305-1.
- 175.X. W. Zhang *et al* (2013). Improving electron injection and microcavity effect for constructing highly efficient inverted top-emitting organic light-emitting diode. *Opt. Laser Technol.* **45**, 181.

176. Y. Y. Zhang and Y. A. Yin (2011). Performance enhancement of blue light-emitting diodes with a special designed AlGaIn/GaN superlattice electron-blocking layer. *Appl. Phys. Lett.* **99**, 221103.
177. R. Dahal, C. Ugolini, J. Y. Lin, H. X. Jiang, J. M. Zavada (2010). 1.54 μm emitters based on erbium doped InGaIn p-i-n junctions. *Appl. Phys. Lett.* **97**, 141109.
178. Ted Pella, Inc. "Glass Microscope Slide" (Nov 20 2012)
http://www.tedpella.com/histo_html/slides.htm
179. S. Xiao *et al* (2005). Effects of Solvent on Fabrication of Polymeric Light Emitting Devices. *Mat. Lett.* **59**, 694.
180. J.W. Kim *et al* (2014). FDTD analysis of the light extraction efficiency of OLEDs with a random scattering layer. *Optics Express.* **22** (1) 498.
181. X. Shi *et al* (2014). High-performance green phosphorescent top-emitting organic light-emitting diodes based on FDTD optical simulation. *Org Elec* **15**, 864.
182. A. Rostami *et al* (2013). Light extraction efficiency enhancement in organic light emitting diodes based on optimized multilayer structures. *Optik.* **124**(18) 3287.
183. J.A.E. Wasey *et al* (2000). Effects of dipole orientation and birefringence on the optical emission from thin films. *Opt Commun.* **183**, 109.
184. M. Flammich *et al* (2010). Orientation of emissive dipoles in OLEDs: Quantitative in situ analysis. *Org Elec.* **11** (6). 1039.
185. D. McBranch *et al* (1995). Optical determination of chain orientation in electroluminescent polymer films. *Appl Phys Lett.* **66** (10) 1175.

186. S. M. King, H. L. Vaughan, A. P. Monkman (2007). Orientation of triplet and singlet transition dipole moments in polyfluorene, studied by polarized spectroscopies. *Chem Phys Lett.* **40**, 268.
187. B. J. Scholz *et al* (2012). Extraction of surface plasmons in organic light-emitting diodes via high-index coupling. *Opt. Express.* **20**, A205.
188. *Lumerical FDTD Solutions*, version 7.5.7; Lumerical Solutions, Inc.: Vancouver, BC, 2011
189. Taflove, A.; Hagness, S. C (2005). *Computational Electrodynamics: The Finite Difference Time-Domain Method*, 3rd ed.; Artech House: Norwood, MA.
190. G.F. Burkhard, E. T. Hoke, M. D. McGehee (2010). Accounting for interference, scattering, and electrode absorption to make accurate internal quantum efficiency measurements in organic and other thin solar cells. *Adv. Mater.* **22**, 3293.
191. Postava, K. *et al* (2000). Spectroscopic ellipsometry of epitaxial ZnO layer on sapphire substrate. *J. Appl. Phys.* **87**, 7820.
192. M. Campoy-Quiles *et al* (2005). Ellipsometric Characterization of the Optical Constants of Polyfluorene Gain Media. *Adv Funct Mater.*, **15** 925.
193. Y.R. Do (2004). Enhanced light-extraction efficiency from organic light-emitting diodes by insertion of a two dimensional photonic crystal structure. *Jour Appl Phys* **96** (12), 7629.
194. Q. Yue *et al* (2012). Enhancing the out-coupling efficiency of organic light-emitting diodes using two dimensional periodic nanostructures. *Adv. Mater. Sci & Eng.* **2012**, 1.

- 195.H. Zhao *et al* (2013). Analysis of Internal Quantum Efficiency and Current Injection Efficiency in III-Nitride Light-Emitting Diodes. *Jour of Display Tech.***9**(4), 212.
- 196.K. Hong and J.L. Lee (2011). Review Paper: Recent Developments in Light-Extraction Technologies of Organic Light-Emitting Diodes. *Elec. Mater Lett.*, **7** (2), 77.
- 197.M.Ariu *et al* (2002). The effect of morphology on the temperature-dependent photoluminescence quantum efficiency of the conjugated polymer poly(9,9-dicoylfluorene). *J. Phys.: Condens. Matter.* **14**, 9975–9986
- 198.C.M. Yang *et al* (2008). Electron mobility and electroluminescence efficiency of blue conjugated polymers. *Synthetic Met.* **158**, 25.
- 199.E.M. Purcell, H.C. Torrey, and R.V. Round (1945). Resonance Absorption by Nuclear Magnetic Moments in a Solid. *Radiation Laboratory*, Massachusetts Institute of Technology.
- 200.L.R. Fleet, M. Babiker, and M. I. J. Probert (2009). An experiment on the Purcell effect in a wedge cavity. *Eur J Phys.* **30**, 81.
- 201.D.M. Carroll, C.E. Hofmann, and H.A. Atwater (2010). Conjugated Polymer/Metal Nanowire Heterstructure Plasmonic Antennas. *Adv Mater.* **22**, 1223.
- 202.D.M. Carroll *et al* (2012). Metal-Polymer-Metal Split Dipole Nanoantennas. *Adv Mater.* **24**, 136.